N° d'Ordre : D.U. 2376

UNIVERSITE BLAISE PASCAL
U.F.R. Sciences et Technologies

ECOLE DOCTORALE DES SCIENCES FONDAMENTALES
N° 759

THESE

présentée pour obtenir le grade de

DOCTEUR D'UNIVERSITE

Spécialité : Physique des Matériaux

Par **NILSSON Jonas**

Master

ELECTRICALLY GENERATED ENTANGLED LIGHT FOR OPTICAL QUANTUM INFORMATION APPLICATIONS

Soutenue publiquement le 19 Septembre 2013, devant la commission d'examen:

Président : MARIE Xavier
Rapporteur : BESOMBES Lucien
Rapportuer : TARTAKOVSKII Alexander
Examinateur : CENTENO Emmanuel
Directeur de these : MALPUECH Guillaume
Directeur de these : STEVENSON Mark
Invité : SOLNYSHKOV Dmitry

Declaration

This dissertation describes original work carried out at the Cambridge Research Laboratory of Toshiba Research Europe Ltd, from October 2010 to July 2013. The work was done in close collaboration with the Semiconductor Physics Group at the Cavendish Laboratory, Cambridge University, and with Université Blaise-Pascal, Clermont-Ferrand.

Acknowledgements

First of all I would like to extend my gratitude to Mark Stevenson of Toshiba Research Europe Ltd for his guidance during my time at the Cambridge Research Laboratory (CRL). It has been a pleasure working with you on the entanglement project and I am sure you will continue to generate many exciting results in the coming years. To Cameron Salter and Branislav Dzurnak I say: it was a pleasure to share the entanglement lab with you! Anthony Bennett and Martin Ward also deserve special mentioning for many rewarding discussions and for a lot of help in the lab. Dave Ellis and Joanna Skiba-Szymanska, you are not only semiconductor processing wizards but also rock solid colleagues that one can always rely on. Adrian Chan, I truly enjoyed our discussions of physics and numerical modelling, I wish you all the best after your PhD. Also many thanks to Marco Lucamarini for many interesting exchanges of ideas, and for helping us with the important theoretical bits for the teleportation paper. A special thanks also to Andrew Shields, for leading and supporting our work in the Quantum Information Group at Toshiba, and for giving me the opportunity to present our work to the outside world on many occasions. Iris Choi and Sokratis Kalliakos, you are both great friends and colleagues, people like you make it easy to go to the office even on a rainy Monday morning in November.

Many thanks to Ian Farrer, Ken Cooper, Melanie Tribble and professor David Ritchie of the Semiconductor Physics group at University of Cambridge. I am also grateful for the academic guidance provided by Guillaume Malpuech of Université Blaise Pascal, and for managing of the EU Initial Training Network SPIN-OPTRONICS which funded much of this work. To Bernhard Urbaszek, Louis Bouet, Sergej Kunz, Thierry Amand and Xavier Marie of INSA-Toulouse I send my greatest appreciations for a fruitful and very enjoyable collaboration.

I am forever indebted for the extraordinary support and love given by the Nilsson and Engelbrecht families. Thousands of kilometres away, you are nevertheless always close. And most importantly, thank you Shilo for sharing this three year adventure in the United Kingdom with me, I will always strive to support you as you have supported me. I will forever be your companion on your endeavours, I love you very very much.

Publications

Parts of this thesis have or will appear in the following publications and conference contributions.

Articles

Stevenson R. M., Salter C. L., Nilsson J., Bennett A. J., Ward M. B., Farrer I., Ritchie D. A., Shields A. J., *Indistinguishable entangled photons generated by a light-emitting diode*, Physical Review Letters **108**, 040503 (2012).

Nilsson J., Stevenson R. M., Chan K. H. A., Skiba-Szymanska J., Lucamarini M., Ward M. B., Bennett A. J., Salter C. L., Farrer I., Ritchie D. A., Shields A. J., *Quantum teleportation using a light-emitting diode*, Nature Photonics **7**, 311-315 (2013).

Stevenson R. M., Nilsson J., Bennett A. J., Skiba-Szymanska J., Farrer I., Ritchie D. A., Shields A. J., *Heterogeneous teleportation with laser and quantum light sources*, submitted for publication, pre-print: http://arxiv.org/abs/1307.3197 (2013).

Nilsson J., Bouet L., Bennett A. J., Amand T., Stevenson R. M., Farrer I., Ritchie D. A., Kunz S. Marie X., Shields A. J., Urbaszek B., *Voltage control of electron-nuclear spin correlation time in a single quantum dot*, submitted for publication, pre-print: http://arxiv.org/abs/1306.1415 (2013)

Conference contributions

Nilsson J., Stevenson R. M., Salter C. L., Bennett A. J., Ward M. B., Farrer I., Ritchie D. A., Shields A. J., *Indistinguishable and entangled photon pairs from a quantum dot LED*, IOP Quantum dot day, 5 january 2012 London (talk)

Nilsson J., Stevenson R. M., Salter C. L., Bennett A. J., Ward M. B., Farrer I., Ritchie D. A., Shields A. J., *Electrically generated indistinguishable and entangled photon pairs* (QF2F.5), Conference on Lasers and Electro-Optics – International Quantum Electronics Conference, San Jose 6-11 May, 2012 (talk)

Nilsson J., Stevenson R. M., Salter C. L., Bennett A. J., Ward M. B., Farrer I., Ritchie D. A., Shields A. J., *Indistinguishable and entangled photons generated by a light-emitting diode*, International School on Spin-Optronics, St. Petersburg July 10-14 2012 (poster)

Nilsson J., Stevenson R. M., Salter C. L., Bennett A. J., Ward M. B., Farrer I., Ritchie D. A., Shields A. J., *Electrical generation of indistinguishable and entangled photon pairs using a quantum dot LED*, International Conference on the Physics of Semiconductors, Zürich July 29 - 3 August 2012 (talk)

Nilsson J., Stevenson R. M., Chan K. H. A., Skiba-Szymanska J., Lucamarini M., Ward M. B., Bennett A. J., Salter C. L., Farrer I., Ritchie D. A., Shields A. J., *Teleportation using a Quantum Dot Entangled-Light-Emitting Diode* (PD-B.3), Conference on Lasers and Electro-Optics – International Quantum Electronics Conference, München, May 12-16 2013 (post-deadline talk)

Nilsson J., Stevenson R. M., Chan K. H. A., Skiba-Szymanska J., Lucamarini M., Ward M. B., Bennett A. J., Salter C. L., Farrer I., Ritchie D. A., Shields A. J., *Teleportation using entangled photons from an electrically excited quantum dot*, International Conference on Spin-Optronics, Toulouse, June 11-14 2013 (talk)

Nilsson J., Stevenson R. M., Chan K. H. A., Skiba-Szymanska J., Lucamarini M., Ward M. B., Bennett A. J., Salter C. L., Farrer I., Ritchie D. A., Shields A. J., *Teleportation using electrically generated entangled photons from a quantum dot*, Progress in Electromagnetics Research Symposium, Stockholm, August 12-15 2013 (talk)

Abstract

Semiconductor quantum dots offer an attractive route towards efficient and high-quality photon sources for optical quantum information applications, with potential for miniaturization and integration on chip.

Here, entangled photon pairs are generated in the biexcitonic radiative cascade resulting from electrical excitation of InAs self-assembled quantum dots placed in a p-i-n diode. In a first set of experiments the non-classical polarisation correlations and the ability to interfere the photons in two-photon interference experiments was verified, finding entanglement fidelities of up to 0.87 ± 0.04 and interference visibilities up to 0.60 ± 0.05.

Encouraged by the two-photon interference experiments, the first directly electrically driven teleporter was implemented in a single-mode fibre circuit. An average fidelity of 0.704 ± 0.016 was achieved for six states symmetrically distributed on the Poincaré sphere, beating the classical limit of 2/3 and proving that quantum teleportation is taking place.

A modified teleportation setup allowed for the accommodation of input photons from an independent CW laser. Two-photon interference between the dissimilar light sources was demonstrated and quantum beats could be observed. Quantum teleportation of polarisation states carried by laser photons was then performed with average fidelity 0.76 ± 0.012.

Controlling confined charge carriers in nano-scale systems such as quantum dots requires a deep understanding of the underlying material physics, even on the nuclear level. Voltage control of electron-nuclear hyperfine spin interactions was demonstrated using a charge-tuneable device. Modelling suggests that the mechanism is controlled mainly via the electron hyperfine correlation time and the nuclear depolarisation time.

Résumé

Les boites quantiques de semiconducteurs représentent une voie attractive pour la réalisation de sources de photon efficaces pour le transfert quantique de l'information, avec un fort potentiel de miniaturisation et d'intégration.

Dans ce travail, les paires de photons intriqués sont générées via le déclin radiatif de bi-excitons, à partir de boite quantiques d'InAs auto-assemblées placé dans une jonction p-i-n. Dans une première série d'expérience d'interférence à deux photons, nous avons démontré des corrélations de polarisation non classiques et la capacité de deux photons à interférer. L'intrication a été démontrée avec une fidélité de 0.87 ± 0.04, et une visibilité des interférences de 0.60 ± 0.05.

Nous avons ensuite réalisé le premier téléporteur injecté électriquement dans un circuit à fibre monomode. Une fidélité moyenne de 0.704 ± 0.016 a été mesurée pour 6 états distribués symétriquement sur la sphère de Poincaré, ce qui supérieur à la limite classique de 2/3 et prouve la téléportation.

Un dispositif modifié de téléportation permettant d'injecter des photons à partir d'un laser continu indépendant a été développé. L'interférence à deux photons entre sources différentes a été démontrée et des battements quantiques observés. La téléportation quantique des états de polarisation portés par les photons a été obtenue avec une fidélité moyenne 0.76 ± 0.012.

Le contrôle du spin des charges confinés dans les nanostructures tels que les boites quantiques requiert une compréhension profonde de la physique des matériaux constituant, y compris au niveau nucléaire. Ainsi, nous avons démontré le contrôle électrique de l'interaction hyperfine entre les spins électroniques et nucléaires en utilisant un composant à charge ajustable. La modélisation suggère que le mécanisme est contrôlé par le temps de corrélation hyperfine de l'électron et le temps de dépolarisation du noyau.

Contents

1 Introduction

1.1 Entanglement

Entanglement is a central concept in quantum physics and has been the cause of much debate regarding the interpretation and completeness of quantum mechanics, most notably involving authorities such as Einstein[1], Bohr[2] and Schrödinger[3] in the first half of the previous century[4]. In addition to its role as a fundamental concept it is today slowly moving towards the realms of engineering and applications as the field of quantum information matures[5].

The type of entanglement considered in this thesis is polarisation-entanglement of two photons, described by states such as

$$|\psi_{12}\rangle = (|H_1H_2\rangle + |V_1V_2)/\sqrt{2} \quad (1.1)$$

where H and V are linearly polarised orthogonal states. Note that the state in equation 1.1 is inseparable with respect to particles 1 and 2. If we would measure the polarisation of any of the particles on its own, we would find that it was completely random, i.e. unpolarised. Still, if we measured both particles 1 and 2 and compared the results, we would find that they were always perfectly correlated. Erwin Schrödinger (who coined the term entanglement) captured this, which is perhaps the essence of entanglement, rather well[6]:

"Best possible knowledge of a whole does not include best possible knowledge of its parts - and that is what keeps coming back to haunt us."

Having two particles in a state such as $|\psi_{12}\rangle$ above has very counter-intuitive and distinctly non-classical consequences; the photons 1 and 2 can in principle be separated by an arbitrarily large distance, and a measurement on 1 yielding H will instantaneously reduce the possible outcomes of particle 2 to H only, in accordance with the collapse of the wavefunction in the Copenhagen interpretation. Einstein, Podolsky and Rosen strongly objected to this non-local consequence of the interpretation of quantum mechanics, and argued that the theory must be incomplete[1]. Bell[7] and others[8] later developed a set of inequalities whose violation would disprove the possibility of any underlying "hidden variables theory" that could actually be at play and explain the correlations.

Today, after numerous experiments violating the Bell inequalities (albeit all with small imperfections and possibilities of "loopholes")[9–12], entanglement is an accepted part of quantum physics, and it plays a key role in quantum information applications. Perhaps the most prominent example, and an important primitive for more complex tasks, is quantum teleportation[13,14] (the topic of chapters 3 and 4), in which a measurement is performed on two particles, yielding no information about the individual particles but full information about their joint state, resulting in transfer of quantum information onto a third particle.

Entanglement is not limited to just two photons – the largest entangled state produced to date (with considerable effort) is with eight photons[15] – and in principle any degree of freedom could be entangled (e.g. space, time, energy). Furthermore we are by no means restricted to photonic qubits; entanglement has been demonstrated for example using atoms[16] , ions[17] and spins in NV-centres[18]. When it comes to entangled photon pairs specifically, there is a need to replace the most commonly employed source spontaneous parametric down-conversion (SPDC). Semiconductor quantum dot light sources, the topic of this thesis, represent one of the prime candidates to achieve this.

1.2 Self-assembled quantum dots

1.2.1 Background

"Quantum dots" (QDs) can be considered a collective name for several types of semiconductor nanostructures that have in common that they provide charge carrier confinement, which can be provided either by enclosing a lower bandgap material in a higher bandgap one or by just limiting the size of small semiconductor crystallites. Colloidal quantum dots, nanoscale semiconductor crystals created by nucleation from pre-cursors suspended in a liquid, emerged in the 1980s[19,20]. In the late 1980s lithographically defined QDs were realised and the term "quantum dot" was coined[21]. Other ways to provide three-dimensional confinement is by electrostatically defining a trapping potential[22] or, which is the type of dot used in the rest of this work, through self-assembly of QDs by epitaxial thin film growth, which has also been researched since the 1980s[23].

All samples used in subsequent chapters are InAs QDs on GaAs substrates grown by Ian Farrer at the Cavendish laboratory of the University of Cambridge by molecular beam epitaxy (MBE). In MBE growth material is deposited slowly (~μm/h), layer by layer, which results in very high crystal quality with few defects and well-defined material layers. For InAs self-assembled dot growth the In and As atoms are deposited in a thin film on a GaAs crystal. Both semiconductors have a face-centred cubic zinc-blende structure but are lattice mismatched (~7%). This results in a strain developing as the InAs is deposited, and after about two monolayers small islands – quantum dots – start to nucleate spontaneously on the InAs thin film which is commonly called the wetting layer (WL). This growth mode with dots forming on top of a wetting layer (essentially a quantum well) is referred to as Stranski-Krastanov (S-K) mode.

Typical morphology of self-assembled InAs QDs are lens shaped islands of ~5 nm height and ~30 nm base[24]. The small size, combined with confinement due to the differing bandgaps (GaAs ~1.5 eV, InAs ~0.35 eV[25]) gives the QDs quantized electronic structure and discrete optical transitions[26] which has earned the QDs the popular nickname "artificial atoms". Figure 1.1 below shows an example photoluminescence spectrum of an InAs QD sample, showing broad wetting layer emission and many discrete spectral lines attributed to an ensemble of QDs.

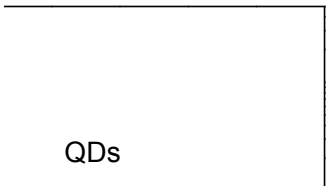

Figure 1.1: Photoluminescence spectrum of InAs self-assembled QD sample excited by a 780 nm laser, exhibiting a broad, intense peak from recombination in the wetting layer (~868 nm) and an ensemble of discrete lines between ~880 – 900 nm attributed to quantum dots.

Through variation of MBE growth conditions the properties of the QDs can be varied according to intended application, for example the QDs used in chapters 2-4 were optimized for entangled light emission[27], while the dots in chapter 5 were designed to emit at slightly longer wavelength. The spontaneous nucleation in S-K growth means that the spatial distribution of QDs is random, which of course can be problematic for applications. To address this issue site-controlled QD growth is being researched[28,29], but so far these dots do not match the self-assembled ones in quality, for example in terms of narrow linewidths. Of particular interest with respect to the main theme of this thesis are recent results showing entangled photon pair emission from site-controlled QDs[30].

Quantum dots find many potential applications in the field of quantum information processing[31], most notably as single photon emitters[32,33], entangled photon pair emitters[34,35] but potentially also as quantum memories[36] and even for photonic cluster state generation[37].

1.2.2 Electronic structure and exciton complexes in InAs quantum dots

The bandgap of InAs is very small, only ~0.35 eV, much smaller than that of GaAs (~1.5 eV) and also very different to the emission at energies ~1.4 eV attributed to the InAs WL and QDs in figure 1.1 above. From the quantum mechanical textbook example of a particle in a one-dimensional potential well[38], in which the lowest lying energy state of a confined electron scales as $\sim\hbar^2/md^2$ (relative to the bottom of the well), we can understand that the size plays a role. The emission can be expected to blueshift as d becomes smaller. We can also expect the states of trapped charge carriers to be quantized for a sufficiently small confinement region. For a realistic model of the quantum dot electronic structure a more sophisticated model is needed, in particular the weaker in-plane confinement needs to be accounted for. Modelling the QD as a disk or as lens shaped[39], the "orbitals", or angular momentum states, of the "artificial atoms" can be described. It has been found that a parabolic in-plane confinement potential, illustrated in figure 1.2, describes the lowest lying states (labelled s, p following atomic physics conventions) of QDs well[40].

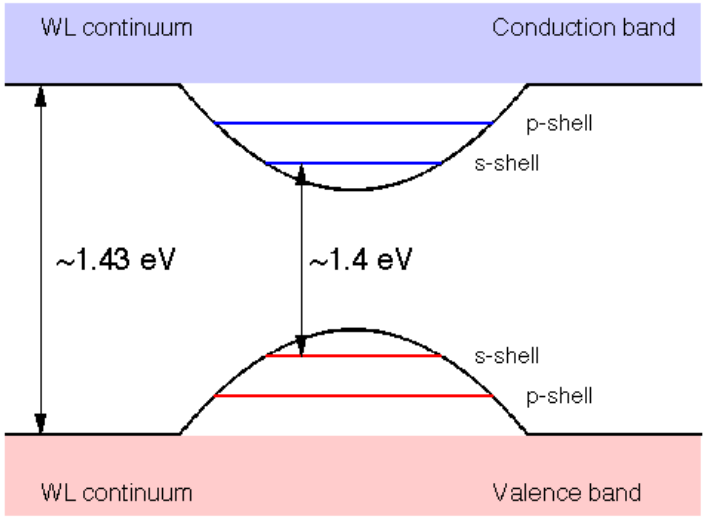

Figure 1.2: Schematic of QD in-plane confinement potential and states. Only the ground state (s) and first excited (p) state for electrons and holes are shown. The blue bands represent the wetting layer continuum of states, with carriers free to move in the 2D plane of the wetting layer.

Usually, it is sufficient to consider only the lowest lying s-orbital and possibly the first excited state (p), as higher states are either not confined[39] or relax to the ground state very rapidly[41,42], significantly faster than typical exciton lifetimes (a few 100 ps to 1 ns). Furthermore, it is usually sufficient to limit the discussion to heavy holes (angular momentum projection $m_j = \pm 3/2$), as spin-orbit coupling splits off light holes ($m_j = \pm 1/2$) by several tens of meV in InAs QDs[43] which are therefore usually not well confined. Typical confinement energies for electrons and heavy holes in InAs QDs are 50 meV and 25 meV respectively[43]. The proximity in energy to the wetting layer quasi-continuum of states limits the use of InAs QDs to cryogenic temperatures, as significantly higher temperatures lead to thermally assisted carrier escape. Other material systems, for example CdSe/ZnSSe from the II-VI groups, provide wider bandgap differences and stronger confinement and can be used to address this problem[40].

QDs are optically active through radiative recombination of the excitonic complexes. The neutral exciton (X) forms when one electron and one hole are trapped in the dot. The exciton total angular momentum projection quantum number M is a combination of electron and hole spin/angular momentum, $M = S_{e,z} + J_{h,z}$. Either the electron and hole spins line up parallel, to form the dark exciton states with total angular momentum $M = \pm 2$, or anti-parallel to form the optically active $M = \pm 1$ bright states[44]. Hybridisation between dark and bright states due to a transverse magnetic field or confinement potential asymmetries does allow for the dark states to be weakly observed in spectroscopy[44], but we shall safely ignore them in the rest of this thesis.

The X and the biexciton (XX, formed by two electron-hole pairs) will be of particular interest in most of this thesis as they can be used for entangled light generation. Figure 1.3(a) shows a state diagram illustrating how this can occur in an ideal quantum dot. Since the biexciton has $M = 0$ and the bright exciton eigensstates have $M = \pm 1$, conservation of angular momentum dictates that the emission will be circularly polarised, carrying angular momentum $\pm\hbar$. This means that photon pairs emitted in a radiative cascade form XX to the ground state will be polarisation-entangled in state $|\psi\rangle = (|R_{XX}L_X\rangle + |L_{XX}R_X\rangle)/\sqrt{2}$. Unfortunately, real world QDs always possess varying degrees of asymmetry due to e.g. strain. This anisotropy introduces an electron-hole exchange interaction which hybridises the exciton $M = \pm 1$ states, making the new eigenstates linearly polarised and non-degenerate as illustrated in figure 1.3 (b)[44]. The splitting s, commonly referred to as the fine structure splitting (FSS), causes the joint photon pair polarisation state to be $|\psi\rangle = (|H_{XX}H_X\rangle + \exp(is\tau/\hbar) \cdot |V_{XX}V_X\rangle)/\sqrt{2}$, where τ is the time spent in the intermediate X state[45]. Unless the natural linewidth of the exciton state $\Gamma_X > s$ (or, expressed equivalently in the time domain, a lifetime shorter than the entangled state evolution period $\hbar/s$) this will result in reduced entanglement fidelities. Loss of coherence between the $|H_{XX}H_X\rangle$ and $|V_{XX}V_X\rangle$ components and spin-scattering in the X state have been found to occur on time scales significantly larger than the X lifetime[46,47] and play an negligible role.

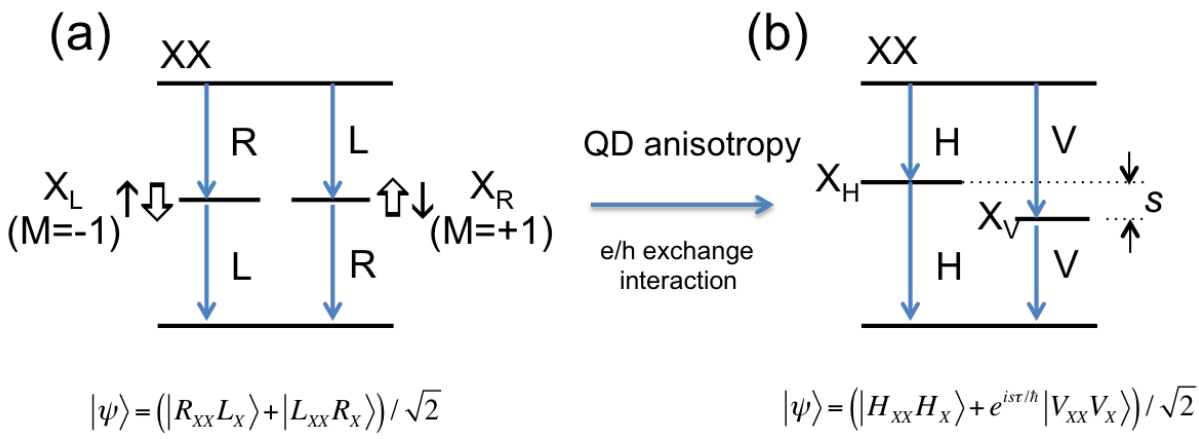

Figure 1.3: (a) An ideal, perfectly symmetric quantum dot emits polarisation entangled XX and X pairs in a radiative cascade. The X eigensstates have eigensstates characterised by total angular momentum $M = \pm 1$ which recombine with emission of circularly polarised photons. (b) QD anisotropy causes electron/hole exchange interactions, hybridising the otherwise degenerate X_L and X_R states and introduces a fine structure splitting s, which results in an unwanted phase factor in the XX-X biphoton state.

Different approaches to reducing the FSS have been developed, one of them being to address the QDs directly: The FSS of self-assembled InAs QDs correlates with the X emission energy, and at 1.4 eV (885 nm) the average QD FSS is minimised[27] although a statistical distribution still exists. The physical cause for the minimised FSS is attributed to weaker exciton confinement and increased penetration into the surrounding barrier material, which reduces the effect of the exchange interaction and consequently minimises the FSS. Dots with emission wavelength around 885 nm can be obtained with appropriate QD growth conditions, which is the approach taken for dots used in this work, or post-growth thermal annealing[27,48]. Reversible tuning of the FSS by magnetic field[35], strain[49] or electric field[50] has also been shown to be a viable approach to minimise the FSS. Another post-growth method is to fabricate an optical microcavity at the site of a suitable QD[34], circumventing the FSS by achieving Purcell enhancement and ensuring $\Gamma_X > s$. Using other quantum dot material systems such as strain-free GaAs droplet dots offers yet another path towards entangled light emission that is also being pursued[51].

Singly charged negative/positive excitons $X^{\pm}$ can form when an electron/hole is added to the neutral exciton or removed from the biexciton. In the context of entangled light emission they are unwanted and must be suppressed, as they can interrupt the radiative cascade and reduce the XX-X entanglement fidelity. In other situations the positive exciton X^{+} is welcomed, since it can be used as a tool to optically control and probe the electron-nuclear hyperfine interactions, as demonstrated in chapter 5.

1.3 Quantum dot light-emitting diodes

1.3.1 Background

The need for new single-photon and entangled photon-pair sources is getting more and more evident in the rapidly developing field of optical quantum information science. The most commonly used type of source, spontaneous parametric down-conversion (SPDC) pumped by lasers is inherently probabilistic with random number of photons emitted in each excitation pulse. The photon numbers are governed by Poisson statistics, which means that if the probability to get one photon pair is p the probability to have two photon pairs is $p^2/2$. Multiple-pair rates can introduce errors in quantum computing circuits or make quantum key distribution systems vulnerable to photon-number-splitting attacks[52]. Already in today's relatively small scale multi-photon experiments the multi-pair emissions constitute a limiting factor[14,53]. The only way to keep the multiple-pair probability low is to keep the overall intensity (i.e. p) low, and for SPDC high efficiency and low error rate thus stand in fundamental contradiction to each other[54,55]. Quantum dots on the other hand in principle do not have such a limitation, and furthermore offer many degrees of engineering freedom and tuneability with respect to emission wavelength, fine structure and other properties (with a very important one being the optical cavity design, see section 1.3.3). This could potentially allow QDs to be used as a technological foundation for triggered, high-efficiency, high purity quantum light sources, and has therefore attracted a lot of research interest in recent years.

By placing a quantum dot in a diode structure an electrically driven single-photon source can be created. The motivation for having an electrically driven and controlled semiconductor single photon source is clear, as semiconductor technology could allow them to be miniaturised, and one could envision something like integrated sources without the need for bulky driving lasers typically used for optical excitation.

A proposal for single-photon and entangled-pair emitting diodes based on quantum dots was introduced in 2000 by Benson et al[56]. The proposal centred around resonant tunnelling of electrons and holes into the quantum dot to deterministically load it with carriers, and optical cavity engineering to achieve high light extraction efficiency. The first single photon emitting diode was realised by Toshiba Research Europe in 2002[33], followed later by other groups also showing promising results[57,58]. In 2010 the first entangled-light emitting diode was demonstrated, also based on quantum dots[59]. The operation principle, which is simpler than Benson's original proposal, is described in sections 1.3.2 and 1.3.3.

1.3.2 Entangled light emitting diode

The entangled-light-emitting diode[59] (ELED) is based on self-assembled InAs QDs, grown to emit around 885 nm and thus have minimal FSS (see section 1.2.2), embedded in a p-i-n diode structure. Figure 1.4 below shows a schematic band diagram of such a device. When a positive bias voltage is applied the potential barrier extending over the intrinsic GaAs region is lowered and current can flow through the junction. Electrons and holes relax via the wetting layer to the ground state of the quantum dot, where they can form biexciton (XX) and exciton (X) complexes. As discussed in section 1.2.2 polarisation-entangled XX-X pairs can be emitted if the radiative recombination happens in a cascade from the XX state. A key design parameter for the ELED is the thickness of the intrinsic region, which is relatively large, ~400 nm. It was found that with thinner intrinsic regions charged emission lines (primarily X^-) appeared and polarisation correlation was lost, indicating tunnelling of electrons into the dot[60]. Hole tunnelling is easier to suppress as holes have ~10 times higher effective mass than conduction electrons in GaAs.

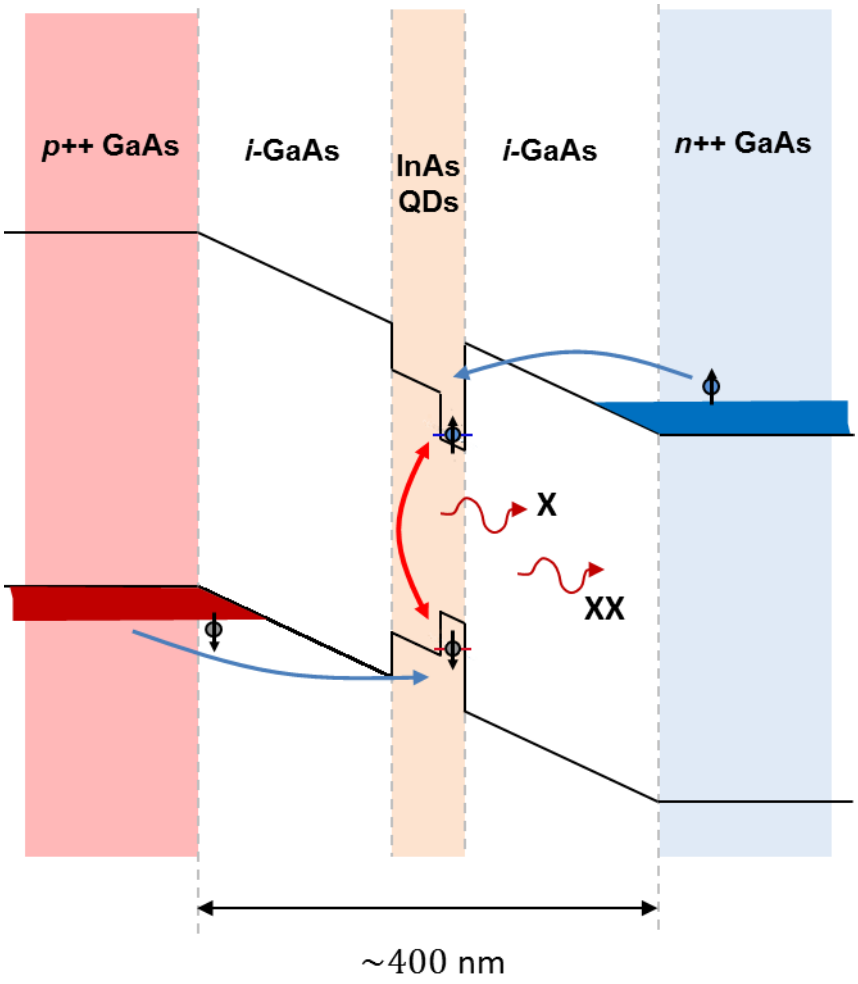

Figure 1.4: Schematic band diagram of the entangled-light-emitting p-i-n diode. Applying a positive bias lowers the potential barrier and allows current to flow through the junction, resulting in population of the QDs. A thick intrinsic region (~400 nm) ensures that the QD emission is dominated by the neutral exciton complexes (XX, X).

The ELED design also includes distributed Bragg reflectors of alternating layers of Al(Ga)As and GaAs (see section 1.3.3 for details) to improve the light collection efficiency around the wavelengths of interest (~885 nm). The DBRs are placed outside the intrinsic GaAs region and are epitaxially grown together with the QDs. High doping levels ensure that they are essentially metallic and highly conducting.

Device mesas of typical dimensions on the order of 100 μm x 100 μm are defined using standard optical lithography and wet-etching techniques. Bottom contacts (to the n++ layers) are deposited using evaporation, lift-off and subsequent thermal annealing of AuGeNi to form a low resistivity Ohmic contact. Quasi-ohmic top contacts are typically made by depositing Ti/Au on top of the p++ doped DBRs. Figure 1.5 shows current-voltage characteristics for a representative ELED fabricated in this way. Turn-on occurs around ~1.5V, roughly matching the bandgap of GaAs as expected. In reverse bias the leakage is in the picoampere range, indicating shunt resistances at least $R_P > 100\ G\Omega$. In high forward bias the current is limited by series resistances[61], and here we find $R_S \sim 60\ \Omega$.

Figure 1.5: IV characteristics of a typical quantum dot p-i-n diode (a) linear scale and (b) semi-logarithmic scale.

1.3.3 Optical cavity design

1.3.3.1 Planar cavity design considerations

A well-known problem for semiconductor light sources, quantum light sources and general-purpose LED lighting alike, is to achieve high light extraction efficiencies[61,62]. The first caveat is that a dipole emitter, for example a single QD, in the semiconductor emits half the light into the 2π solid angle away from the extraction surface. This can obviously be addressed by engineering a reflective backplane, thereby "recycling" the light. In epitaxially grown heterostructures, such as the QD LEDs considered here, a bottom mirror can be realised by introducing distributed Bragg reflectors (DBRs), consisting of alternating layers of thickness $\lambda/4n_i$ of materials with different refractive index n_i. In our QD LEDs the DBRs are made out of Al(Ga)As ($n_{AlAs} \approx 2.97$) and GaAs ($n_{GaAs} \approx 3.5$). Another problem is that due to the high refractive index contrast between semiconductors and air ($n \approx 1$), the angle of total internal reflection at the semiconductor-air interface is only $\arcsin(1/n_{GaAs}) \approx 17°$ (relative to the surface normal), which means that all light emitted at higher angles remains trapped in the semiconductor material. Figure 1.6 shows the simulated extraction efficiency for a dipole emitter placed in a GaAs slab two wavelengths below the air interface, for 0-20 bottom DBR repeats and different collecting numerical apertures. The calculations were carried out using CAMFR[63,64], a Maxwell equation solver designed for optical microcavity simulations. For NA=0.5 (typically used in experiments in following chapters) the collection efficiency is limited to ~0.6% with no bottom mirror. For increasing number of repeats the DBR reflectivity improves, and the theoretical collection efficiency saturates around 8% for ~20 repeats.

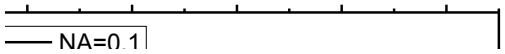

Figure 1.6: Light collection efficiency for dipole placed 2λ below GaAs-air interface for various collecting numerical apertures and bottom DBR repeats.

In figure 1.6 above it is worth noting that the efficiency improved more than 10 times, significantly more than the factor of two if the structure just recycled the light emitted into the "wrong" (bottom) hemisphere. This can be explained by a resonant cavity effect, in which reflected waves from the bottom mirror interfere constructively with forward-emitted waves. Light emitted obliquely goes through regions of positive and destructive interference depending on the angle[64,65]. This concept can be taken further by incorporating top mirror DBRs as well, forming a resonant cavity LED (RCLED) with improved collection efficiency over a range of wavelengths.

Figure 1.7(a) shows the simulation results for a $2\lambda_0$ thick cavity with an in-plane electrical dipole emitter placed in the middle, sandwiched between six top and 18 bottom GaAs/Al(Ga)As DBR repeats. The nominal design wavelength $\lambda_0 = 885$ nm determines the cavity and DBR layer thicknesses, and was chosen to coincide with the emission wavelength of InAs QD for minimal FSS[27]. Figure 1.7(a) shows the out-coupling efficiency η_{out}, defined as the proportion of the light that escapes the semiconductor, the proportion of the out-coupled light that can be collected in a NA=0.5 aperture η_{coll} and the total efficiency $\eta_{tot} = \eta_{out} \cdot \eta_{coll}$ as a function of emission wavelength. Examining η_{out} the first thing to notice is that the maximum extraction efficiency occurs at ~880 nm, i.e. not at the nominal design wavelength, and then remains essentially constant for shorter wavelengths in the simulated range. This is because for positively detuned cavities ($\lambda_0 > \lambda$) the first resonant mode falls within the escape cone of the semiconductor-air interface, a well-known effect for RCLEDs[65]. A side-effect of positive detuning is that the emission pattern becomes less directional[66], as can be seen by comparing figure 1.7(c) showing angular emission pattern for $\lambda = \lambda_0 = 885$ nm and 1.7(b) for $\lambda = 881,873$ nm. For a given NA (here NA=0.5) a higher emission angle (shorter emission wavelength) of the out-coupled light means less can be collected, which explains the drop of η_{coll} for $\lambda < \lambda_0$. All factors taken together, the total efficiency η_{tot} has a peak value of 17% centred around 883 nm, i.e. only slightly detuned from the nominal design wavelength, and a bandwidth of FWHM~8 nm.

By adding more top and bottom DBRs the resonant cavity effect can be made stronger over a narrower bandwidth. One thing to consider for the ELED is that the X and XX transitions are in general not degenerate due to Coulomb interactions between the confined charge carriers. Typical separations are ~2-3 nm and the optical microcavity must thus be designed with this in mind. A very narrow cavity resonance will also give a lower quantum dot yield since fewer dots will emit within the wavelength window.

A small simulation study of different number of top and bottom mirror repeats was carried out, with results presented in figure 1.8, showing the total efficiency η_{tot} (at optimal detuned wavelength) for 10-22 bottom repeats and 0-12 top repeats, assuming collection optics with NA=0.5. As one can expect, the efficiency is increasing with the number of bottom DBRs, but the returns are rapidly diminishing as one approaches ~20 repeats. For each number of bottom repeats the optimal number of top repeats is slightly different, reflecting the balance between out-coupling through top mirror and emission directionality into the collection optics that must be met.

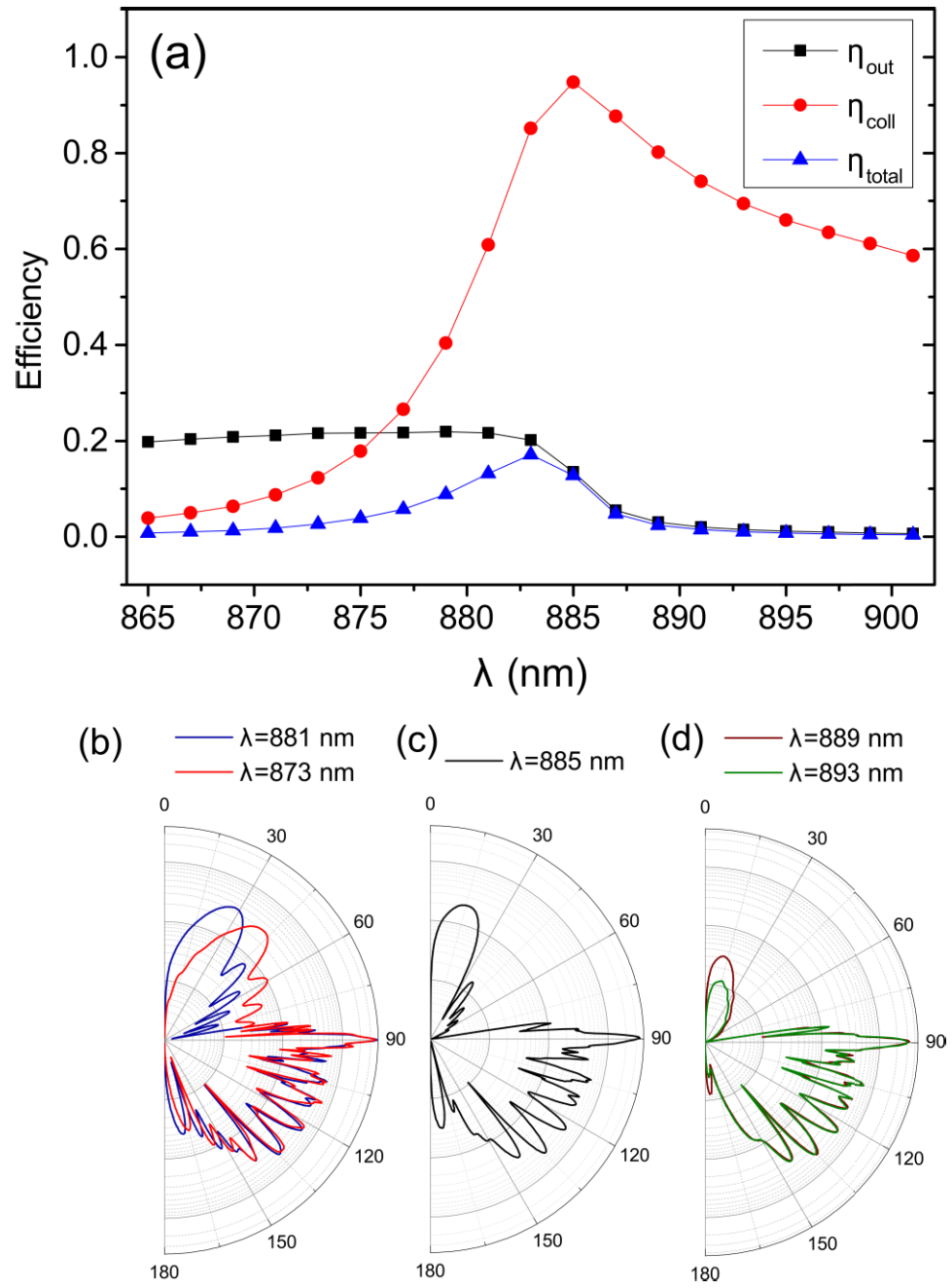

Figure 1.7: (a) Simulated LED light output coupling efficiency (black squares), NA=0.5 collection efficiency (red circles) and total efficiency (blue triangles) for a 6/18 top/bottom DBR $2\lambda_0$ cavity with nominal design wavelength $\lambda_0 = 885$ nm. Maximum total efficiency 17% occurs for 883 nm. Intensity distribution (log scale) as a function of angle to the normal for (a) $\lambda < \lambda_0$, (b) $\lambda = \lambda_0$ and (c) $\lambda > \lambda_0$.

Figure 1.8: Peak total efficiency for $2\lambda_0$ cavities with different numbers of bottom and top DBR repeats.

Figure 1.9 shows a comparison of simulated η_{tot} and experimentally acquired PL-spectrum for a 6/18 DBR cavity with an InAs wetting layer with very low QD density and no QDs in the focal spot. The sample was non-resonantly excited at 780 nm with a diode laser. The PL-spectrum shows a very bright peak at ~860 nm originating from recombination in the wetting layer. No quantum dot emission can be seen, but a peak at 888 nm is visible which is attributed to the tail of the wetting layer feeding into the optical cavity resonance. As shown in the inset the simulated efficiency and PL-intensity overlap very well, verifying that the simulations give qualitatively reliable predictions about the cavity design.

Figure 1.9: Experimental collected emission spectrum for optically excited sample with 6/18 DBR cavity but no quantum dots in the focal spot (black curve). The wetting layer tail extends into the optical cavity wavelength region at ~890 nm with enhanced collection efficiency as a result. The overlaid simulated collection efficiency (red curve) fits the shape of the experimental spectrum well. Inset shows the cavity wavelengths zoomed in.

We can conclude that the cavity configuration with 6/18 DBRs presented in figure 1.7 is a reasonable compromise that gives high light collection efficiency and a relatively broad cavity resonance, able to accommodate both XX and X transitions of typical separations. The predicted efficiency improvement compared to bare GaAs is almost 30-fold. Although one can expect that real-world imperfections reduce the total efficiency, it is in the laboratory obvious that the planar cavity greatly enhances the QD ELED brightness. It should be noted that only negligible Purcell enhancement of spontaneous emission rates is predicted for planar microcavities[65,66], and any such effects are most certainly insignificant in experimental situations.

1.3.3.2 Alternative cavity designs

As mentioned above the planar cavity cannot provide Purcell enhanced spontaneous emission. This would however be highly desirable in order to achieve indistinguishable photons, and indeed such structures can and have been realised in for example photonic crystal waveguides[67] and pillar microcavities[32,68]. Purcell enhanced radiative lifetimes can create new problems with re-pumping of the dot leading to poorer single photon emission characteristics, and to address this different nanowire geometries have been investigated[69]. Very high efficiencies (>70%) have been demonstrated with such designs[70], and they could be made compatible with electrical operation[71]. Entanglement generation via the biexciton cascade presents a problem for narrow-band resonant structures such as pillar microcavities, since the XX and X photons in general are not degenerate. At the same time, Purcell enhanced spontaneous emission of the exciton state appears to be a key to circumvent the finite FSS. To achieve reduced lifetimes for both X and XX a double micropillar structure ("photonic molecule") was used by Dousse et al, achieving high brightness and entanglement fidelities of ~60% without post-selection[34].

The optical microcavities mentioned here offer many avenues that could be explored in order to engineer the emission properties of QD based single photon and entangled light emitting diodes. The planar resonant cavity, however, remains considerably simpler to implement and achieves significant improvements in light collection efficiency compared to having no cavity, without which in particular the three-photon experiments of chapters 3 and 4 would not have been possible.

1.4 Experimental methods

1.4.1 Single quantum dot spectroscopy

Spectroscopic methods were used to characterise and select single quantum dots suitable for the experiments of chapters 2-4. The samples are mounted in a liquid helium cryostat and cooled to ~5-15K. The light from the focal spot (~1 μm) is collected into a numerical aperture NA=0.5 and coupled into either single mode fibre or polarisation-maintaining fibre, with coupling efficiency estimated to ~50%. The small core (~5 μm) and the small acceptance cone of the fibre (NA~0.1) combined with a relatively low quantum dot density in the samples (on the order of one QD per μm^2) means that single dots can be addressed individually with very little light from nearby emission centres being collected. A spectrometer with 600 lines/mm or 1800 lines/mm combined with a low-noise CCD was used to acquire spectra. A motorised half-waveplate can optionally be inserted in the light path before the fibre coupling. Then, if the optical fibre is of polarisation-maintaining type and a linear polariser is placed before the spectrometer entrance slit, polarisation-resolved spectroscopy can be performed to determine e.g. the FSS of the exciton state (see section 2.2.1.1). A white light (broadband) LED is used to illuminate the sample and an image of the sample is registered by a video camera, which allows the sample surface to be navigated using precision stages.

In chapter 5, where spectroscopy plays a very prominent role, a similar but slightly more advanced magneto-spectroscopy setup was used, described in more detailed in said chapter.

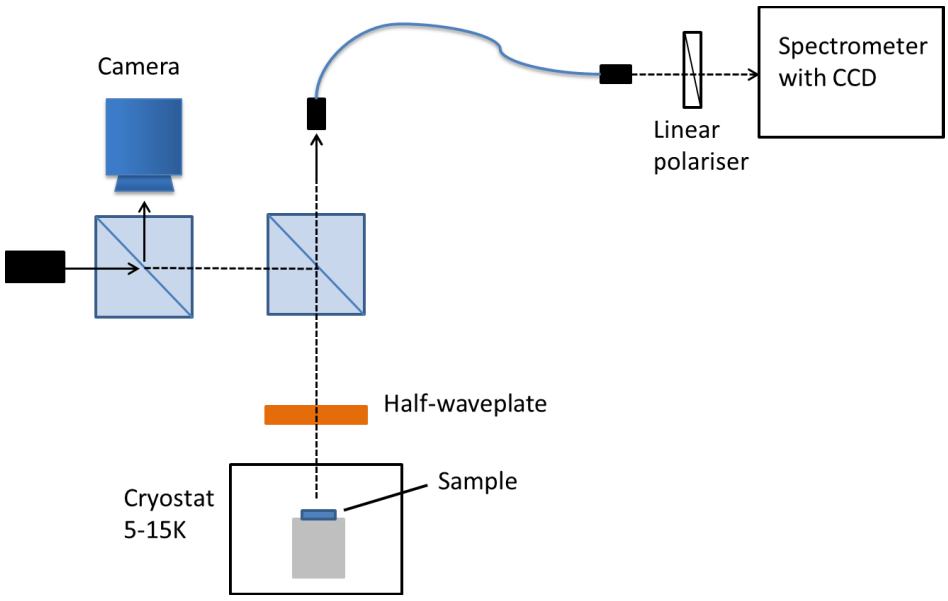

Figure 1.10: Optical setup for single quantum dot spectroscopy. The sample is placed in liquid helium cooled cryostat. An LED for white light illumination and a camera is used for orientation on the sample. Light from the sample is coupled into polarisation-maintaining fibre and sent to a spectrometer equipped with a low-noise CCD. A half-waveplate in combination with a linear polariser is optionally used for polarisation-resolved spectroscopy.

1.4.2 Photon correlation measurements

In chapters 2-4 photon correlation measurements are carried out to probe the light states generated by the quantum dots. In order to observe the quantum effects fast photodetectors are required, and for this purpose single photon counting detectors in combination with fast time correlation electronics are used. The detectors used in this work are either Silicon avalanche photodiodes (APDs) or superconducting single photon detectors (SSPDs). The APDs operate near the reverse breakdown voltage, which leads to an electron avalanche upon detection of a single photon, thereby providing sufficient gain to make detection of single quanta possible. The detection principle of the SSPDs is based on loss of superconductivity (and consequently increased resistance) in the sensing element upon absorption of a single photon. This gives rise to a voltage pulse in the amplifier that can be detected. The SSPDs offer time resolution of ~100 ps, to be compared to the ~300-400 ps resolution of the Si-APDs. This is however achieved at the cost of lower detection efficiency.

The photon correlation electronics has fast discriminators that trigger upon the arrival of an electronic pulse from a detector. Using time to amplitude converters (TAC) and amplitude to digital (ADC) converters the time interval between triggering events from two detectors can be measured with accuracy limited by the detector timing jitter. This enables the measurement of various time-resolved correlation measurements, for example exciton or biexction auto-correlations (Hanbury-Brown-Twiss measurements, section 2.2.1.1), polarisation correlations to evaluate entanglement (section 2.2.1.2) and three-photon correlations for quantum teleportation experiments (chapters 3-4).

In subsequent chapters 2-4, we will continually refer to different polarisation states. We adopt the convention that H and V refer to linear polarisation states coinciding with those emitted by the exciton eigenstate (see figure 1.3). D/A refer to the linearly polarised diagonal superposition states $|D/A\rangle = (|H\rangle \pm |V\rangle)/\sqrt{2}$ and R/L refer to the circularly polarised superposition states $|R/L\rangle = (|H\rangle \pm i|V\rangle)/\sqrt{2}$.

1.4.3 Single photon interference

Single photon interference (SPI) experiments can give insight into the quantum dot physical environment not readily available with spectroscopy directly in the frequency domain[72,73], and is used to characterise the photons produced by the ELED for use in experiments of chapter 2-4. Figure 1.11 below shows a schematic of a Michelson interferometer used for such single photon interference measurements. By measuring the interference fringe visibility as the relative time delay τ between the paths is increased one can determine the photon coherence time τ_c and infer the transition lineshape.

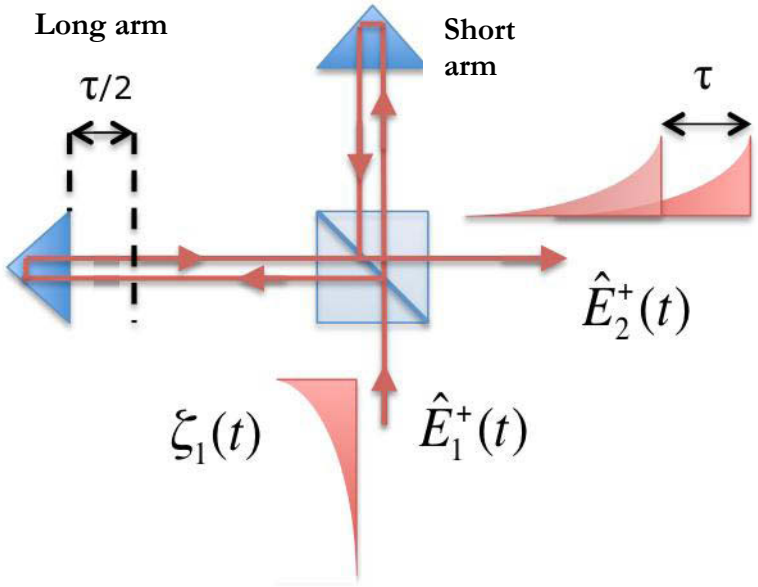

Figure 1.11: Michelson interferometer consisting of a 50/50 beamsplitter and retroreflector. The relative path difference τ between the two arms refers to round-trip time and is variable.

The interferometer is realised by splitting the incoming mode 1 using a balanced beamsplitter. The length of both arms can be varied, one over a relatively long range to introduce large relative path differences (tens of cm), and the other over just very short ranges (tens of μm) using piezo stages with high precision. When the two light field components are recombined on the splitter they form a superposition in the output mode 2. This can be described by expressing the electric field operator $\hat{E}_2^+(t)$ for the output in terms of the operator for the input mode, $\hat{E}_1^+(t)$, taking the passages through the beamsplitter into account:

$$\hat{E}_2^+(t) = \frac{1}{\sqrt{2}}\left(\hat{E}_1^+(t+\tau) + \hat{E}_1^+(t)\right) \tag{1.2}$$

If we assume that the input photons come only one by one, i.e. the input Fock state is $|1\rangle_1$, and that they occupy only certain modes with spatio-temporal mode functions $\zeta_1(t)$, the detection probability at time *t* for a given delay τ can be calculated[74]:

$$P(t,\tau) = \left|\langle 1_1|\hat{E}_2^-(t)\hat{E}_2^+(t)|1_1\rangle\right|^2 =$$
$$= \frac{1}{2}\left|\left\langle 1_1\right|\left(\hat{E}_1^-(t+\tau)+\hat{E}_1^-(t)\right)\left(\hat{E}_1^+(t+\tau)+\hat{E}_1^+(t)\right)\left|1_1\right\rangle\right|^2 \quad (1.3)$$
$$= \frac{1}{2}\left(|\zeta_1(t+\tau)|^2 + |\zeta_1(t)|^2 + \zeta_1^*(t+\tau)\zeta_1(t) + \zeta_1(t+\tau)\zeta_1^*(t)\right)$$

Experimentally, the photons are usually detected by measuring over a long time compared to the photon wavepacket, either using a spectrometer with a CCD or with photon counters such as APDs. Therefore, we integrate over all detection times *t* to get the experimentally accessible detection probability (proportional to measured intensity):

$$P(\tau) = \int_{-\infty}^{\infty} P(t,\tau)dt = 1 + \frac{1}{2}\int_{-\infty}^{\infty} dt\,(\zeta_1^*(t+\tau)\zeta_1(t) + c.c) \quad (1.4)$$

Here we have used that the wavepackets are normalised to $\int_{-\infty}^{\infty} dt\,|\zeta_1(t)|^2 = 1$ and c.c. means complex conjugate.

By varying the long arm the overlap of the displaced wavepacket envelopes at the output mode 2 can be modified as indicated schematically in figure 1.11. Now, by varying the short arm by fractions of the photon wavelength λ interference can be observed when detecting the light in the output mode. The interference goes periodically from constructive to destructive with period λ as the short arm delay is slowly varied. For $\tau = 0$ this interference can be made to be perfectly constructive or destructive. For $\tau > 0$ two effects degrade the interference fringe visibility:

- "Natural" decoherence due to the finite radiative lifetime τ_r or "length" of the photons resulting in different magnitudes of the overlapping wavepackets at a given detection time, as illustrated in figure 1.11.
- Random phase variations in the light field caused by dephasing processes in the quantum dot environment during the emission process, for example fluctuating Coulomb interactions with charges in nearby traps. The time scale on which these events occur is called the pure dephasing time T_2, and once the delay $\tau \sim T_2$ the displaced wavepackets tend to no longer add upp in phase.

These two effects can be embodied in the spatio-temporal mode functions $\zeta_1(t)$. For quantum dots we consider single photon emitters dissipating their energy in an exponentially decaying fashion with characteristic time τ_r, with phase evolving according to the central transition frequency ω. The dephasing can be described by a phase fluctuation $\Phi(t)$ which is assumed to be time-invariant random process with average zero[75]. The mode function can thus be written as:

$$\zeta_1(t) = \begin{cases} A\exp(-t/2\tau_r - i\omega t - i\Phi(t))\text{, for t} \geq 0 \\ 0\text{, else} \end{cases} \quad (1.5)$$

Returning to equation 1.4 we can now evaluate the detection probability:

$$P(\tau) = 1 + \frac{|A|^2}{2}\int_0^{\infty} dt\left(e^{-t/\tau_r - \tau/2\tau_r - i\omega\tau - i[\Phi(t+\tau)-\Phi(t)]} + c.c\right) \quad (1.6)$$

The random process $\Phi(t)$ is assumed to be significantly faster than the radiative decay, and then it can be shown that that $\langle \exp(-i[\Phi(t+\tau) - \Phi(t)]\rangle = \exp(-|\tau|/T_2)$[73,76], which leaves us with the follow expression:

$$P(\tau) = (1 + e^{-|\tau|/2\tau_r - |\tau|/T_2} \cos\omega\tau)/2 = (1 + e^{-|\tau|/\tau_c} \cos\omega\tau)/2 \tag{1.7}$$

In the above expression we have related the coherence time τ_c to the radiative lifetime and the pure dephasing time:

$$\frac{1}{\tau_c} = \frac{1}{2\tau_r} + \frac{1}{T_2} \tag{1.8}$$

When the photons suffer no dephasing ($T_2 \to \infty$) the coherence time is limited by the radiative lifetime and are said to be transform limited. For quantum dots without Purcell enhanced emission, however, the dephasing is usually significantly faster than the lifetime, and to all practical matters $\tau_c \approx T_2$.

From equation 1.7 we can see the fast modulation $\cos\omega\tau$ with small changes in the interferometer delay, as well as a slower overall decay $\exp(-|\tau|/\tau_c)$ for large changes. Experimentally, we measure the interference fringe visibility which is related to the local minima and maxima of eq. 1.7:

$$V(\tau) = \frac{P_{max} - P_{min}}{P_{max} + P_{min}} = e^{-|\tau|/\tau_c} \tag{1.9}$$

The dephasing processes considered above fall into the category called the fast-modulation regime[73,77]. The exponential decay in equation 1.9 is directly related to a Lorentzian lineshape in the frequency domain[78]. If the random modulations are on a time-scale longer than the radiative decay time we will observe an inhomogeneous type of line-broadening, with the spectral lineshape and SPI visibility tending towards Gaussian shapes due to our measurement averaging over effectively over an ensemble of "preparations" of the dot environment. Therefore, the careful observation of single photon interference will reveal important information about the environment of the single photon emitter.

2 Two-photon interference with electrically generated entangled photons

2.1 Introduction

Quantum dots placed in weak optical cavities have been used to demonstrate two-photon interference through post-selection in a multitude of ways; with a single source interfering subsequent electrically generated photons[79,80], two remote quantum dots electrically tuned onto resonance[81] and photons from a quantum dot have been interfered with a laser source[82]. In this chapter we will see how photons emitted simultaneously by a quantum dot can be entangled, and photons emitted at different time can interfere.

2.1.1 Two-photon interference and quantum logic

Quantum interference between photons plays a fundamental role in optical circuits realising quantum logic and in universal quantum computing schemes such as those proposed by Knill-Laflamme-Millburn[83]/Gottesmann-Chuang[84], as well as the recent multi-photon, multi-port Boson Sampling circuits[85,86].

If we take a few steps back from the general multi-port, multi-photon interferometers we find the interference between just two photons. The first two-photon interference (TPI) experiments were performed by Hong, Ou and Mandel[87] (famously referred to as HOM-interference) with photons generated through spontaneous parametric down-conversion (SPDC) in a nonlinear crystal. Many variations of the original experiment have been performed since then, including the demonstration of interference between photons from separate SPDC sources[88] and quantum-eraser-type experiments[89] which stress that the photons must be indistinguishable at the point of measurement but not necessarily at the beamsplitter where they overlap. Since then, many different types of sources have been used to demonstrate TPI: single molecules[90], atoms[91], ions[92], Nitrogen Vacancy centres in diamond[93] and semiconductor quantum dots[79].

At the very heart of two-photon interference lies the concept of indistinguishable particles. Let's consider the typical HOM-type experiment depicted in figure 2.1 where two photons are incident on a 50/50 beamsplitter. Each photon can be either transmitted or reflected, with probability amplitudes $r_{13} = r, r_{24} = -r, t_{14} = t, t_{23} = t$ [94]. This gives us in total four processes that can occur, but if the input photons are indistinguishable there is no way to distinguish the end state (a) from (c) where we have one photon in each output mode. Quantum mechanics dictates that the probability *amplitudes* for these processes involving bosonic particles must be added before considering the probability of the outcome[95]. If the beamsplitter is balanced ($|r|^2 = 1/2$ and $|t|^2 = 1/2$) the probability for two photons in opposite outputs vanishes: $r \cdot (-r) + t \cdot t = 0$. The probability for two photons appearing together in either output mode 3 or 4 becomes $1/2$ for each case, and the effect can be observed as a "bunching" or increase of coincidence rates.

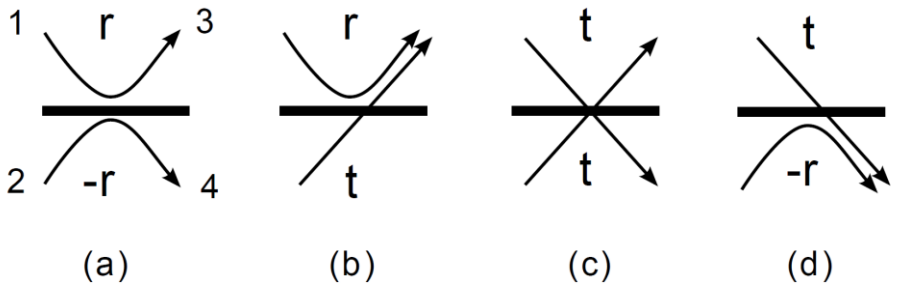

Figure 2.1: Possible processes when two photons are incident on a beamsplitter and associated reflection amplitudes: (a) Both photons reflected, (b) the photon from above is reflected and the one from below is transmitted, (c) both photons are transmitted and (d) the photon from above is transmitted and the one from below reflected. If the photons are indistinguishable the probability amplitudes for (a) and (c) interfere destructively.

It is worth pointing out that two-photon interference effects do not always manifest themselves as "bunching", indeed the effect can be the opposite – "anti-bunching", or an increased probability of photons leaving in opposite ports – if the input photons are prepared in an appropriate anti-symmetric polarisation state such as $|\psi^-\rangle = (|H_1V_2\rangle - |V_1H_2\rangle)/\sqrt{2}$ the spatial (mode) part of the two-particle state is also required to be anti-symmetric (ensuring an overall symmetric state) and interference will ensure that the photons will always appear in opposite output ports[96].

2.1.2 Modelling two-photon interference

To aid the interpretation of the experimental results presented in the following sections a model based on the "wavepacket" analysis by Legero[74] is used. This type of model has been used extensively and successfully before in similar two-photon interference measurements[79,80,82,97].

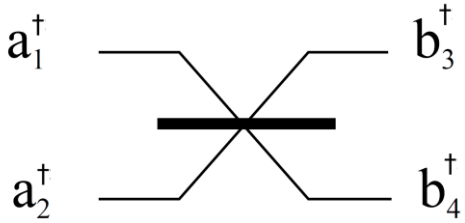

Figure 2.2: Beamsplitter with associated mode operators.

Following Legero's[74] analysis (and the adaptation by Patel et al[80] to non-Gaussian wavepackets) the beamsplitter is considered to have input ports restricted to single modes in the spatio-temporal domain. A balanced beamsplitter can be described using its mode creation/annihilation operators as depicted in figure 2.2, relating the input and output mode annihilation operators according to the common convention:

$$\begin{pmatrix} \hat{b}_3^\dagger \\ \hat{b}_4^\dagger \end{pmatrix} = \frac{1}{\sqrt{2}} \begin{pmatrix} 1 & 1 \\ 1 & -1 \end{pmatrix} \begin{pmatrix} \hat{a}_1^\dagger \\ \hat{a}_2^\dagger \end{pmatrix} \tag{2.1}$$

At this point we do not consider how and when the input photons were generated, we only consider them as freely propagating and limited each to only one mode, described by exponential spatio-temporal mode functions consistent with the Lorentzian lineshapes observed for the X and XX transitions (see section 2.2.1.3 below):

$$\zeta(t) = \begin{cases} A\exp(-t/2\tau_r - i\omega t) \text{ ,t} \geq 0 \\ 0, \text{else} \end{cases} \tag{2.2}$$

The electric field operators for each mode is related to the creation and annihilation operators[98], and due to the restriction to the mode functions of the form in eq. (2.2) this relation is straight-forward[74]:

$$\begin{cases} \hat{E}_1^+(t) = \zeta_1(t)\hat{a}_1 \\ \hat{E}_2^+(t) = \zeta_2(t)\hat{a}_2 \end{cases} \tag{2.3}$$

Using equation 2.1 the electric field operators for the output modes are trivially related to the input counterparts:

$$\begin{pmatrix} \hat{E}_3^+(t) \\ \hat{E}_4^+(t) \end{pmatrix} = \frac{1}{\sqrt{2}}\begin{pmatrix} 1 & 1 \\ 1 & -1 \end{pmatrix}\begin{pmatrix} \hat{E}_1^+(t) \\ \hat{E}_2^+(t) \end{pmatrix} \tag{2.4}$$

The experiments described in the following sections are conducted in d.c., i.e. the arrival time of the photons is random, and to model this Δt has been introduced below as a relative time difference between the wavepackets describing the photons in each mode. Experimentally the two-photon interference manifests itself as a reduction in coincidences between the output modes. Therefore we are interested in calculating the two-photon detection probability of modes 3 at some time t and mode 4 at time $t + \tau$[74,80]:

$$\begin{aligned} g_{34}(t, t+\tau, \Delta t) &= \left|\langle 1_1 1_2 | \hat{E}_3^-(t)\hat{E}_4^-(t+\tau)\hat{E}_4^+(t+\tau)\hat{E}_3^+(t) | 1_1 1_2 \rangle\right|^2 \\ &= \frac{1}{4}|\zeta_1(t+\tau-\Delta t)\zeta_2(t) - \zeta_1(t-\Delta t)\zeta_2(t+\tau)|^2 \end{aligned} \tag{2.5}$$

As indicated by the bra and kets, this expression is conditional upon the presence of two photons in the input modes 1 and 2. Photons emitted by quantum dots usually suffer from decoherence caused mainly by phonon interactions and charge fluctuations in the dot environment, rendering photons emitted at different times partially distinguishable. This is included by adding a random phase fluctuation to the mode functions (as explained in section 1.4.3):

$$\zeta(t) = \begin{cases} A\exp(-t/2\tau_r - i\omega t - i\Phi(t)) \text{ ,t} \geq 0 \\ 0, \text{else} \end{cases} \tag{2.6}$$

By inserting this function for both modes in eq. (2.5) and integrating over t and Δt we arrive at a joint detection probability which is not dependent on the absolute detection time, and is averaged over all possible relative generation time delays. The random phase fluctuations are evaluated similar to in section 1.4.3 and we arrive at the following expression:

$$P_{34}(\tau) = \int_{-\infty}^{\infty} dt \int_{-\infty}^{\infty} d(\Delta t)\, g_{34}(t, t+\tau, \Delta t) = \frac{1}{2}(1 - e^{-2\tau/\tau_c}) \tag{2.7}$$

From eq. 2.7 we clearly see that a key parameter characterising the two-photon interference will be the photon coherence time, and we will use this later to aid the interpretation of the experimental results (sections 2.2.1.3 and 2.2.2.2).

2.2 Experimental

2.2.1 D.c. generation of entangled and indistinguishable photons

2.2.1.1 Device characteristics

The device used in the experiments described here is an entangled-light-emitting diode (ELED) of the type described in section 1.3.2 with two top and 14 bottom DBRs. The device was operated at ~5 K in a liquid helium cooled cryostat system and electrically operated.

Entangled photons can be emitted in the radiative cascade from the biexciton (XX) through the exciton (X) states to the quantum dot ground state[35,59], as described in section 1.2.2 A pre-requisite is that the X fine-structure splitting (FSS) is small compared to the radiative lifetime[99]. The EL-spectrum of the quantum dot investigated here is shown in figure 2.3(a) at a d.c. current density of 70 nA/μm^2. The spectrum is dominated by the X and XX transitions centred around ~1.395 eV, close to ~1.4 eV (885 nm) where dots of this type have been shown to have a minimal average FSS between the exciton eigenstates[27]. Also seen in the spectrum are two very weak lines most likely originating from the positively and negatively charged exciton complexes.

Through linear-polarisation-dependent spectroscopy the fine-structure splitting (FSS) below the resolution of the spectroscopy system can be detected; the detection is linearly polarised and a half-wave plate (HWP) selects the linear state that is detected. As the wave-plate is rotated the measured spectrum shifts through one linear eigenstate (H), to the orthogonal linear eigenstate (V) separated by a 45 degree rotation of the HWP. For intermediate angles varying proportions of these energy eigenstates are detected. For FSS smaller than the system resolution (~30 μeV) the change is only detectable as a change in centre of mass of the spectral lines, but this can be detected through lineshape fitting with an accuracy of ~1 μeV. Figure 2.3(b) shows the XX-X energy separation calculated from such a fitting procedure for the dot studied here. As shown, it was verified to have a FSS of 2.0 ±0.1 μeV. This dot selected for further study was also verified to have coherence properties suitable for two-photon interference experiments, as described later in section 2.2.1.3.

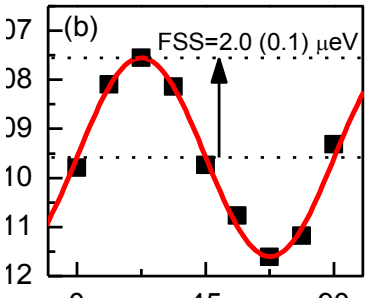

Figure 2.3: (a) Electroluminescence of the chosen quantum dot. (b) Energy difference of the XX and X transitions as a function of HWP angle determined in linear-polarisation-dependent electroluminescence spectroscopy. A fit to the sinusoidal evolution allows the determination of the FSS = 2.0 ±0.1 μeV.

One of the main disadvantages of conventional SPDC entangled-light sources is their Poissonian nature. This presents a fundamental trade-off between interference visibility and source brightness[54], and limits their applicability in large quantum logic applications. The single-photon emission properties of our quantum dot and device are therefore of particular importance. Figure 2.4(a) shows schematic of the Hanbury-Brown-Twiss setup used to investigate this. The light from the ELED is coupled to a fibre system. A spectral filter $\lambda_{XX/X}$ (with bandwidth significantly wider than the X or XX) is tuned to either one of the transitions. A 50/50 beamsplitter and super-conducting single-photon detectors (SSPD1, SSPD2) allow for the measurement of the second-order correlation function:

$$g^{(2)}_{HBT}(\tau) = \frac{< I(t)I(t+\tau) >}{< I >< I >} \tag{2.8}$$

For a perfect single-photon emitter $g^{(2)}_{HBT}(0) = 0$ as two photons cannot be emitted simultaneously. Figures 2.4(b) and (c) show the measured correlation functions for the X and XX transitions respectively. As can be seen the dips extend almost to zero (0.07±0.01 for X, 0.11±0.03 for XX). By calculating the simple function

$$g^{(2)}_{HBT}(\tau) = 1 - \exp(-|\tau|/\tau_0) \tag{2.9}$$

and convolving with the detector-pair response (measured to be Gaussian with FWHM ~150 ps) we can numerically fit the measured correlations and extract time constants τ_0 characterising the dips. We find $\tau_{0,XX} = 322$ ps and $\tau_{0,X} = 773$ ps respectively. The longer time constant for X compared to XX is consistent with the longer lifetime typically found for X. The red curves in figure 2.4 show the theoretical background-free fits to equation 2.9, while the blue curves include the detector time response. The convolved curve overlaps very well with the experimentally determined correlations, and we can conclude that the value of the experimental $g^{(2)}_{HBT}(0)$ is consistent with essentially background-free emission and finite detector response. The low level of background emission from e.g. wetting layer can be attributed to the excellent spatial filtering which is an effect of the fibre-coupling.

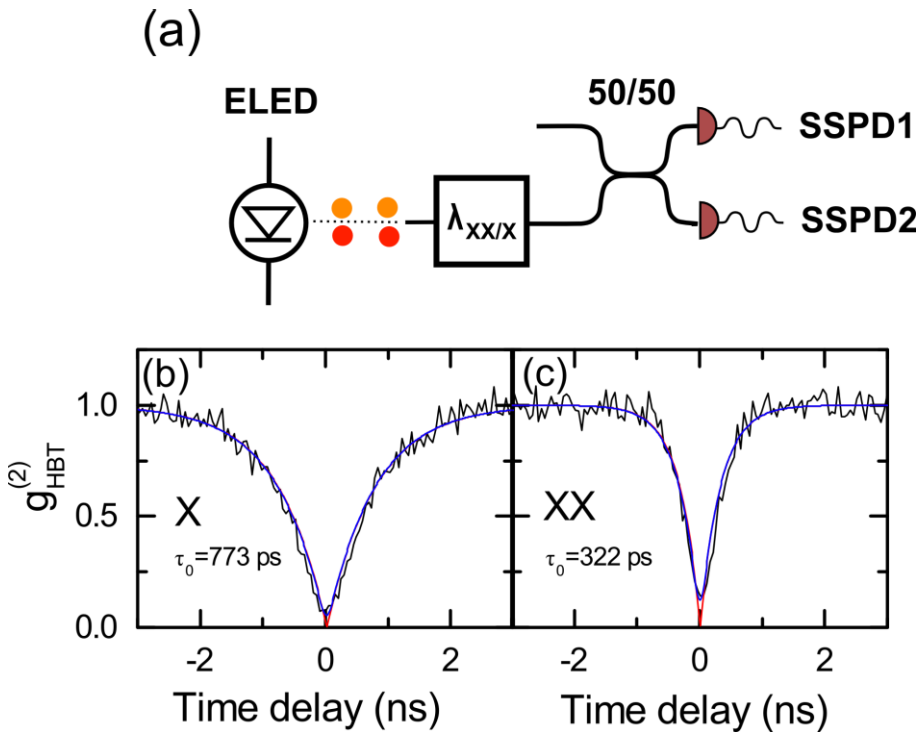

Figure 2.4: (a) Hanbury-Brown-Twiss setup used to measure the second-order correlation function $g^{(2)}_{HBT}(\tau)$. Second-order correlation function for the X (a) and XX (b) transitions respectively. Time constants τ_0 are found from numerical fitting of the simple function $1 - exp(-|\tau|/\tau_0)$.

To conclude our initial characterisation, the identified quantum dot exhibits a very high degree of anti-bunching in the second-order correlation functions for both the XX and X photons, signatures for a high-quality single photon source, and a necessary requirement for a source for future application in quantum logic. Furthermore, the dot has a small fine structure splitting, which is a requirement for the observation of non-classical polarisation correlations. In the following sections we explore how these properties allow us to observe both high degrees of entanglement fidelity and photon indistinguishability in two-photon interference measurements.

2.2.1.2 Entanglement characterisation

Entangled photon pair emission has been demonstrated from quantum dot based light sources under different conditions. Most experiments to date employ optical excitation using lasers[34,35], but entanglement has also been demonstrated under electrical injection conditions[59].

To characterise the entanglement properties of the electrically driven ELED used here the setup schematically shown in figure 2.5 was constructed. Similarly to the Hanbury-Brown-Twiss measurements above, the light from the ELED is first coupled to a fibre system based on polarisation-maintaining (PM) fibre. Monochromators (λ_X, λ_{XX}) isolate the XX and X photons, which then go down separate arms of the system. Polarising beamsplitters (PBS1, PBS2) and superconducting single-photon counting detectors (SSPDs) allow us to simultaneously measure time-resolved co-polarised (SSPD1-SSPD3) and cross-polarised (SSPD2-SSPD3) correlations between the XX and X photons. A half- or quarter-wave plate (WP) at the point of fibre coupling selects the measurement bases of the PBSes. All detection times τ are recorded relative to the detection of one XX photon by detector SSPD3, which is our time reference.

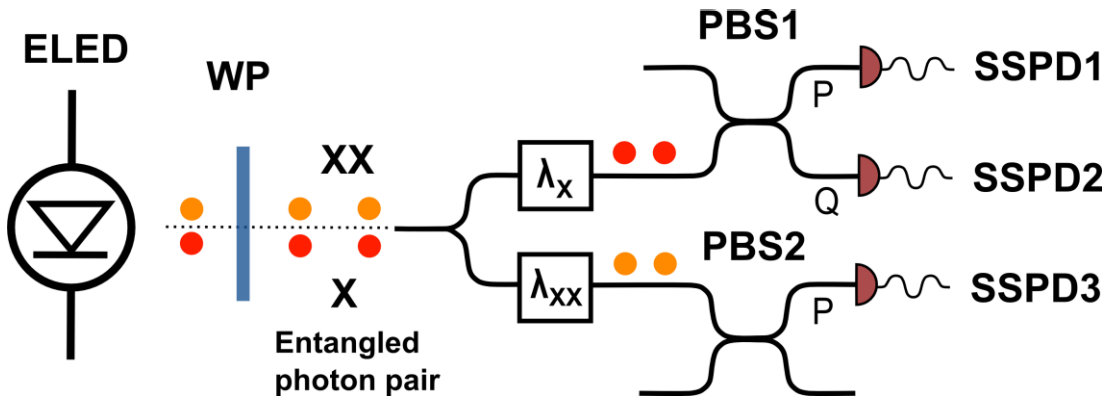

Figure 2.5: Setup for polarisation correlation measurements in a polarisation-maintaining fibre system. Components include quarter-wave plate/half-wave plate (WP), tuneable spectral filters ($\lambda_{XX/X}$) to isolate the X and XX photons, and superconducting single photon detectors (SSPD) detecting orthogonal polarisations P, Q using polarising beamsplitters (PBS).

Ideally, the XX-X photon pair would be emitted into the polarisation Bell-state $|\phi^+\rangle = (|HH\rangle + |VV\rangle)/\sqrt{2}$, where the first label in the ket refers to the XX polarisation and the second refers to the X polarisation. In order to estimate the fidelity of the detected photons onto this state it is sufficient to measure the polarisation correlations in three bases; the linearly polarised exciton eigenbasis (H-V), the diagonal superposition basis (D-A) and the circularly polarised basis (R-L)[46]. By defining the degree of correlation in a polarisation basis P-Q, where P⊥Q:

$$C_{PQ}(\tau) = \frac{g^{(2)}_{PP}(\tau) - g^{(2)}_{PQ}(\tau)}{g^{(2)}_{PP}(\tau) + g^{(2)}_{PQ}(\tau)} \tag{2.10}$$

we can express the fidelity onto the Bell state $|\phi^+\rangle$ as:

$$f^+(\tau) = (1 + C_{HV}(\tau) + C_{DA}(\tau) - C_{RL}(\tau))/4 \tag{2.11}$$

It is worth pointing out eq. 2.11, with eq. 2.10 used for the degree of correlation, is valid only for un-polarised sources. We verify the quantum dot used here to be unpolarised within error.

By re-casting the ideal Bell-state in the three polarisation bases under consideration here, we can see what polarisation correlations to expect:

$$|\phi^+\rangle = (|HH\rangle + |VV\rangle)/\sqrt{2} = (|DD\rangle + |AA\rangle)/\sqrt{2} = (|RL\rangle + |LR\rangle)/\sqrt{2} \tag{2.12}$$

In other words, in the linear bases we would ideally observe co-polarised XX-X pairs, and in the circular basis they should be orthogonally polarised. Figure 2.6 shows the measured time-resolved polarisation correlations (a) in the X polarisation eigenbasis H/V, (b) the diagonal superposition D/A and (c) the circular basis R/L. For small $\tau > 0$, i.e. when the X photon is detected shortly after the XX photon, we observe the predicted correlations with strongly co-polarised photons in the linear bases and strong cross-polarised correlation in the circular basis. For negative τ we observe a dip, which means that it is unlikely for X photons to be emitted just before the XX

photon. We can note that this dip goes very close to zero, on average 5.9% for the three bases compared to about 30% for the first measurements on similar electrically driven devices[59], which can be attributed to the fast SSPDs that better resolve the correlations, and the spatial filtering of the fibre-based system rejecting unwanted background emission just as in the Hanbury-Brown-Twiss measurements above.

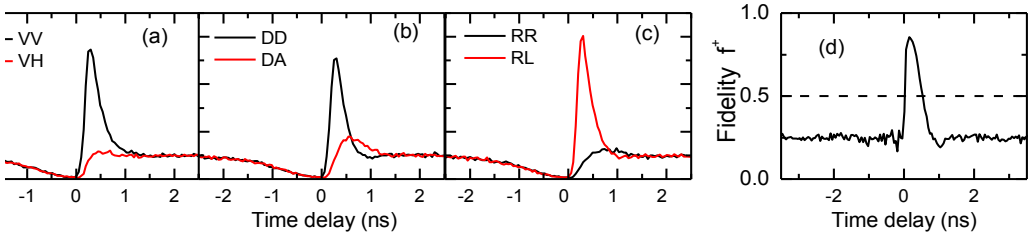

Figure 2.6: Polarisation correlation measurements in (a) X polarisation eigenbasis, (b) diagonal and (c) circular basis. (d) resulting fidelity f^+ to the maximally entangled state $|\phi^+\rangle = (|HH\rangle + |VV\rangle)/\sqrt{2}$ with peak fidelity 0.85±0.01.

Examining panels (a)-(c) we can see some interesting details; at about ~0.5 ns the unwanted DA-correlation is of roughly equal magnitude as the wanted DD-correlation (panel b), while in the X eigenbasis (panel a) the cross-polarised component VH remains small. This is the effect of the non-zero FSS, which manifests itself as an evolution of the entangled state[45] according to

$$|\psi\rangle = \left(|HH\rangle + e^{is\tau/\hbar}|VV\rangle\right)/\sqrt{2} \tag{2.13}$$

where s is the FSS of the X state. In panel (c) we can also see that the circular (cross-polarised) correlations are stronger than the in the linear polarisation bases. This can be explained by considering the randomly fluctuating nuclear (effective) magnetic fields in the quantum dot: the electron in the X states experiences a random Overhauser field at different times of up to a few μeV. Effectively the X eigenstates, and thus polarisation states in 2.13, then tend from linear towards elliptical (the larger Overhauser field the closer to circular). The experimental observations, acquired over much longer time scales than these processes, thus become a time-average over different polarisation eigenstates. The effect for dots with small FSS is a damping of correlations in the linear bases, resulting in stronger correlations in the circular basis[100].

Figure 2.6(d) shows the fidelity to the maximally entangled state $|\phi^+\rangle$ calculated using equations 2.10 and 2.11, reaching a peak value of 0.85±0.01, clearly above the achievable limit of 1/2 using a classically correlated, unpolarised source emitting a mixture of $|HH\rangle$ and $|VV\rangle$. At large detection time differences the fidelity is ~1/4, consistent with completely mixed light as expected when the detected XX and X photons are not correlated.

2.2.1.3 Post-selective two-photon interference

After verifying in the previous section that photons emitted in the *same* excitation cycle are entangled with high fidelity, we will now proceed to describe experiments verifying their indistinguishability, i.e. that it is possible to make photons generated in *different* excitation cycles interfere. This is a pre-requisite for the application of the entangled photons in e.g. quantum teleportation and entanglement swapping protocols.

The coherence properties of the emitted photons are critical for their ability to interfere. Dephasing events in the quantum dot environment such as charge fluctuations in nearby traps or in the wetting layer will render the photons partially distinguishable. The key parameter characterising this is the coherence time, and it was therefore measured by single-photon interference in a Michelson interferometer as described in section 1.4.3. Figure 2.7(a) shows the measured interference fringe visibility as a function of interferometer delay at an injection current of 70 nA/μm^2, the same as used for the entanglement measurements above. The visibility for the XX photon (squares) is found to decay slower than the X photon (triangles), i.e. it has a longer coherence time, and this is systematically observed for dots in these samples. The visibility is shown on a logarithmic scale, and the straight lines (XX red, X blue) indicate that the visibility decay follows an exponential decay very closely, implying a Lorentzian spectral lineshape and homogeneous broadening mechanisms for both photons. Homogeneous broadening is consistent with e.g. charge fluctuations occurring on a time-scale faster than the radiative lifetime, the so-called fast-modulation limit[73]. The crossing with 1/e (dashed line) is defined as the coherence time, and we find 186 ps for the XX photon and 129 ps for the X photon at this current density. To further characterise the behaviour and select appropriate excitation power a small current-dependence study was made, with results presented in figure 2.7(b). In this range, we measure coherence times up to 240 ps for the XX photons, and as one might intuitively expect the coherence time drops with increasing current density.

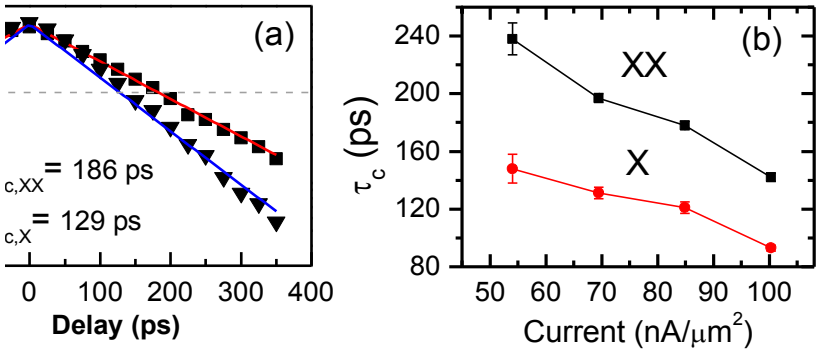

Figure 2.7: (a) Single-photon fringe visibility on a semi-logarithmic scale as a function of time delay between the arms in the Michelson interferometer, measured at current density 70 nA/μm^2. Red and blue lines indicate exponential fits to the XX and X transitions respectively. (b) Photon coherence time plotted versus d.c. current density through the device.

Two-photon interference experiments were performed in a polarisation-maintaining fibre interferometer, schematically depicted in figure 2.8 below. Similar to the entanglement measurements (section 2.2.1.2) a spectral filter $\lambda_{XX/X}$ was first used to select either the X or the XX transitions without narrowing the emission lines. A Mach-Zender interferometer was built using two 50/50 beamsplitters (BS1, BS2) with one arm delayed 2.1 ns to allow photons emitted at different times to meet at BS2. Using polarising beamsplitters (PBS1, PBS2) and super-conducting single-photon detectors (SSPD1-SSPD3) co- and cross-polarised second-order correlations could be measured simultaneously on the output ports of BS2. A quarter-wave plate (WP) was used to align the measurement basis of the PBSs to the circular (R, L) basis. Detections registered by SSPD3 provided our "time zero" reference and co-polarised correlations $g^{(2)}_{TPI}(RR,\tau)$ were measured as a function of detection time delay τ between SSPD1 and SSPD3, whereas the cross-polarised $g^{(2)}_{TPI}(RL,\tau)$ was recorded using SSPD2-SSPD3.

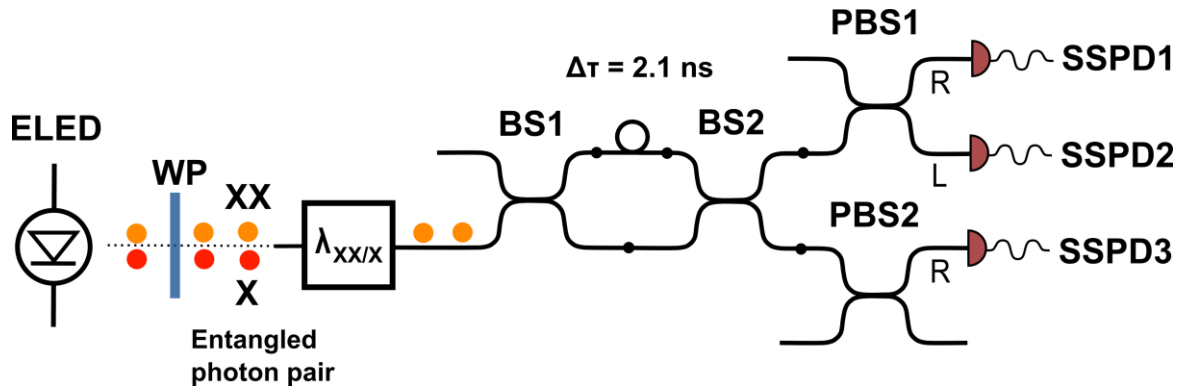

Figure 2.8: Setup based on polarisation-maintaining fibre for two-photon interference correlation measurements in a Mach-Zender type configuration. Components include a tuneable filter to select either the XX or X photons ($\lambda_{XX/X}$), 50/50 beamsplitters (BS1, BS2), a fibre delay line ($\Delta\tau = 2.1$ ns), polarising beamsplitters (PBS) and superconducting single photon counting detectors (SSPD). A quarter-wave plate (WP) is used to align the polarisation axes of the fibre system and thus the detection basis to the circular basis (R, L).

Only when photons arrive simultaneously at BS2 and are indistinguishable in every degree of freedom, including the polarisation, can they interfere. Consequently two-photon interference will manifest itself in the co-polarised correlations, while for the cross-polarised $g^{(2)}_{TPI}(RL,\tau)$ the photons are perfectly distinguishable and do not interfere which provides a baseline with which we can compare and quantify the amount of interference.

Figure 2.9(a) shows the measured co- and cross-polarised second-order correlation functions for XX input photons. The cross-polarised case $g^{(2)}_{TPI}(RL,\tau)$ has been offset by 0.25 for clarity. The central dip in $g^{(2)}_{TPI}(RL,\tau)$ which goes to ~1/2 is solely due to the anti-bunched nature of the source, and reflects the suppression of two photons emitted simultaneously and then propagating down the same path of the Mach-Zender interferometer. With probability 1/2 two photons emitted at different times can take different paths, and these account for the remaining ~1/2 at $g^{(2)}_{TPI}(RL,0)$. The dips to ~3/4 at ±2.1 ns are also due to the sub-Poissonian emitter, causing a suppressed probability of photons being emitted simultaneously and travelling down different paths of the interferometer.

Shown together with $g^{(2)}_{TPI}(RL,\tau)$ are also modelled correlations, taking the above described ways to detect two photons into account:

$$g^{(2)}_{TPI}(RL,\tau) = \frac{1}{2}g^{(2)}_{HBT}(\tau) + \frac{1}{4}\left(g^{(2)}_{HBT}(\tau+\Delta\tau) + g^{(2)}_{HBT}(\tau-\Delta\tau)\right) \qquad (2.14)$$

For $g^{(2)}_{HBT}(\tau)$ we take the numerical fits presented before in section 2.2.1.1. The blue dashed curve shows the calculation based on eq. 2.14 which would be observed with perfect detector response. The red trace shows the simulated correlations after convolving the ideal case with the experimentally measured detector response function (Gaussian, FWHM~140 ps).

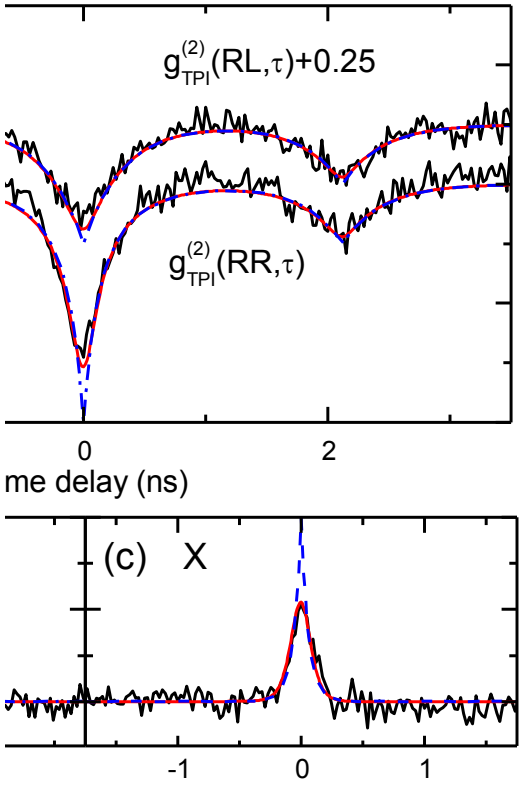

Figure 2.9: (a) Second-order correlation functions measured for co-polarised (RR) and cross-polarised (RL) XX photons. Cross-polarised correlations offset by 0.25 for clarity. The corresponding measurements for X photons look very similar and is not shown. (b) Two-photon interference visibility for XX photons, (c) visibility for X photons. Blue dashed curves shows theoretical model assuming perfect detectors, red curves shows theoretical model with the experimentally measured detector pair responses.

Now that we understand the appearance of the correlations for non-interfering, cross-polarised photons, we can turn our attention to the co-polarised, interfering, photons. To take the quantum interference into account we can modify expression 2.14 using the theoretical coincidence probability $P(\tau) = 1/2 \cdot (1 - \exp(-2|\tau|/\tau_c))$ previously derived (eq. 2.7, section 2.1.2). Remembering that this is a probability conditional upon the presence of two photons in the input ports of the interference beamsplitter BS2, we only need to change the second term in eq. 2.14 which represents photons in different paths of the interferometer:

$$g^{(2)}_{TPI}(RR,\tau) = \frac{1}{2} g^{(2)}_{HBT}(\tau) + \\ + \frac{1}{4}\left(g^{(2)}_{HBT}(\tau + \Delta\tau) + g^{(2)}_{HBT}(\tau - \Delta\tau) \right) \cdot (1 - \exp(-2|\tau|/\tau_c)) \tag{2.15}$$

Any interference occurring will be observed for $\tau \sim 0$, and upon inspection of $g^{(2)}_{TPI}(RR,\tau)$ in figure 2.9(a) we see that the central dip indeed extends to 0.27±0.02, much deeper than in the cross-polarised case. Again the blue dashed curve represents the simulated correlations for perfect detectors, and we can note that due to the strongly anti-bunched source the dip extends to zero. The red curve which takes the detector time resolution into account fits excellently to the experimentally measured correlations, without any free fitting parameters. Two-photon interference using the X photon was also performed with very similar results. The correlation functions look almost identical to the ones in figure 2.9(a) and are therefore not shown.

In order to quantify our results, we define an interference visibility as

$$V_{TPI}(\tau) = \frac{g^{(2)}_{TPI}(RL,\tau) - g^{(2)}_{TPI}(RR,\tau)}{g^{(2)}_{TPI}(RL,\tau)} \tag{2.16}$$

Figures 2.9(b-c) show the visibility as a function of detection time delay for XX photons (panel b) and X photons (panel c). For long delays the visibility is zero, i.e. the photon wavepackets do not interfere since they do not even overlap on the beamsplitter, but as we approach zero the visibility increases and reaches a maximum of 0.57±0.03 for the XX photons and 0.52±0.03 for X, indicating that a majority of the photons interfere when detected simultaneously. The shorter coherence time of the X photons manifests itself as a slightly narrower visibility peak. The modelling (red curves) again fits excellently to the experiments, and essentially unit visibility could be achieved with perfect detectors (blue, dashed curves) owing to the low $g^{(2)}_{HBT}(0)$.

It is a remarkable result that despite the d.c. excitation and consequently the random overlaps in time of photon wavepackets on BS2, the post-selected interference visibility is mainly limited by the photon coherence time and the detector resolution, and this has been demonstrated before[79,80,93]. However, two-photon interference with quantum dots has mostly focussed on charged transitions[79,80,97], and in contrast here we show high levels of indistinguishability of photons that are part of entangled pairs. In section 2.3 we discuss the implications of this for quantum teleportation and entanglement swapping, and in chapters 3-4 we demonstrate that these properties indeed are sufficient for quantum teleportation.

2.2.2 Towards a.c. generation

2.2.2.1 Device characteristics in A.C. operation

Arguably a larger-scale implementation of an optical quantum information machine will likely employ pulsed sources, so that the emission is triggered and the detection of photons can be synchronised and gated. This is the way that small-scale implementations of quantum logic with spontaneous parametric down-conversion (SPDC) sources have been realised[53,85].

Motivated by this fact a.c. operation of the ELED is explored in this section. A sinusoidal driving voltage of frequency 476 MHz super-imposed on a d.c. voltage was used, with frequency chosen to match the delay line of the Mach-Zender interferometer. Figure 2.10(a) shows the XX coherence time as a function of the a.c. voltage amplitude. After 0.5V there is a clear drop in coherence time. Examining panel (b) we can see the cause of this; at higher a.c. voltages a Stark-shift at a frequency comparable to the radiative lifetime is induced[101], causing significant broadening that can be easily detected even directly in the spectral domain. To avoid this, we choose to work at an a.c. amplitude of 0.5V. Figure 2.11 shows the time-resolved electroluminescence of the XX transition at these conditions, exhibiting rather clear pulsed appearance. For the X photon however, we do not achieve such pulsed characteristics. The difference can be attributed to an overall super-linear power dependence of the XX emission, caused by both the non-linear IV characteristics of the diode and the quadratic power dependence of the XX intensity.

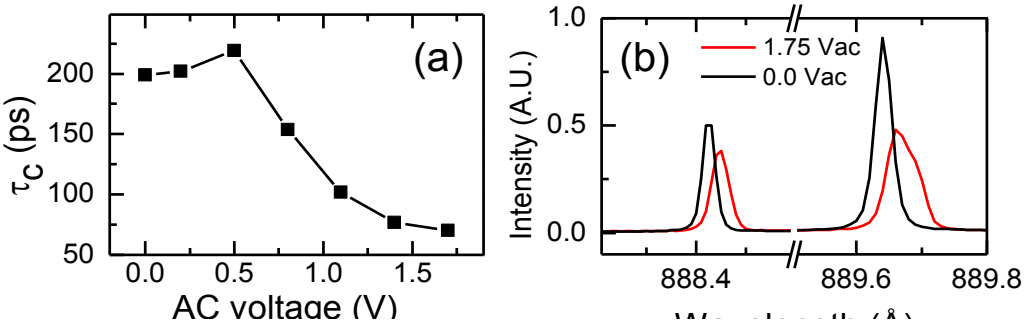

Figure 2.10: (a) Coherence time of XX photon as a function of AC voltage amplitude. (b) Electroluminescence spectra for 0 V ac amplitude and 1.75 V ac amplitude.

Figure 2.11: Time-resolved electroluminescence for the XX photon showing fairly good pulsed characteristics.

2.2.2.2 Characterising entanglement and two-photon interference

The XX-X polarisation correlation and two-photon interference experiments described in sections 2.2.1.2 and 2.2.1.3 above were repeated under a.c. excitation conditions. Figures 2.12 shows the resulting entanglement fidelity which is very similar to what was measured in d.c. conditions, reaching a peak value of 0.87 ± 0.04 (d.c.: 0.85 ± 0.01). Figure 2.13(a) on the other hand, showing the two-photon interference correlations, differs significantly from d.c. due to the modulated excitation. Several peaks separated by 2.1 ns corresponding to the pulse repetition period can be seen. Although they are not completely separated the valleys extend to roughly half of the peak values. For a high quality pulsed source with completely indistinguishable photons the central peak in $g^{(2)}_{RR}(\tau)$ would be completely absent, since photons would always be emitted one by one, always arrive perfectly synchronised at BS2, and be perfectly indistinguishable over the whole photon wavepacket. Here we clearly have something intermediate between a d.c. and pulsed source; the central peak around $\tau \sim 0$ bears clear witness of interference in the co-polarised correlations, with the dip extending significantly deeper than in the cross-polarised case, but then as τ increases $g^{(2)}_{RR}(\tau)$ swings up first up, as photons are arriving either not at the same time or do not interfere due to decoherence, then down again as the intensity goes down. The post-selected two-photon interference visibility of the XX photons, shown in figure 2.13(b), is slightly higher than in d.c., possibly due to reduced re-excitation, reaching 0.60±0.05 (d.c.: 0.57±0.04).

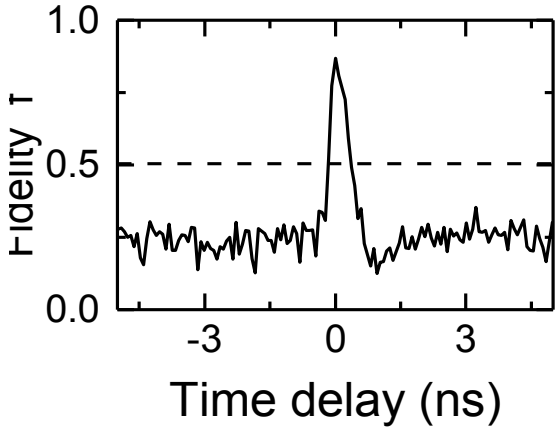

Figure 2.12: Entanglement fidelity of the XX-X photon pair in a.c. driving conditions.

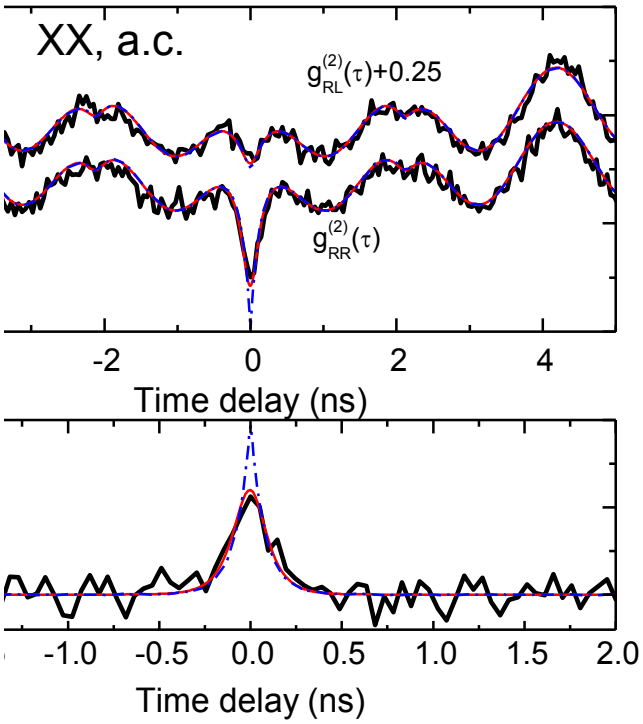

Figure 2.13: (a) Second-order correlation functions for XX photons in a.c. operation. (b) two-photon interference visibility, with a maximum of 0.60±0.05.

2.3 Two-photon interference, quantum teleportation and entanglement swapping

2.3.1 Quantum teleportation

Quantum teleportation[13,14] will be described in more detail in chapters 3 and 4, but here we will very briefly discuss it to put the above discussed experimentally achieved entanglement fidelities and two-photon interference visibilities in a context and relate them to an application.

In quantum teleportation one qubit (here a photon) is destroyed so that its information can be transferred to another target qubit. This is achieved by performing a joint measurement on the input qubit and one photon from an entangled pair (the ancilla), projecting them onto one of the four Bell states, with the second qubit in the entangled pair constituting the target. Two-photon interference plays a key role in the Bell state projective measurement, since the input and ancilla photons are made to interfere on a 50/50 beamsplitter (see figure 2.14).

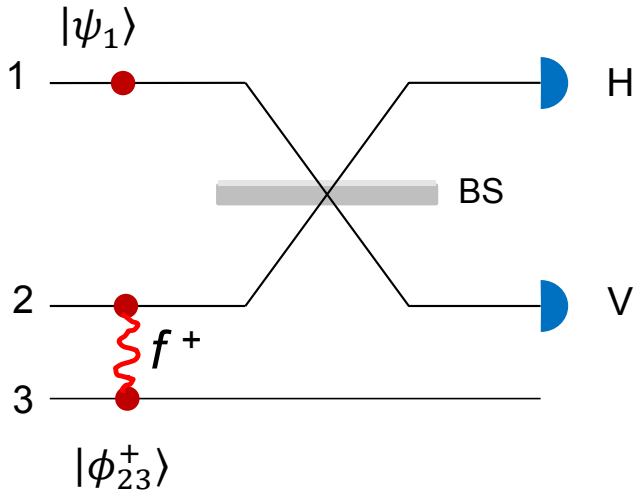

Figure 2.14: Schematic of the quantum teleportation protocol. The photon carrying the input qubit is in mode 1 and the entangled photon pair mediating the teleportation occupies modes 2 and 3. The balanced beamsplitter (BS) and the detectors perform a Bell-state measurement, which signals successful teleportation of $|\psi_1\rangle$ to mode 3 when the two detectors click.

Here, we simplify the picture by only considering the post-selected entanglement fidelity and interference visibility, and furthermore considering the two-photon state as a mixture of a fraction k of the ideal entangled state $|\phi^+\rangle = (|HH\rangle + |VV\rangle)/\sqrt{2}$ and a fraction $(1-k)$ completely mixed fraction:

$$\rho_{23} = k \cdot |\phi^+\rangle\langle\phi^+| + (1-k)\mathbb{I}/4 \tag{2.17}$$

where $\mathbb{I}$ is the identity matrix. We can relate the constant k to the measured fidelity f^+ through

$$\begin{gathered}\langle\phi^+|\rho_{23}|\phi^+\rangle = k + (1-k)/4 = f^+ \\ k = (4f^+ - 1)/3\end{gathered} \tag{2.18}$$

In quantum teleportation we must also consider the input photon in mode 1, which is assumed to be in the pure state $|\psi_1\rangle = \alpha|H_1\rangle + \beta|V_1\rangle$ so that the total system density matrix becomes

$$\rho_{123} = \rho_1 \otimes \rho_{23} = (|\psi_1\rangle\langle\psi_1|) \otimes \rho_{23} \tag{2.19}$$

The Bell state measurement performed on the input and ancilla photons projects the modes 1 and 2 onto the state $|\psi^-{}_{12}\rangle = (|H_1V_2\rangle - |V_1H_2\rangle)/\sqrt{2}$[14]. The target photon in mode 3 is then projected into the state

$$\begin{aligned} \rho_3' &= \frac{\langle\psi^-{}_{12}|\rho_{123}|\psi^-{}_{12}\rangle}{\mathrm{Tr}\,\langle\psi^-{}_{12}|\rho_{123}|\psi^-{}_{12}\rangle} \\ &= k \cdot |\psi_3'\rangle\langle\psi_3'| + (1-k)\cdot\frac{1}{2}(|H_1\rangle\langle H_1| + |V_1\rangle\langle V_1|) \end{aligned} \tag{2.20}$$

where the first term is the expected output state

$$|\psi_3'\rangle = -\beta|H_3\rangle + \alpha|V_3\rangle \tag{2.21}$$

which is orthogonal to the input state, and differs systematically by only a unitary transformation (correctable with a combination of waveplates). The second term in eq. 2.20 represent completely mixed light in the output mode, when the entanglement "fails". The fidelity of ρ_3' to the expected output state is trivially

$$f_P = \langle\psi_3'|\rho_3'|\psi_3'\rangle = k + \frac{1-k}{2} = \frac{k+1}{2} \tag{2.22}$$

The Bell-state projective measurement is a crucial step and depends on the photons interfering. If we take the two-photon interference used in previous sections as the probability of them interfering we arrive at a teleportation fidelity of:

$$f = V \cdot f_P + \frac{1}{2}(1-V) = \frac{V\cdot(4f^+ - 1) + 3}{6} \tag{2.23}$$

This expression is intuitively reasonable; with no interference but perfect entanglement ($V = 0, f^+ = 1$) or with perfect interference but no entanglement ($V = 1, f^+ = 1/4$) the maximum fidelity is $1/2$. Both interference and entanglement are needed for teleportation to be successful. Figure 2.15 shows the calculated teleportation fidelity as a function of entangled-pair fidelity f^+ and visitbility V. Taking the experimentally achieved entanglement fidelity ($f^+ = 0.87$) and two-photon interference visibility ($V = 0.6$) a teleportation fidelity of ~0.75 is predicted, significantly above the limit for no information transfer $1/2$.

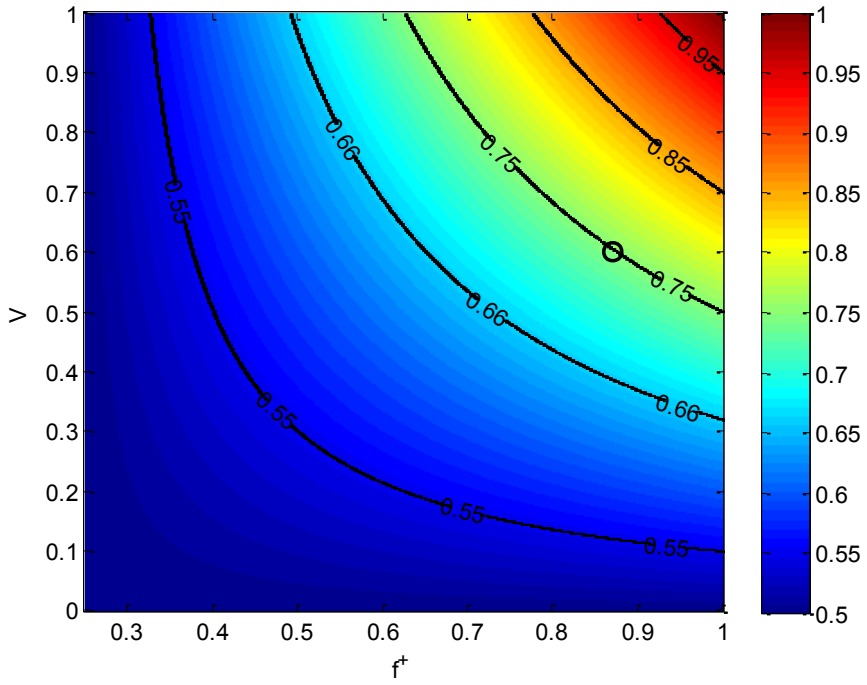

Figure 2.15: Quantum teleportation fidelity as a function of entanglement fidelity f^+ and interference visibility V. The position of the experimentally achieved fidelity and visibility ($f^+ = 0.87, V = 0.6$) is marked with a black ring, and a teleportation fidelity of 0.75 is predicted.

2.3.2 Entanglement swapping

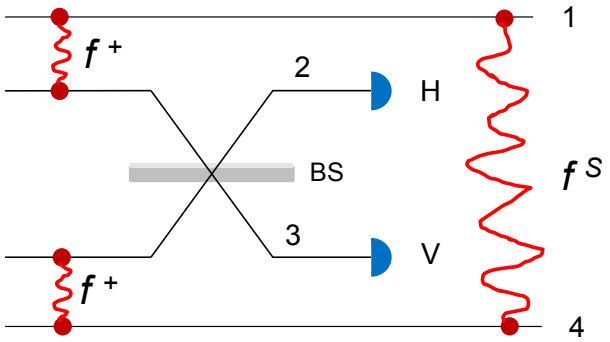

Figure 2.16: Schematic of entanglement swapping protocol.

A similar analysis to the one in the preceding section can be applied to entanglement swapping, a slightly more complex protocol which is essentially the same as quantum teleportation, except the input photon itself is part of an entangled pair. The protocol is schematically drawn in figure 2.16 above. The Bell-state projective measurement on the balanced beamsplitter (BS in the figure) has the interesting result of creating entanglement between the two photons (modes 1 and 4) that did not participate in the measurement, projecting them onto the state $|\psi^-{}_{14}\rangle = (|H_1V_4\rangle - |V_1H_4\rangle)/\sqrt{2}$. Entanglement swapping has important applications in for example quantum repeaters for long-distance quantum communication networks[102].

Repeating the analysis in complete analogy with that for teleportation, and calculating the fidelity of the created entangled pair onto the expected entangled output state $|\psi^-_{14}\rangle$, we get

$$f^S = V \cdot \left((f^+)^2 + \frac{(1-f^+)^2}{3} \right) + \frac{1-V}{4} \tag{2.24}$$

Figure 2.17 shows the estimated fidelity f^S as a function of input fidelity f^+ and visibility V. By once again inserting our experimentally measured fidelities and visibilities we can estimate an achievable fidelity of $f^S = 0.56$. This is above the fidelity of 1/2 achievable if modes 1 and 4 were occupied by unpolarised but classically correlated photons, but it is clearly significantly more difficult to achieve entanglement swapping than teleportation due to the involvement of two entangled pairs. Considering the relatively crude simplifications made in the analysis presented here, we must conclude that in order to achieve convincing entanglement swapping results in a realistic experimental setting, more substantial improvements of the ELED would need to be made.

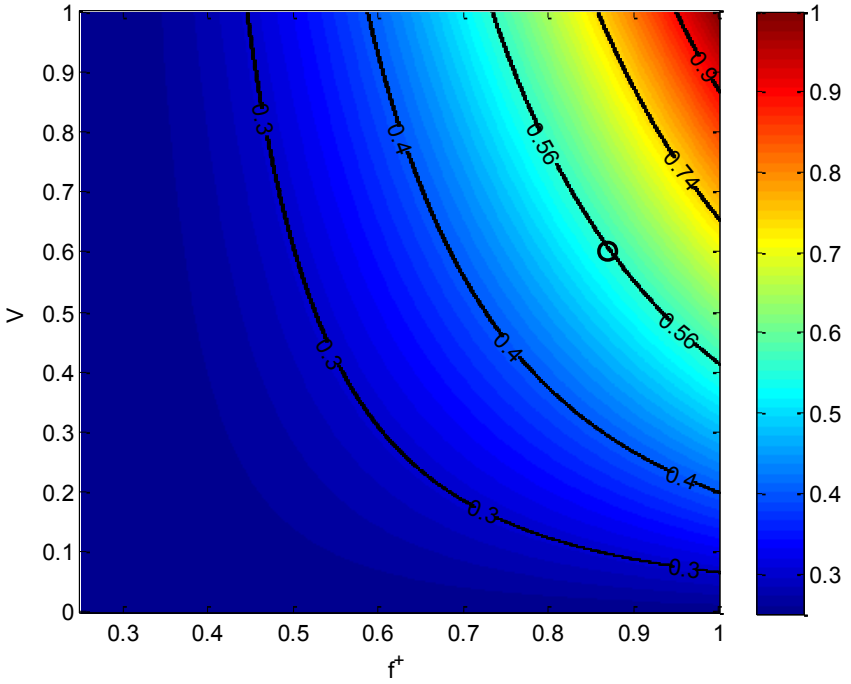

Figure 2.17: Fidelity f^S of the entangled pair created in an entanglement swapping operation as a function of incoming photon pair fidelity f^+ and interference visibility V. The position of the experimentally achieved fidelity and visibility ($f^+ = 0.87, V = 0.6$) is marked with a black ring, for which a fidelity of 0.56 is predicted.

2.4 Discussion

In this chapter it was shown that photons from an entangled-light-emitting diode originating from the same excitation cycle can be entangled, with a peak observed fidelity of 0.87 ± 0.04, and photons emitted in different excitation cycles can interfere, with the highest observed interference visibility being 0.60 ± 0.05.

The limited exploration of a.c. driving modes illustrated the difficulty in achieving strongly pulsed operation with low probability of re-excitation later in the same excitation cycle, and to achieve highly coherent photons. The time-dependent Stark shift observed for strong a.c. voltages (figure 2.10) has actually been used in conjunction with narrow spectral filtering to achieve strongly pulsed single-photon emission[80], albeit with reduced detected photon count rate so it cannot be considered a generally applicable method. In order to make significant progress towards a fast, pulsed single-photon device further engineering of the electrical device characteristics would be necessary, for example by making smaller area devices with lower capacitance[103,104].

Purcell enhancement of quantum dot emitters placed in optical cavities can be used to combat the problem of decoherence and improve the indistinguishability of the photons, thereby moving towards two-photon interference with no or minimal time post-selection or gating[32,105]. As a bonus this would also reduce the negative influence of the exciton fine-structure splitting on entanglement[34]. Resonance fluorescence[106] techniques represent another interesting recent development and have been used to generate extremely long coherence times of up to 22 ns[107], excellent sub-Poissonian emission[107] and almost unity interference visibility[108] has been demonstrated. These techniques are however very sophisticated and require per definition a high-quality driving laser, making the prospect of miniaturization of devices questionable.

The ending analysis (sections 2.3.1-2.3.2) of requirements in terms of entanglement fidelity and interference visibility for the quantum teleportation and entanglement swapping protocols indicated that teleportation with an appreciable fidelity should be feasible, while entanglement swapping may still be out of reach for the devices studied here. In the next chapter, we shall see how the ELED indeed enables quantum teleportation to be realised in a photonic circuit.

3 Quantum teleportation using a light-emitting diode

3.1 Introduction

3.1.1 Teleporting a quantum state using non-classical correlations

The so-called 'no-cloning theorem' states that a quantum state cannot be perfectly cloned. It is possible for a chosen fixed set of orthogonal states $|0\rangle$ and $|1\rangle$, but a cloning machine for arbitrary states $\alpha|0\rangle + \beta|1\rangle$ is not compatible with the superposition principle, a cornerstone of quantum mechanics[109,110]. This may be a complication in quantum information science, but it is worth pointing out that quantum key distribution (QKD) actually relies directly on the no-cloning theorem; since perfect cloning of arbitrary quantum states is not possible this makes the formation of unconditionally secure communication channels possible. Any eavesdropper attempting to clone (and read) qubits exchanged by two parties will by necessity introduce some noise on the channel, which can be detected by the legitimate parties[111].

Quantum teleportation, first proposed in 1993 by Bennett et al[13], circumvents the no-cloning theorem and permits a quantum state to be perfectly copied from one particle to another - regardless of their spatial separation - with the crucial caveat that the input state is destroyed and no information is gained about it. For this feat non-classically correlated states must be shared between the sender and receiver. In 1997 Anton Zeilinger's group in Austria was the first to realize quantum teleportation in the lab, using photonic polarisation qubits and polarisation-entangled photon pairs generated by spontaneous parametric down-conversion (SPDC)[14]. Following the first demonstration of quantum teleportation parts of the quantum optics community have been involved in a constant competition towards teleportation over ever longer distances both over fibre[112–114] and free-space[115–117] links, or making other technical improvements such as detecting more than one of the Bell states[112,118] (and thus improving the upper limit to the success probability of the protocol). Fundamentally, though, the development of entangled light sources for all-optical experiments has been limited in the sense that modern experiments still rely on SPDC[115,116] which suffer from multi-photon emission events[54].

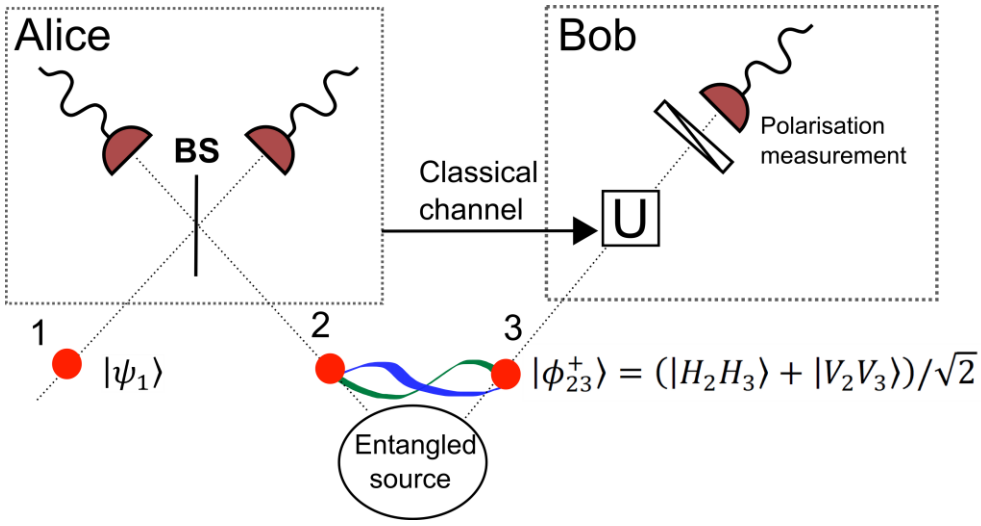

Figure 3.1: Schematic of quantum teleportation protocol.

To see the basic working principle of optical quantum teleportation, consider figure 3.1 above. Here we shall only concern ourselves with teleportation of qubits encoded on the polarisation degree of freedom, similar to the first implementation of the protocol[14]. Teleportation begins with the distribution of an entangled photon pair between two nodes, conventionally called Alice and Bob. The entangled pair occupies modes 2 and 3, and is here assumed to be in the Bell state $|\phi_{23}^+\rangle = (|H_2H_3\rangle + |V_2V_3\rangle)/\sqrt{2}$ (which is also the state of the biexciton-exciton pair ideally emitted by a quantum dot). Alice receives the photon in mode 2 and the input (control) photon in mode 1, which carries an arbitrary polarisation state $|\psi_1\rangle = \alpha|H_1\rangle + \beta|V_1\rangle$ to be teleported. The joint three-photon state is then

$$\begin{aligned} |\psi_1\rangle|\phi_{23}^+\rangle = \frac{(\alpha|H_1H_2H_3\rangle + \alpha|H_1V_2V_3\rangle + \beta|V_1H_2H_3\rangle + \beta|V_1V_2V_3\rangle)}{\sqrt{2}} = \\ = \frac{|\phi_{12}^+\rangle}{2}\cdot(\alpha|H_3\rangle + \beta|V_3\rangle) + \\ \frac{|\phi_{12}^-\rangle}{2}\cdot(\alpha|H_3\rangle - \beta|V_3\rangle) + \\ \frac{|\psi_{12}^+\rangle}{2}\cdot(\alpha|V_3\rangle + \beta|H_3\rangle) + \\ \frac{|\psi_{12}^-\rangle}{2}\cdot(\alpha|V_3\rangle - \beta|H_3\rangle) \end{aligned} \tag{3.1}$$

where in the last step the state has been re-written in the Bell-state basis of modes 1 and 2, spanned by the four states $|\phi_{12}^\pm\rangle = (|H_1H_2\rangle \pm |V_1V_2\rangle)/\sqrt{2}$ and $|\psi_{12}^\pm\rangle = (|H_1V_2\rangle \pm |V_1H_2\rangle)/\sqrt{2}$. In the original protocol[14] Alice performs a joint measurement on the photons in mode 1 and 2 using a 50:50 beamsplitter (BS in figure 3.1). When her two detectors register a coincidence no information is gained about the individual states of mode 1 and 2, but the joint state is projected onto $|\psi_{12}^-\rangle$. From eq. 3.1 we see that particle 3 (the target) must then be in the state $|\psi_3\rangle = \alpha|V_3\rangle - \beta|H_3\rangle$, which differs from the input state $|\psi_1\rangle$ by a trivial unitary transformation, correctable with a waveplate.

From the probability amplitudes in eq. 3.1 we see that this projective measurement by Alice only succeeds 1/4 of the time, but crucially Alice will know when it succeeds when she

registers a coincidence, and can signal this to Bob using a classical information channel (see figure 3.1). It is impossible to detect all four Bell states without errors when using only linear optics, only $|\psi_{12}^{+}\rangle$ and $|\psi_{12}^{-}\rangle$ can be detected without ambiguity[119] which limits the theoretical success probability to 1/2. In the successful cases Alice can feed forward to Bob the information of which state was detected, and he can according to Alice's signal apply the appropriate unitary transformation U to ensure he will receive the correct state, without actually knowing what the state is[13,115]. In order to resolve all Bell states analysers based on non-linear optics have been used, although with very small success probability due to the weak non-linear effects[118].

To summarise, quantum teleportation is a method for copying quantum information from one qubit onto another without any involved party learning anything about the quantum state, and where the original copy is destroyed. The process consumes entangled resource states that are used to mediate the transfer through their non-local correlations, and in addition teleportation requires a classical communication (feed-forward) channel. As we shall see in the next section teleportation finds important applications in quantum information applications.

3.1.2 Teleportation in quantum communication and computing

If quantum teleportation destroys the input state in order to copy it onto the target qubit, then one may ask the question what the point of the whole operation is, especially since a classical message signalling success must also be sent. After all, why not just send the input qubit to Bob? This question naturally brings us close to one possible application: quantum teleportation can be used to extend the range of quantum communication networks used for example for quantum key distribution (QKD). Figure 3.2 shows a schematic illustrating how a chain of quantum relays[113,120] can be used to improve the signal to noise ratio at Bob's end; each quantum relay node comprises an entangled pair source and a Bell-state analyser, just as the basic teleportation protocol described above. It operates by performing the Bell-state measurement (BSM) on the input photon and one of the entangled photons, teleporting the input state onto the output. A heralding signal from the BSM is passed down the chain of relays, accompanying the qubit photon as it propagates down the link. At the end-point this heralding signal enables the receiver (Bob) to discard any detection events in which the signal photon was lost along the link, thereby achieving a higher signal to noise ratio for the events he considers. Note that a relay node (and the quantum teleportation protocol) can be interpreted as a quantum non-demolition (QND) device; a successful BSM signals the presence of a photon on the input, but the device allows the state to propagate to the output un-harmed and without reading the state. Quantum relays have been implemented in some variations, for example using weak pulses of down-converted photon pairs[113], down-converted CW laser photons[121] and using telecom-band photons generated through four-wave-mixing in fibres[122].

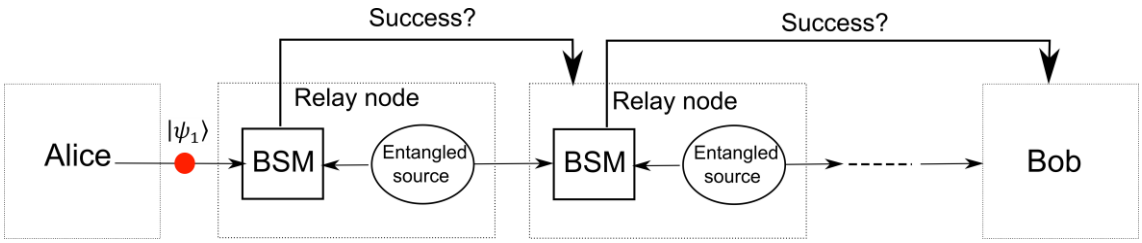

Figure 3.2: Operation principle of a chain of quantum relays linking Alice and Bob.

While the quantum relay described above can improve the SNR of the communication by heralding the successful transmission of the qubit, it does not correct for decoherence of qubits along the transmission line and it does not improve the overall signal strength (qubit rate) at the receiving end. The quantum repeater addresses both of these problems[102,123]. The initial goal for a communication channel using quantum repeaters is to establish entanglement between the sender and receiver. This is done in a nested fashion, first for the nearest neighbour repeater nodes and then further and further afield. To this end, each station in the network must be equipped with a high fidelity, high efficiency quantum memory (QM), an entangled light source and a Bell state analyser. All of these components are extremely challenging to implement with today's technology, with the quantum memories being perhaps the main challenge, but some progress has been made using single atom memories[124], cold atom gases[125], quantum dots[36] and NV-centers[18]. Prototypical quantum repeaters for single photon qubits have been implemented[126,127], but still the quantum relay at the moment appears to be a much more feasible endeavour.

Teleportation also plays a central role in linear optics quantum computing proposals[84,128,129] as it allows the realisation of quantum logic gates with success rates arbitrarily close to one[129]. Provided that one can implement a set of universal gates, such as single-qubit rotations plus a two-qubit gate such as the CNOT gate (which flips one qubit, 'target', dependent on the state of another qubit, 'control'), one can in principle implement any multi-qubit unitary transformation, i.e. one can construct a quantum algorithm[130]. Two-qubit gates present significant challenges since photons do not interact with each other, and nonlinear optical processes that could provide the interaction are very weak and inefficient. With linear optics components two-photon interference can provide our "interaction", which allows for example the CNOT gate to be realised[68,131]. Unfortunately, such two-qubit gates are probabilistic with limited success probability which renders them not scalable, but luckily sacrificial single-photon ancillae can at least tell us *when* the gate succeeded. Gottesman and Chuang introduced the concept of "teleporting the qubits through the gate" to make the gates in principle deterministic[84]. The principle is schematically shown in figure 3.3. The CNOT gate is repeatedly applied on qubits (modes 3 and 4) from two entangled pairs ($|\Phi_{23}^{+}\rangle$ and $|\Phi_{45}^{+}\rangle$) until it succeeds, after which the control $|C_1\rangle$ and target $|T_6\rangle$ qubits are teleported onto the CNOT output qubits $3'$ and $4'$. With just a few single-qubit rotations (X, Z in the figure) dependent on the feed-forward from the Bell-state measurement devices the two qubits emerging at the very end (7-8) will be in the desired state $CNOT|C,T\rangle$. This type of gate has been elegantly demonstrated using SPDC sources and free-space optics[53].

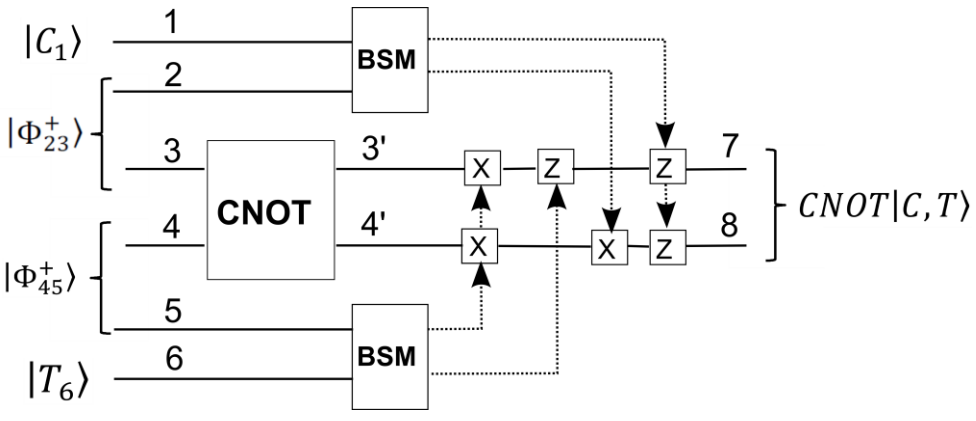

Figure 3.3: Schematic drawing of a teleportation-based CNOT gate, incorporating a probabilistic CNOT gate repeatedly applied on entangled resource states until success, after which the control and target qubits are teleported onto the output modes. After a series of single-qubit rotations (X, Z) the intended output state $CNOT|C,T\rangle$ emerges.

As seen from the above examples, quantum teleportation is a very important primitive for quantum information applications in the way it builds on a combination of entanglement, quantum interference effects and measurements to create desired qubit operations. In addition, it is perhaps one of the most striking manifestations of non-local correlations and arguably something that is expected to be demonstrated for an entangled light source. In this chapter we shall see how the two-photon interference and entanglement properties presented in chapter 2 were brought together to implement the first photonic quantum teleporter with an electrically driven light-emitting diode[132].

3.2 Experimental

3.2.1 Fibre-based teleporter

We implement our teleportation circuit using single-mode fibre components and the entangled-light-emitting diode (ELED)[59], already shown to be capable of generating high fidelity entangled photons with appreciable degrees of interference (chapter 2 and Stevenson et al[133]). The setup is schematically drawn in figure 3.4 below. The light from the ELED is coupled to the single mode fibre and passed through a tuneable transmission grating filter (F) separating the X and XX photons from the rest of the emission, without reducing their bandwidth. As described in the previous section, teleportation begins with the distribution of entangled photons between two parties Alice and Bob. Using a 50/50 beamsplitter (BS1) we distribute half of the XX photons to Alice. These photons are termed the ancillae (XX_a) and will mediate the teleportation. The other half of the XX photons, called control photons (XX_c), are sent down the other arm of the setup and prepared in a desired polarisation state using a polarising beamsplitter (PBS1) and an electronic polarisation controller EPC1. The control photons XX_c carry the state to be teleported. The state preparation arm also incorporates a delay of 2.5 ns to allow photons from different excitation cycles of the quantum dot to meet at BS2. It should be pointed out that although the control photon in this experiment originates from the same source as the ancilla, and is prepared in the same circuit, the teleportation protocol is in principle compatible with independent sources. This will be demonstrated in chapter 4.

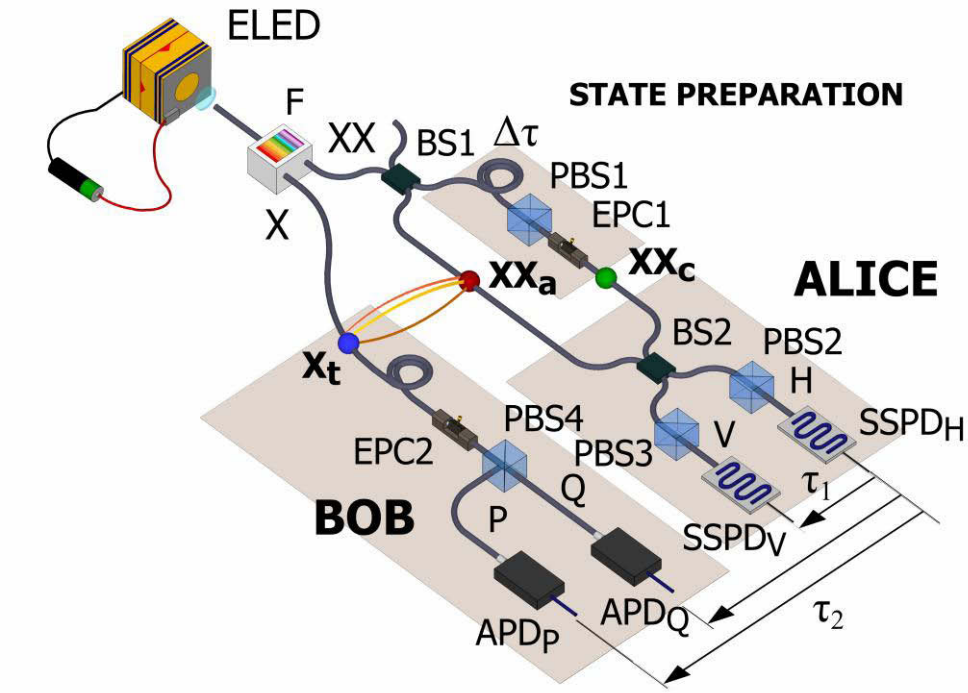

Figure 3.4: Schematic of the fibre-based teleportation setup, with ELED, spectral filter (F), 50/50 beamsplitters (BS), polarising beamsplitters (PBS), electronic polarisation controllers (EPC), superconducting single-photon detectors (SSPD), avalanche photodiodes (APD). Alice performs a Bell-state projective measurement on the control photon (XX_c) and the ancilla (XX_a) entangled with the target photon (X_t) received by Bob.

Alice receives both ancilla XX_a and target XX_c, and performs a joint measurement on them using a second beamsplitter (BS2) and superconducting single-photon detectors ($SSPD_V$, $SSPD_H$) set to measure polarisations H and V using polarising beamsplitters PBS2, PBS3 and electronic polarisation controllers (not shown). A coincidence registered by Alice signals a successful Bell-state measurement, projecting the ancilla and control photons onto the Bell state $|\psi_{ac}^-\rangle = (|H_a V_c\rangle - |V_a H_c\rangle)/\sqrt{2}$. The X photon, or target (X_t), forms an entangled pair together with the ancilla XX_a, and is sent to the receiver Bob. Bob is in possession of two APDs interrogating the polarisation state of X_t in the polarisation basis P-Q (with P orthogonal to Q) using PBS4 and EPC2 to set the basis.

Experimentally, fast correlation electronics are used to record three-fold detections events ($SSPD_H$-$SSPD_V$-APD_P and $SSPD_H$-$SSPD_V$-APD_Q), with all detection times registered relative to detections by Alice's detector $SSPD_H$. We call the time delay between Alice's detectors $SSPD_H$-$SSPD_V$ τ_1, and τ_2 signifies the relative detection time of either of Bob's detectors ($SSPD_H$-APD_P or $SSPD_H$-APD_Q). The time resolution of the detector pairs was measured to be $SSPD_H$-$SSPD_V$: 103 ±3 ps, $SSPD_H$-APD_P: 365±7 ps, SSPDH-APDQ: 327±1 ps. In reality, the target X_t photons are delayed in fibre by ~55 ns, but since the origin of τ_2 is arbitrary we choose it to coincide with the maximum output fidelity for clarity of the presentation.

To evaluate the performance of our ELED we perform teleportation for six control photon polarisations distributed over the Poincare sphere as shown in figure 3.5, chosen to represent teleportation of a general qubit state. For each input, Bob's polarisation basis P-Q is set to the expected output basis, and we simultaneously record third-order correlation functions $g_{HVP}^{(3)}(\tau_1, \tau_2)$ and $g_{HVQ}^{(3)}(\tau_1, \tau_2)$. This allows us to evaluate the fidelity of the detected photons to the expected output state as

$$f_P(\tau_1, \tau_2) = \frac{g_{HVP}^{(3)}(\tau_1, \tau_2)}{g_{HVP}^{(3)}(\tau_1, \tau_2) + g_{HVQ}^{(3)}(\tau_1, \tau_2)} \tag{3.2}$$

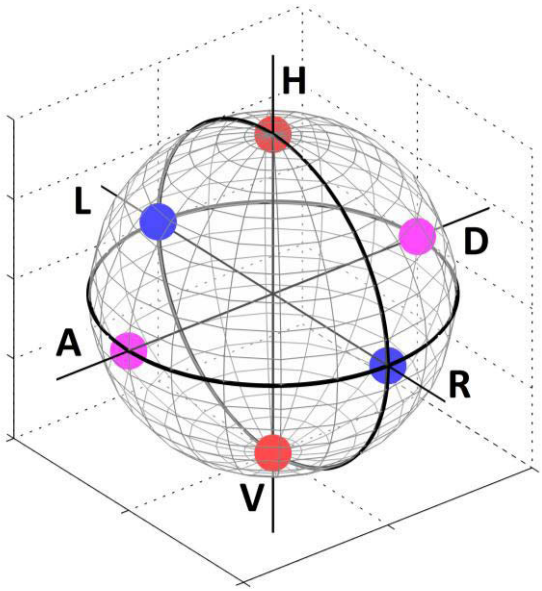

Figure 3.5:Poincaré sphere with the six input states used in the teleportation experiment.

3.2.2 Properties of the entangled light-emitting diode

The ELED was operated at 93 nA/μm^2 d.c. current in a liquid helium cooled cryostat at ~15K. The quantum dot spectrum, shown in figure 3.6(a) is dominated by the X and XX photons and we verify the fine-structure splitting of the X state to be 2.0±0.2 μeV (see section 2.2.1.1). For successful teleportation the source must provide photons of high quality; teleportation relies on two-photon interference on BS2, which requires long photon coherence times, and accidental multiple photons can cause false detections lowering the overall teleportation fidelity. At the chosen operating conditions the XX coherence time is measured to be 161±4 ps, and we verify the sub-Poissonian emission character using a Hanbury-Brown-Twiss interferometer, with resulting second-order correlation functions $g^{(2)}(\tau)$ shown in figure 3.6(b) for the X and XX photons respectively. The measurements reveal an almost perfect anti-bunched behaviour, with the minimum values (X: 0.096±0.010, XX: 0.105±0.008) being explainable with the finite time response of the detectors used. In contrast, photons from parametric down-conversion sources conventionally used in teleportation experiments[14,115,118] have a $g^{(2)}(0)\sim1$. Accidental errors from multiple pairs are one of the main limiting factors in multi-photon experiments[53] and limits the scalability of SPDC-based quantum information schemes.

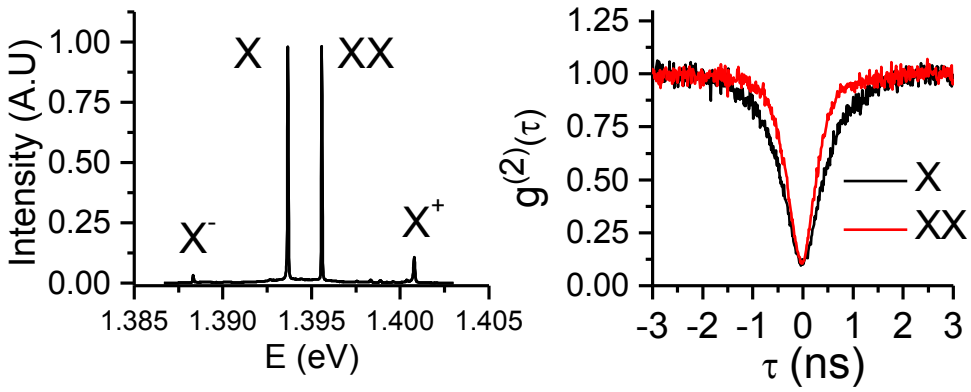

Figure 3.6: (a) Electroluminescence spectrum from the identified quantum dot, operated at 93 nA/μm² and ~15K. (b) Second-order correlation functions of the X and XX transitions measured using a Hanbury-Brown-Twiss interferometer.

We investigate the entanglement properties of the XX-X photon pairs emitted by the ELED at the chosen operating conditions in the same way as described in section 2.2.1. Figure 3.7 shows the measured polarisation correlations as a function of XX-X detection time delay τ in the rectilinear basis (H-V, panel a), diagonal linear basis (D-A, panel b) and circular basis (R-L, panel c). To quantify the results we calculate the degree of correlation C in each basis (see equations 2.10-2.11), with results shown in figure 3.8(a). In agreement with what is commonly observed for this type of dot we find stronger correlations in the circular and rectilinear bases than in the diagonal basis. As discussed in chapter 2 this can be attributed to the FSS of the exciton state and nuclear polarisation fluctuations in the quantum dot. The degree of correlation (figure 3.8(a)), in these three polarisation bases allows us to calculate the fidelity to the ideal Bell state (figure 3.8(b)), with a maximum of 0.777±0.005, confidently above the classical limit of 0.5.

Figure 3.7: Polarisation correlations of d.c. electrically excited quantum dot ELED. XX-X correlations measured in (a) rectilinear basis H/V coinciding with the basis of the X eigenstates, (b) diagonal, linearly polarised superposition basis D/A, (c) circular polarisation basis R/L.

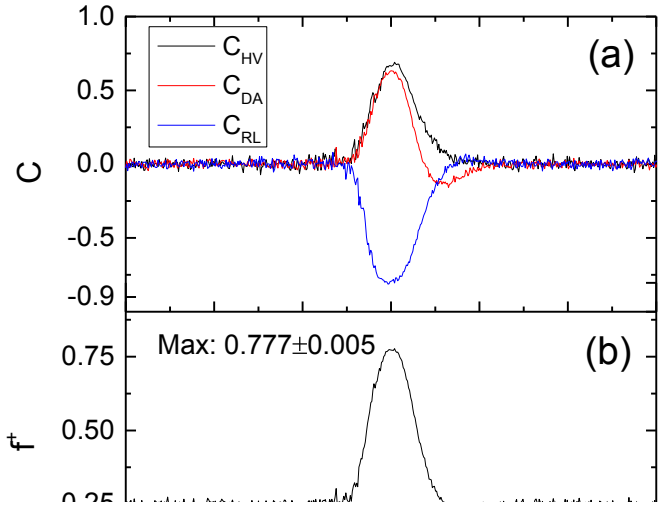

Figure 3.8: (a) Degree of correlation based on polarisation correlation measurements (figure 3.7). (b) Entanglement fidelity of the XX-X biphoton polarisation state used for teleportation.

3.2.3 Teleporting polar states

Of the six control photon states used to test the performance of our teleporter, the two polar states H and V, i.e. the input states that coincide with Alice's measurement basis and the quantum dot exciton eigenbasis, can be considered to be a special case. They do not require interference between the ancilla and the control photons, and they can be "teleported" without entanglement. To see why, consider the setup in figure 3.4 again, but let the control photon (XX_c) polarisation be restricted to H and V (but random for these): for each of Alice's pair-detections she knows due to the polarisation-resolved detection that the ancilla and the control photon were of opposite polarisations. Furthermore, if the photon pair source is correlated but not entangled, i.e. the ancilla and target photons are emitted in a statistical mixture of $|H_a H_t\rangle$ and $|V_a V_t\rangle$, she can be certain that if the control was V, the target must have been H, and if the control was H, the target must have been V. In other words, when Alice signals a coincidence Bob only has to apply a polarisation rotation of 90 degrees and can be certain to receive the correct state.

Figure 3.9 shows the experimentally acquired third-order correlations obtained for control state H when Bob detects V ($g^{(3)}_{HVV}(\tau_1, \tau_2)$, panel a) and H ($g^{(3)}_{HVH}(\tau_1, \tau_2)$, panel b) respectively. Many features originating from the quantum light source characteristics are visible: the vertical dip visible at $\tau_1 = 0$ originates from the suppressed probability of having two XX photons emitted simultaneously and passing down the same arm of the interferometer. Similarly, the vertical dark stripe at $\tau_1 = -2.5$ ns corresponds to a suppression of two XX photons emitted at the same time with the photon detected by $SSPD_V$ having come down the short arm and the one detected by $SSPD_H$ having arrived through the long arm.

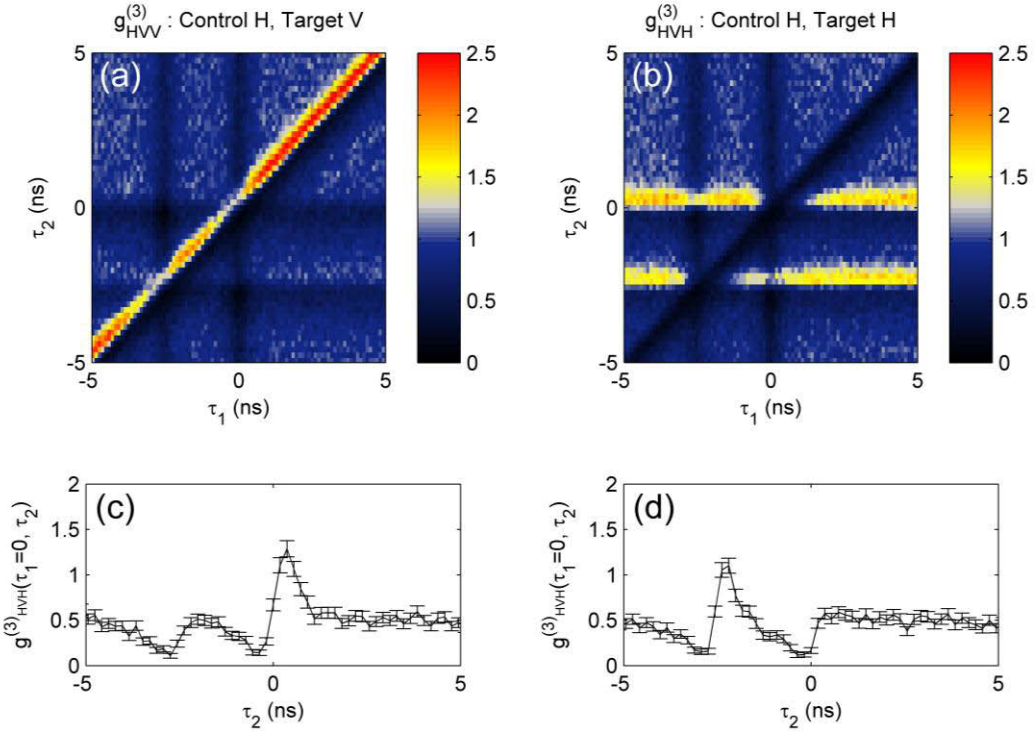

Figure 3.9: Third-order correlation functions for control H and (a) Bob measuring V, (b) Bob measuring H. One-dimensional cut through third-order correlation for (c) Bob measuring V and (d) Bob measuring H.

The horisontal dark stripes at $\tau_2 = 0$ in figure 3.9(a) and the horisontal bright stripes at $\tau_2 = 0$ in figure 3.9(b) can be explained by the polarisation correlations between XX_a and X_t photons: Since τ_2 measures the detection time difference between the target X_t photon and $SSPD_H$, X_t photons detected at $\tau_2 = 0$ "belong" to the XX_a photon measured to have polarisation H. Consequently, for target V (figure 3.9(a)) we get a suppression and for target H (figure 3.9(b)) we get an increase, consistent with polarisation correlations showing a high degree of XX-X co-polarisation in the rectilinear basis (see figure 3.7(a) in the previous section). Similarly the horisontal stripes at $\tau_2 = -2.5$ ns originate from correlations between the control photon and the target photon, and can be considered artefacts that have no impact on the teleporter performance and can thus be safely ignored.

On the diagonal in figures 3.9(a) and (b) we have $\tau_2 = \tau_1$, i.e. the target photon is detected simultaneously with the photon detected by $SSPD_V$. Hence, the polarisations are correlated but reversed compared to the horisontal stripes, i.e. target H is suppressed (dark stripe, panel b) while target V is enhanced (bright stripe, panel a).

Quantum teleportation of a general state only succeeds when Alice detects a coincidence, i.e. $\tau_1 = 0$. The lower panels in figure 3.9 show cross-sections through the third-order correlation functions for Bob detecting V ($g^{(3)}_{HVV}(\tau_1 = 0, \tau_2)$ in panel c) and H ($g^{(3)}_{HVH}(\tau_1 = 0, \tau_2)$ in panel d) respectively. Only when the target photon is correlated with the ancilla, i.e near $\tau_2 = 0$, can general teleportation succeed. Comparing the two traces in this region we clearly see that Bob receives mainly V photons as expected from the three-photon state in equation 3.1 in the beginning of this chapter.

Figure 3.10 shows the fidelity $f_{H\to V}(\tau_1, \tau_2)$ of the detected photons to the expected target state V as a function of Alice's (τ_1) and Bob's (τ_2) detection times in panel b. In most parts of the figure the fidelity is close to 1/2, i.e. the target photon polarisation is completely random. But a clear diagonal stripe with higher fidelity runs all the way through the two-dimensional plot. This expresses what was qualitatively discussed above: two-photon interference is not required for the polar states, so the fidelity can be above 1/2 even where $\tau_1 \neq 0$. As we shall see in the next section, teleportation of arbitrary states is only successful when $\tau_1 \approx 0$, so for a general teleporter this is the region of interest. Figure 3.10(a) and (c) show cross-sections through the two-dimensional fidelity map for $\tau_1 = 0$ and $\tau_2 = 0$ respectively with a peak fidelity of 0.802 ± 0.035.

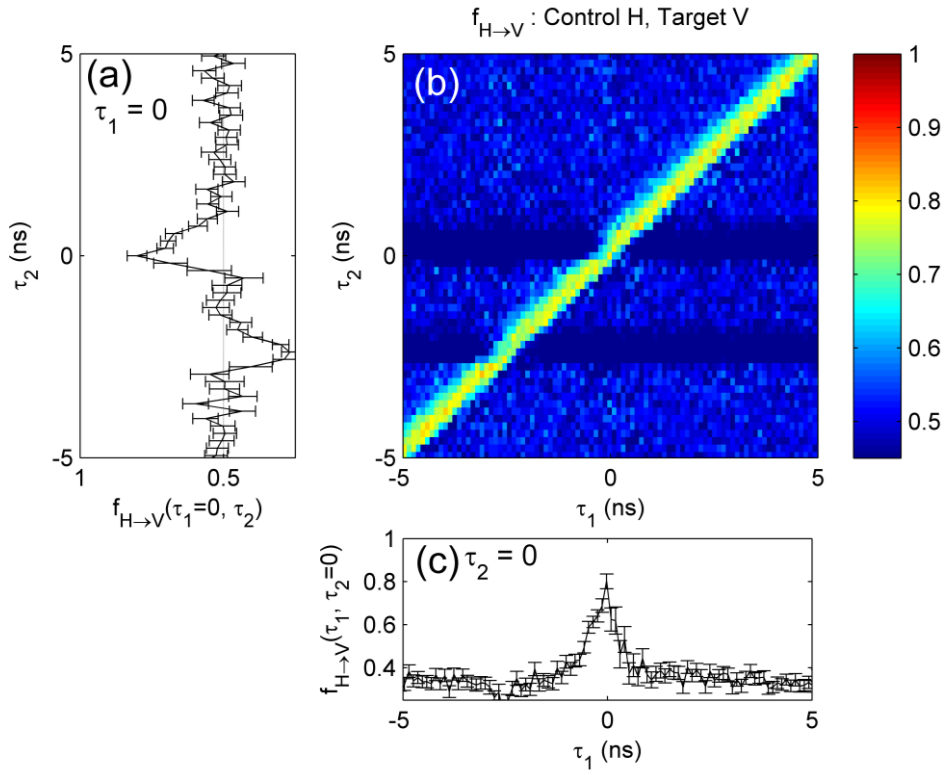

Figure 3.10: (a) Fidelity $f_{H\to V}$ as a function of $\tau_2$when Alice registers coincidences ($\tau_1 = 0$). (b) Fidelity as a function of Alice's detection time (τ_1) and Bob's detection time (τ_2). At $\tau_1 = \tau_2 = 0$ we find fidelity 0.802±0. (c) Fidelity as a function of Alice's detection time only, when $\tau_2 = 0$.

The teleporter was evaluated also for the second polar state V, with resulting $g^{(3)}_{HVV}(\tau_1, \tau_2)$ and $g^{(3)}_{HVH}(\tau_1, \tau_2)$ shown in figure 3.11 (a) and (b) respectively. Similar to what was observed for H input, we find a central vertical dip extending through the plots, owing to the sub-Poissonian nature of the XX emission. Likewise a second dark vertical stripe is visible, this time at $\tau_1 = +2.5$ ns instead of negative times, since now it is $SSPD_H$ instead of $SSPD_V$ that is "blind" to the control state preparation arm of the setup. For the same reason only one horizontal feature is visible, whereas two diagonal stripes are visible. The horizontal stripes extending through the whole figure, showing suppression for target V (panel a) and enhanced detection for target H (panel b), shows also for this polar input state that interference is not needed. Polarisation correlations are needed though, although classically correlated photons in the H-V basis would suffice. Figure 3.11(c) and (d) show cross-sections through the $g^{(3)}(\tau_1, \tau_2)$ functions for $\tau_1 = 0$, highlighting the fact that for control V, Bob measures predominantly H when $\tau_2 \sim 0$. Just as for input H we quantify how well the teleportation process works by calculating the fidelity $f_{V\to H}(\tau_1, \tau_2)$ according to equation 3.2. The resulting two-dimensional map is shown in figure 3.12(b), with cross-sections through the origin shown in panels (a) and (c). A streak of high fidelity runs horizontally along τ_1 at $\tau_2 = 0$ as expected from the measured third-order correlations, and we find fidelity 0.833±0.027 at the origin. The fidelity remains ~1/2 for most other times. The relatively strong, positive diagonal trace offset by -2.5 ns is due to correlations between control and target photons but, it must be stressed again, has no impact on the teleportation of general input states, for which we will focus on the origin only.

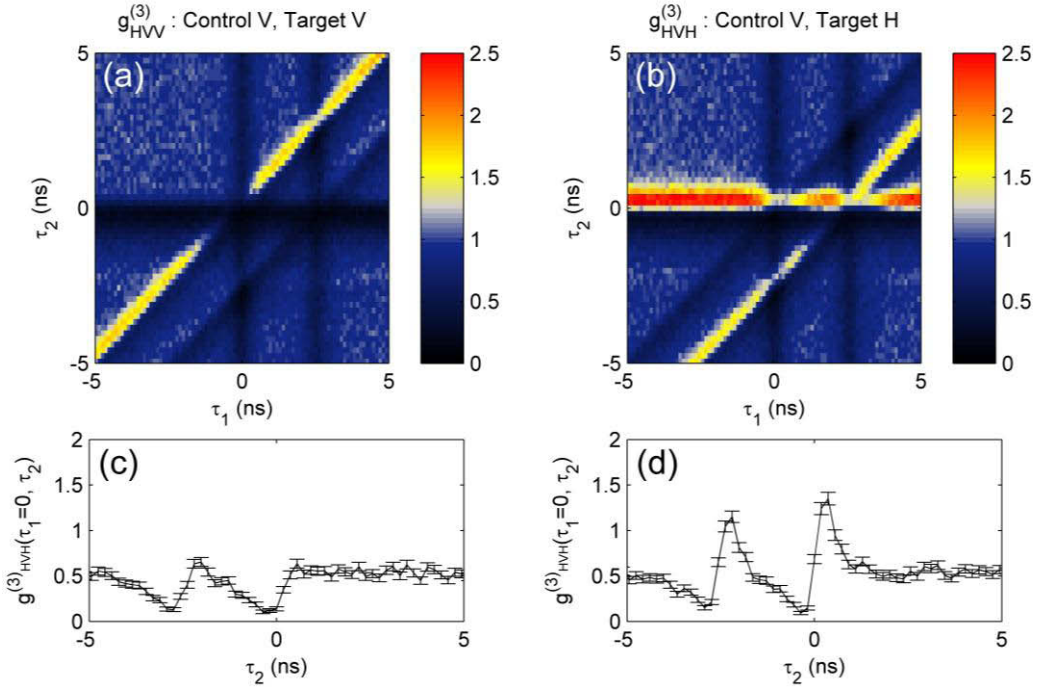

Figure 3.11: Third-order correlation functions for control V and (a) Bob measuring V, (b) Bob measuring H. One-dimensional cut through third-order correlation for (c) Bob measuring V and (d) Bob measuring H.

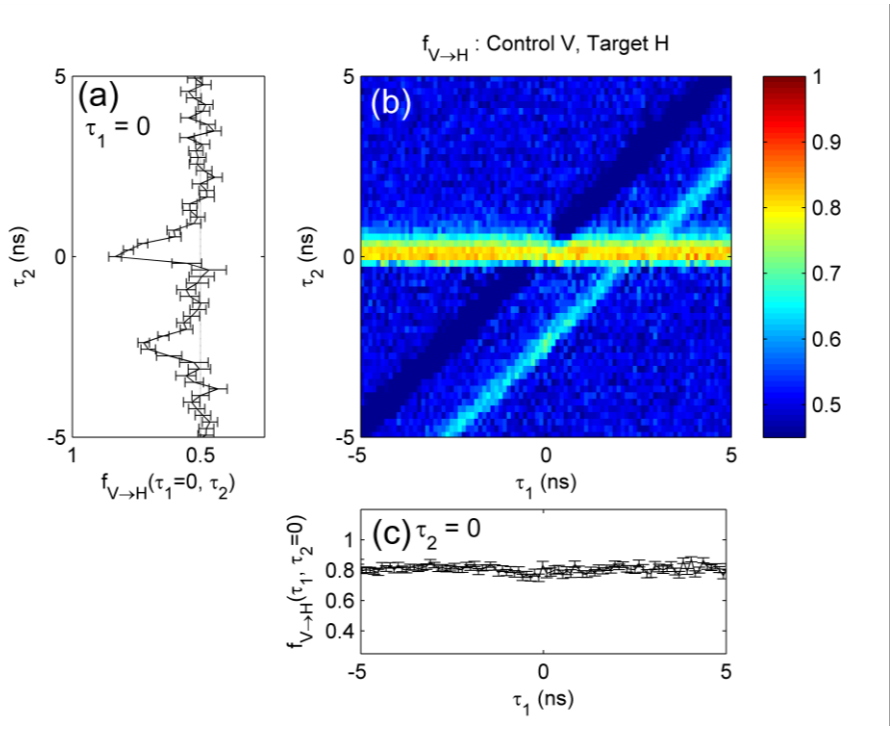

Figure 3.12: (a) Fidelity $f_{V\to H}$ as a function of τ_2 when Alice registers coincidences ($\tau_1 = 0$). (b) Fidelity as a function of Alice's detection time (τ_1) and Bob's detection time (τ_2). At $\tau_1 = \tau_2 = 0$ we find fidelity 0.833±0.027. (c) Fidelity as a function of Alice's detection time only, when $\tau_2 = 0$.

3.2.4 Teleporting superposition states

The results in the previous section, for teleportation of control states coinciding with Alice's measurement basis and the X eigenbasis, represent two special cases as already pointed out above, since they do not require interference and also no entanglement between XX-X pairs (but at least classical correlations). To fully characterise quantum teleportation with the entangled-light-emitting diode four more states were teleported, corresponding to the maximal superposition states located on the equator of the Poincaré sphere (figure 3.5); diagonal/anti-diagonal in the linear diagonally polarised basis ($|D_c/A_c\rangle = (|H_c\rangle \pm |V_c\rangle)/\sqrt{2}$) and right- and left circularly polarised ($|R_c/L_c\rangle = (|H_c\rangle \pm i|V_c\rangle)/\sqrt{2}$). These states, in contrast to H/V, require both quantum interference and entanglement and are therefore more challenging.

Figure 3.13(a) and (b) show the measured third-order correlation functions $g^{(3)}_{HVA}(\tau_1, \tau_2)$ and $g^{(3)}_{HVD}(\tau_1, \tau_2)$ respectively, for control photon state A. As for the polar states, the vertical dark streak extending through the figures at $\tau_1 = 0$ is due to suppressed probability of having two XX photons emitted simultaneously and travelling down the same arm of the fibre setup, owing to the excellent sub-Poissonian behaviour demonstrated previously in figure 3.6. This time two adjacent dark streaks at $\tau_1 = \pm 2.5$ ns can be seen, coming from suppression of two photons emitted simultaneously into different arms of the teleporter. Horizontal lines at $\tau_2 = 0$ originate from correlations between ancilla XX_a and target X_t photons, when the XX photon is detected by Alice's detector $SSPD_H$, the "time reference" detector. Similarly, diagonal features through the origin are due to XX_a-X_t correlations when the XX photon goes to Alice's $SSPD_V$. The horizontal and diagonal features going through the origin are of similar magnitudes in figure 3.13(a) and (b), as an A or D photon detected by Bob has approximately the same probability to be correlated with a H or V photon detected by Alice. Streaks offset by -2.5 ns can be safely ignored as they bear no influence on the teleportation, originating as they do from correlations between control and target photons, and can be considered an artefact of using the ELED also for control photon generation.

At the origin, when $\tau_1 = \tau_2 = 0$, one can not discern which of the two photons detected by Alice (the one detected by $SSPD_H$ or by $SSPD_V$) Bob's target photon is correlated to. This is where interference between the two XX photons can take place, and Alice's measurement effectively performs the Bell-state projection. The effect is visible upon comparison of the origin of figures 3.13(a) and (b), with the diagonal streak extending through the origin only in panel (b) when Bob detects D. The width in τ_1-direction of the area of interest is narrow, which is expected since quantum interference between ancilla XX_a and control XX_c can only occur within the XX coherence time of 161 ps. Figure 3.13(c) and (d), showing cross-sections through the $g^{(3)}$:s for coincident detection by Alice ($\tau_1 = 0$) also highlights that Bob predominantly receives D polarised photons when $\tau_2 \sim 0$. This signifies teleportation of the superposition state A onto D, as expected from the three-photon state in equation 3.1 in section 3.1.1.

Figure 3.14(b) shows the fidelity of the detected target photons onto D as a function of the detection times, $f_{A\to D}(\tau_1, \tau_2)$. At the origin a bright spot is visible, standing out with a peak fidelity of 0.718±0.026 against the background of ~1/2 surrounding it. The cross-sections, plotted in figure 3.14(a) as a function of Bob's detection time τ_2, and in 3.14(c) as a function of Alice's detection time τ_1, show peaks limited by the XX-X polarisation correlations in τ_2 and the XX coherence time in τ_1.

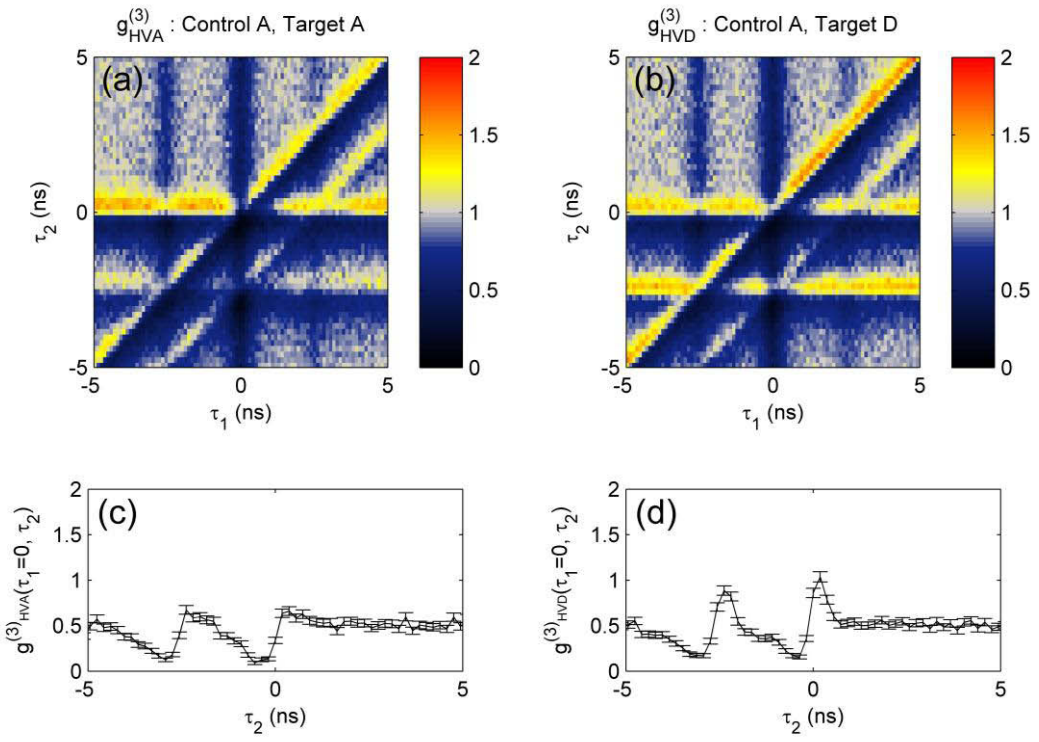

Figure 3.13: Third-order correlation functions for control A and (a) Bob measuring A, (b) Bob measuring D. One-dimensional cut through third-order correlation for (c) Bob measuring A and (d) Bob measuring D.

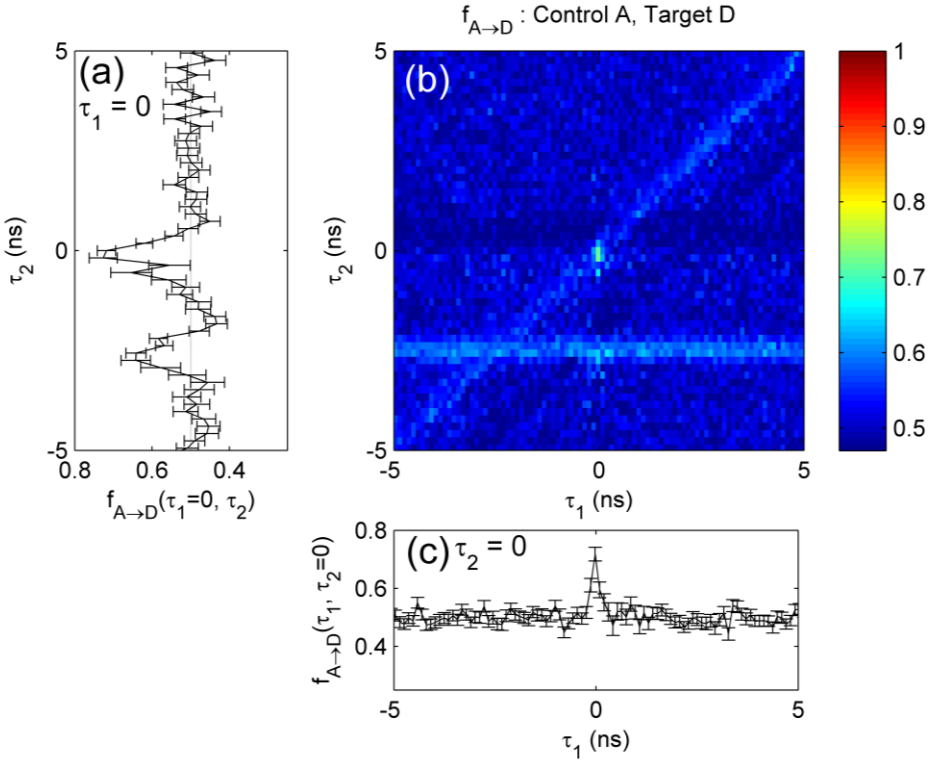

Figure 3.14: (a) Fidelity $f_{A\to D}$ as a function of τ_2 when Alice registers coincidences ($\tau_1 = 0$). (b) Fidelity as a function of Alice's detection time (τ_1) and Bob's detection time (τ_2). At $\tau_1 = \tau_2 = 0$ we find fidelity 0.718±0.026. (c) Fidelity as a function of Alice's detection time only, when $\tau_2 = 0$.

Teleportation of control qubits in the circular basis (R, L) qualitatively speaking appear very similar to results in the diagonal superposition basis (D, A). Figures 3.15(a) and (b) show the measured correlation functions $g^{(3)}_{HVL}(\tau_1, \tau_2)$ and $g^{(3)}_{HVR}(\tau_1, \tau_2)$ respectively, together with associated cross-sections along $\tau_1 = 0$ (panels c, d). The main difference here compared to the diagonal and polar states is that the output state is the same as the control state, i.e. L teleports to L, as is expected from equation 3.1. That Bob mainly receives L polarised photons when the teleportation succeeds is manifested in figure 3.15(a) in which the diagonal and horisontal stripes extend through the origin, and in figure 3.15(b) as a notable absence of detections at the origin. The same effect is illustrated in figure 3.15(c) and (d), plotting cross-sections through the origin along "Bob's time axis" τ_2. The fidelity $f_{L\to L}$ is shown in figure 3.16. Similar to A input (figure 3.14) successful teleportation occurs only for three-fold coincidence ($\tau_1 \approx \tau_2 \approx 0$), here with a fidelity of 0.646±0.035.

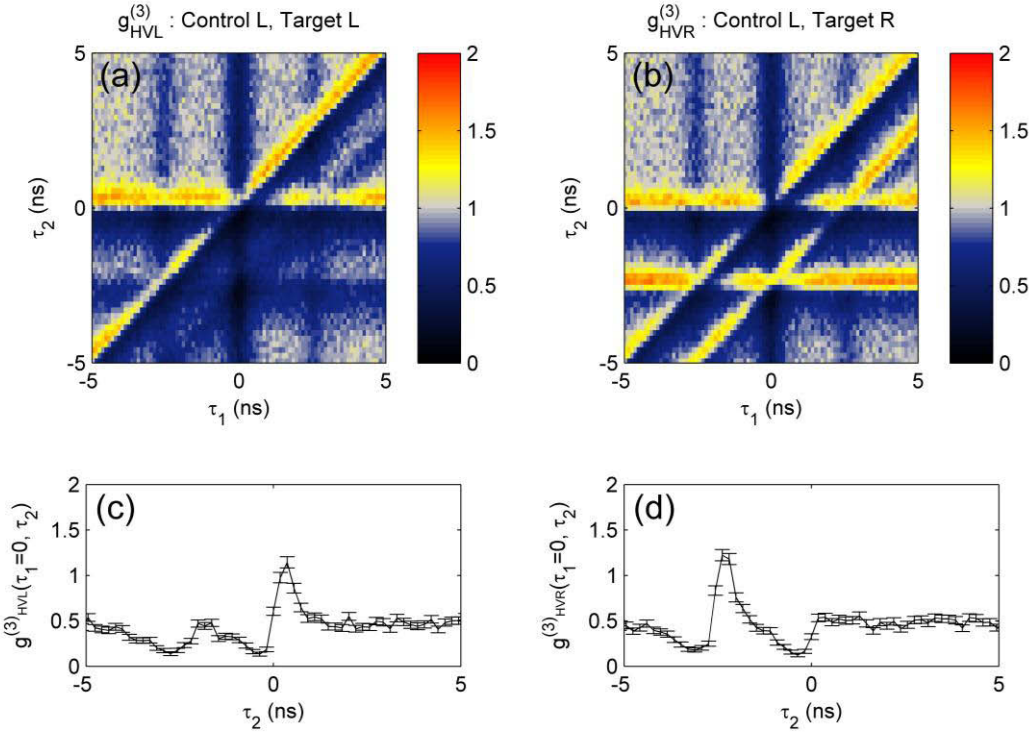

Figure 3.15: Third-order correlation functions for control L and (a) Bob measuring L, (b) Bob measuring R. One-dimensional cut through third-order correlation for (c) Bob measuring L and (d) Bob measuring R.

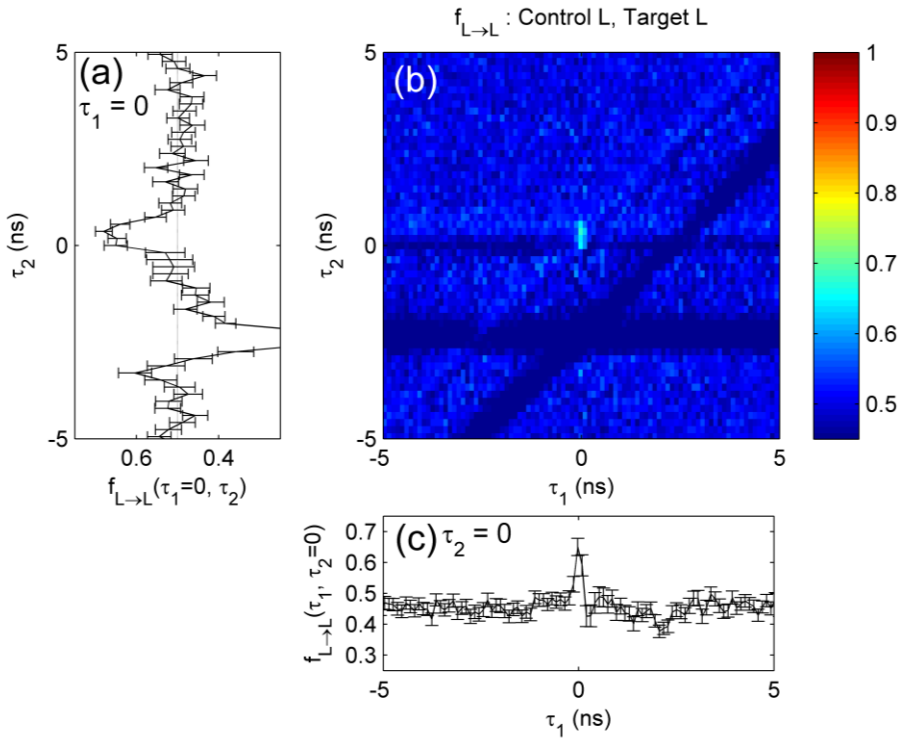

Figure 3.16: (a) Fidelity $f_{L\to L}$ as a function of $\tau_2$when Alice registers coincidences ($\tau_1 = 0$). (b) Fidelity as a function of Alice's detection time (τ_1) and Bob's detection time (τ_2). At $\tau_1 = \tau_2 = 0$ we find fidelity 0.646±0.035. (c) Fidelity as a function of Alice's detection time only, when $\tau_2 = 0$.

3.2.5 General teleportation and classical limit

Teleportation was performed for in total six states evenly distributed over the Poincaré sphere, with two polar states and four superposition states on the equator. The individual measured fidelities were 0.802±0.035, 0.833±0.027, 0.574±0.035, 0.718±0.026, 0.646±0.035 and 0.650±0.032 for control qubit states H, V, D, A, R and L respectively. We have already noted that the polar states H and V do not require entanglement or interference, and this explains the higher measured fidelity for these states. We can also note that all states have a fidelity significantly above 1/2, the limit for no information transfer (completely random measurement outcomes for Bob). The fidelities in the circular basis are equal within experimental error, but in the diagonal basis D has significantly lower fidelity than A. We attribute this asymmetry to weakly polarising elements in the setup that cause slight misalignments of the calibrated polarisations. This can also be seen in figure 3.14(b), where a weak diagonal streak is visible. However, simulations show that the effect on mutually orthogonal states (such as D and A) largely cancels out (modelled by K.H.A. Chan for ref. [132]). Indeed we can see that the average fidelity for D-A is 0.646±0.022, very similar to the average in the circular basis which is 0.648±0.024.

In the context of quantum teleportation of general qubit states, discussing individual states is not very meaningful. For example, if the control photons are restricted to one orthogonal basis, faithful "teleportation" with perfect fidelity is achievably if Alice just aligns her detection apparatus to this basis and shares classically correlated photons with Bob. Such a scheme requires neither interfering particles nor non-classical correlations. With a theoretical analysis it can be shown that for a classical teleporter equipped with the best possible general measurement device (positive operator-valued measurement, POVM device), the best achievable average fidelity is 2/3 for the six states considered here (proof by Marco Lucamarini, see supplementary information of ref. [132]). This result can also be understood intuitively; if Alice can achieve unit fidelity for the polar states on the Poincaré sphere by sharing only classically correlated photons, the outcome will be completely randomised for the diagonal and circular superposition states. The average fidelity is thus $(2 \cdot 1 + 4 \cdot 1/2)/6 = 2/3$. Note that if the tested input states are restricted to only four states the classical upper bound must be adjusted accordingly to $3/4$[134].

To prove non-classical behaviour the appropriate thing for the experiment here is thus to consider the average fidelity for our six control photon input states, which is shown in figure 3.17(a) below as a function of τ_1 and τ_2. A single high fidelity spot around $\tau_1 \approx \tau_2 \approx 0$ is visible, with a peak value of 0.704±0.016 which represents teleportation of general qubit states for three-fold coincidence. This fidelity beats the classical limit of 2/3 by 2.2 standard deviations and proves that quantum teleportation is taking place. The quoted error includes the Poissonian counting statistics (1.2%), uncertainty due to calibration of the time measurement apparatus (0.5%) and error due to polarisation misalignments (less than 1%). Figure 3.17(c) shows a cross-section at $\tau_2 = 0$, and similar to the individual superposition state fidelities the peak is narrow in τ_1 direction, limited by the imperfect quantum interference between ancilla and control photons determined by the XX photon coherence time. A simulated average fidelity is also shown (red lines), with a predicted fidelity of 0.712 and good general agreement with experimentally observed peak shapes. The model upon which these calculations are based was further developed for dissimilar input photons as described in detail in section 4.3.2.

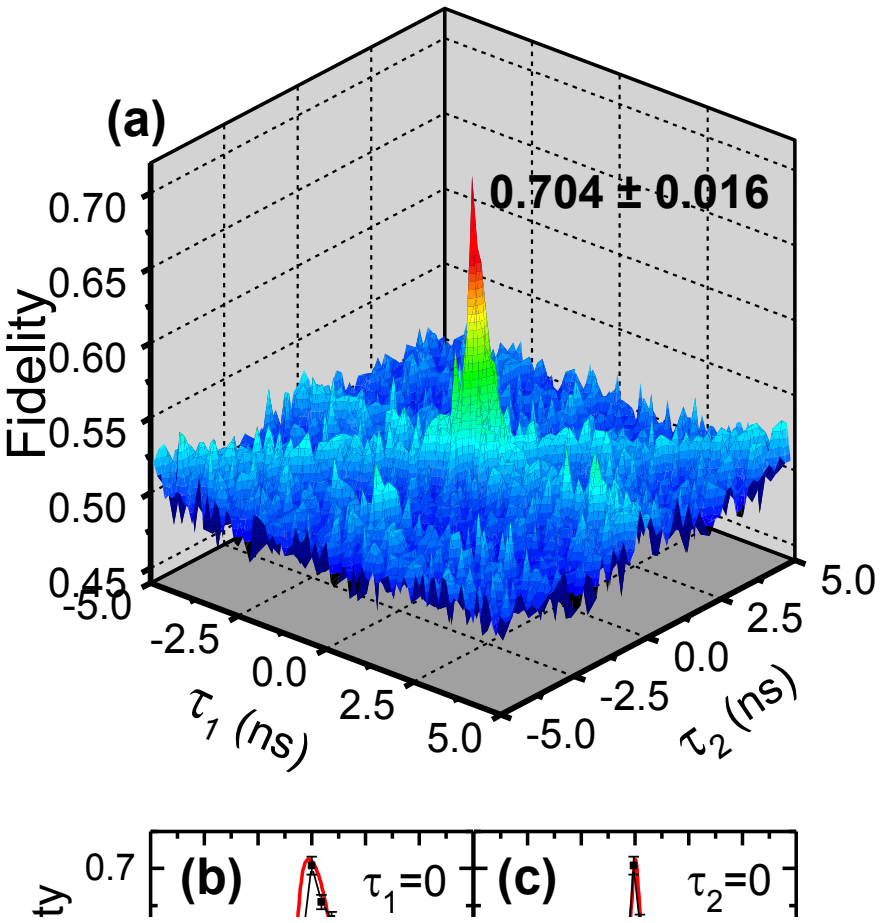

Figure 3.17: (a) Average fidelity for states H,V,D,A,R and L, as a function of Alice's (τ_1) and Bob's detection time (τ_2). When Alice registers a coincidence ($\tau_1 = 0$) and Bob simultaneously registers a detection ($\tau_2 = 0$), the average fidelity is 0.704±0.016 beating the classical limit of 2/3. (b) Cross-section through the two-dimensional fidelity map taken at $\tau_1 = 0$ (c) Cross-section through the two-dimensional fidelity map taken through $\tau_2 = 0$. Solid red curves in (b) and (c) is the modelled average fidelity (courtesy of K.H.A. Chan).

3.3 Conclusions

The results represents in this chapter represent the first realisation of a quantum teleporter based on electrically generated light from a quantum dot emitter. Teleportation was evaluated for six input polarisations, representing teleportation of a general qubit state, and was found to beat the classically achievable average fidelity. The fidelities of the individual states were asymmetrically distributed with the polar states H and V the highest since they do not require two-photon interference in Alice's beamsplitter. As they only rely on polarisation correlations they are mainly limited by the entanglement fidelity and the time coincidence window in τ_2 (183 ps). It was also found that the diagonal basis had elevated fidelity for A, and suppressed fidelity of D, while R and L had roughly the same fidelities. This is a side-effect attributed to weakly polarising elements such as the spectral filter and couplers in the fibre setup, but does not affect the average quantum teleportation fidelity appreciably (less than 1%).

Teleportation of superposition states requires successful quantum interference between ancilla XX_a and control XX_c. This is limited by the time resolution of Alice's detectors (103 ps) relative to the XX coherence time (161 ps), and the width post-selected time window (110 ps). Further improvements can be achieved with faster detectors, or – which will most likely be required for quantum information applications – developing entangled light sources with longer coherence times and/or shorter radiative lifetimes, approaching transform limited photons[32]. Shorter lifetimes can be achieved with Purcell enhancement by placing the dot in an optical cavity, which will also have the advantage of reducing the detrimental effect of exciton fine-structure on the entanglement fidelity[34]. With further improvements such as these the device could become a useful component in quantum information applications.

Although the fibre setup used in the experiments presented here prepared the input photons to be teleported using light from the same device as the entangled photons, it is in principle compatible with independent sources. In the next chapter we shall see how the setup was modified to accommodate an independent source of vastly different character and perform quantum teleportation of laser generated photons using the entangled-light-emitting diode.

4 Teleporting weak coherent states using a quantum entangled light source

4.1 Introduction

Quantum computing promises great power for solving certain problems in engineering and science[135,136]. With the research efforts still not close to the realisation of a useful quantum computer it is not clear what architecture will eventually be successful[137]. Intense work on different systems such as trapped as ions[138], NV-centres in diamond[139], semiconductor quantum dots[140] or atomic spins in silicon[141,142] are on-going. For long distance quantum *communication* on the other hand optical communication seems to be the by far most likely contender, as fibre optics already today forms the backbone of our long-distance communication infrastructure and photonic qubits are relatively robust to decoherence. Interfacing photonic qubits from a communication network with the above mentioned matter systems will require quantum teleportation protocols to transfer the information, and matter-light teleportation has for some of these systems been demonstrated[143,144]. Linear optics remains another attractive architecture to implement quantum logic[83,128,145], and similarly it would require all-optical teleportation[53,84,129]. It is conceivable that the input photon then is likely to originate from a dissimilar source to that supplying the entangled resource states. The most common source used by classical and quantum optical communication systems is the laser, but surprising as it may seem linear optics teleportation of an independent laser input has never been performed (it should however be noted that it has been done with non-linear optics based Bell-state measurement device, operating with extremely low success probability owing to the weak non-linear processes[118]). In fact, every demonstration so far of teleportation using linear optics use the same[14,134] or identical[121,146] sources for the input and entangled photons, often accompanied by a fourth heralding photon[146], making them impractical for general quantum networking.

In this chapter we build upon the work of the previous chapter and demonstrate optical teleportation of photons directly generated by a laser, mediated by a polarisation-entangled photon pair electrically generated by the entangled-light-emitting diode (ELED)[59]. The light sources differ considerably in character; in bandwidth by a factor ~100, and while the photon statistics of the laser is Poissonian the ELED produces characteristically sub-Poissonian light. This is a step towards practical applications such as extending the range of existing QKD systems (typically based on weak coherent laser pulses) using quantum relays [120] and repeaters [102]. Furthermore, the ELED offers practical advantages of electrical control, and as we show it erases the multi-photon character of the laser input field, thus eliminating errors if used in a quantum optics circuit.

As described in the previous chapter, linear optics quantum teleportation requires Hong-Ou-Mandel (HOM) type interference[32,87], usually realised using a 50:50 beamsplitter, between the input qubit and one ancilla photon from an entangled photon pair[13,14]. Here, we interfere our photons on a strongly unbalanced (95:5) beamsplitter to achieve quantum teleportation of the polarisation state carried by input photons from a CW laser. The large coupling imbalance allows us to make efficient use of the photons produced by the quantum dot emitter.

All experiments in this chapter are carried out using the same electrical excitation conditions as in chapter 3, i.e. at ~15 K and with a d.c. current of ~90 nA/μm^2, under which conditions the XX coherence time is 161 ± 4 ps, corresponding to a linewidth of $2\hbar/\tau_c \sim 8\ \mu eV$. In comparison the laser has a linewidth of ~50 neV.

To verify that interference does take place on the somewhat unusual unbalanced coupler, we start this chapter by demonstrating quantum interference experiments with it (section 4.2). The experiments also allowed us to do direct observations of quantum beats between photons originating from the laser and the quantum dot, something that has previously only been done with extremely long photon wavepackets from atomic transitions[147,148].

After having verified that interference is indeed taking place the attention is turned to quantum teleportation experiments (section 4.3), including density matrix measurements (section 4.3.3.4) characterising the output state more carefully than what was done in chapter 3.

4.2 Quantum beats between dissimilar photons

4.2.1 Experimental setup

Before proceeding to the quantum teleportation experiments, we verify the two-photon interference of our dissimilar light sources on the unbalanced beamsplitter using the setup illustrated schematically in figure 4.1. The setup is implemented using single mode fibre components and single-photon counting detectors. XX photons from the ELED are selected using a transmission grating filter, then polarised and fed into input port 1 of the unbalanced 95:5 beamsplitter, which couples with 95% efficiency to output mode 3. The CW laser is also polarised and then fed to input port 2 with coupling 5% to port 3. Mode 4 goes to a spectrometer and allows us to monitor and computer control the emission wavelength of the laser, and thus the detuning ΔE of the laser and ELED, which is estimated to be controlled with a precision of ~5 μeV. Using a balanced beamsplitter (50:50) at port 3 we measure second-order correlations using detectors D1 and D2 for co-polarised (interfering) and cross-polarised (non-interfering) inputs. With computer controlled fibre-based polarisation controllers the polarisations of the sources is switched between co- and cross-polarised periodically during data acquisition.

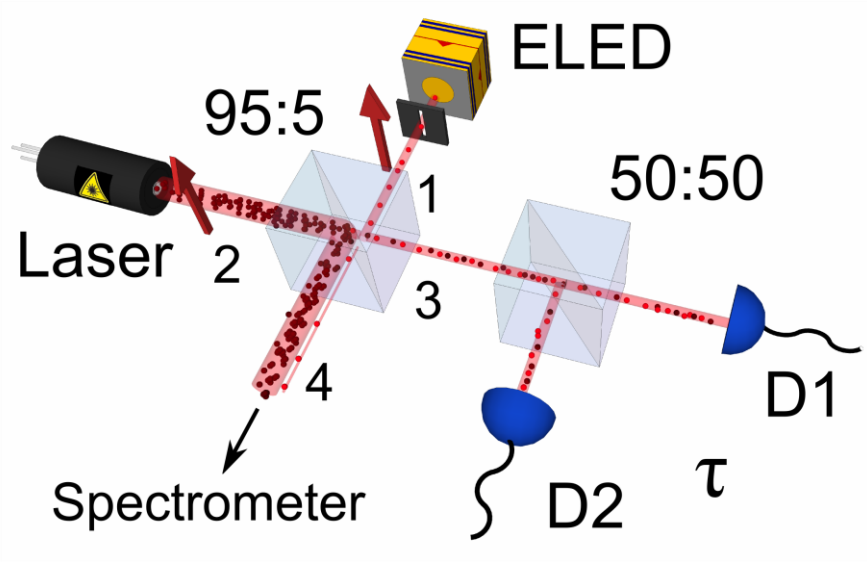

Figure 4.1: Schematic of fibre-based experimental setup for two-photon interference on a 95:5 beamsplitter between a laser photon and XX photons from an entangled-light-emitting diode (ELED). The ELED couples from port 1 to 3 with efficiency $cos^2\kappa = 0.95$ and the laser couples from 2 to 3 with probability $sin^2\kappa = 0.05$. The sources couple with reversed probability to output mode 4, which is sent to a spectrometer for monitoring of the sources' detuning ΔE. Bunching of photons in output 3, the signature of interference, is observed using a 50:50 beamsplitter and superconducting single-photon counting detectors D1 and D2.

4.2.2 Modelling two-photon interference of dissimilar sources

In order to arrive at a model for the two-photon interference experiments presented in this chapter we follow the model presented in chapter 2 closely, but do some modifications to account for the dissimilar photon sources and the unbalanced beamsplitter.

For the unbalanced beamsplitter in figure 4.1 the mode creation operators $\hat{a}_k^\dagger$ for the input ports (1,2) and output ports (3,4) can be related according to the convention[98]:

$$\begin{pmatrix} \hat{a}_3^\dagger \\ \hat{a}_4^\dagger \end{pmatrix} = \begin{pmatrix} \cos\kappa & \sin\kappa \\ -\sin\kappa & \cos\kappa \end{pmatrix} \begin{pmatrix} \hat{a}_1^\dagger \\ \hat{a}_2^\dagger \end{pmatrix} \tag{4.1}$$

which means that the coupling ratios are $\cos^2\kappa = 0.95$ from port 1 to 3 and $\sin^2\kappa = 0.05$ from port 2 to 3.

The photons emitted by the quantum dot are modelled as exponentially decaying wavepackets with random phase fluctuations due to decoherence processes (see sections 1.4.3 and 2.1.2), and furthermore they are considered to be fed to port 1 (see setup in figure 4.1):

$$\zeta_1(t) = \begin{cases} A\exp(-t/2\tau_r - i\omega_1 t - i\Phi(t)) \text{ ,t} \geq 0 \\ 0, \text{ else} \end{cases} \tag{4.2}$$

The laser, on the other hand, is a CW laser in port 2. Initially we consider the laser to have Gaussian wavepackets of width σ:

$$\xi_2(t) = Ae^{-(t-t_0)^2/2\sigma^2 - i\omega_2 t} \tag{4.3}$$

The laser employed in the experiments is a CW laser with coherence length much longer than the XX photons it is interfering with, so the approximation of a very wide Gaussian wavepacket ($\sigma \gg \tau_r$) can be justified. A variable time delay t_0 is included to model the random arrival time differences of the photons due to the d.c./CW nature of the experiment. The possible detuning of the sources is modelled by having different central frequencies of the two wavepackets, $\Delta E = \hbar(\omega_1 - \omega_2)$.

Let us call the creation operators of the output ports of the 50/50 splitter in figure 2.8 going to detector D1 $\hat{d}_1^\dagger$ and detector D2 $\hat{d}_2^\dagger$. These operators are easily related to the output port 3 of the unbalanced beamsplitter through $\hat{a}_3^\dagger = (\hat{d}_1^\dagger + \hat{d}_2^\dagger)/\sqrt{2}$. The probability to have detections by detector D1 at time t and D2 at time $t + \tau$, similar to eq. 2.5 in chapter 2, can be calculated with the electric field operators at detectors D1 ($\hat{E}_{D1}^{\pm}(t)$) and D2 ($\hat{E}_{D2}^{\pm}(t)$)[74]:

$$\begin{aligned} p(t, t+\tau, \Delta t) &= \langle 1_1 1_2 | \hat{E}_{D1}^-(t)\hat{E}_{D2}^-(t+\tau)\hat{E}_{D2}^+(t+\tau)\hat{E}_{D1}^+(t) | 1_1 1_2 \rangle = \\ &= \left| \langle 0 | \hat{E}_{D2}^+(t+\tau)\hat{E}_{D1}^+(t) | 1_1 1_2 \rangle \right|^2 \end{aligned} \tag{4.4}$$

Through the beamsplitter relations we can transform this to the electric field operators at input ports of the system (ports 1, 2 of the unbalanced splitter):

$$
\begin{aligned}
&p(t, t+\tau, \Delta t) = \\
&= \left| \langle 0 | \left(\frac{\cos\kappa}{\sqrt{2}} \hat{E}_1^+(t) + \frac{\sin\kappa}{\sqrt{2}} \hat{E}_2^+(t) \right) \cdot \left(\frac{\cos\kappa}{\sqrt{2}} \hat{E}_1^+(t+\tau) + \frac{\sin\kappa}{\sqrt{2}} \hat{E}_2^+(t+\tau) \right) |1_1 1_2\rangle \right|^2 \\
&= |\langle 0| \left(\frac{\cos^2\kappa}{2} \hat{E}_1^+(t) \hat{E}_1^+(t+\tau) + \frac{\cos\kappa \sin\kappa}{2} \hat{E}_1^+(t+\tau) E_2^+(t) + \right. \\
&\left. + \frac{\cos\kappa \sin\kappa}{2} \hat{E}_1^+(t) E_2^+(t+\tau) + \frac{\sin^2\kappa}{2} \hat{E}_2^+(t) \hat{E}_2^+(t+\tau) \right) |1_1 1_2\rangle|^2
\end{aligned}
\tag{4.5}
$$

When writing $|1_1 1_2\rangle$ we explicitly ignore the possibility of detecting two photons from one source, i.e. either in mode 1 from the quantum dot, or in mode 2 from the laser. This means we can drop the first and the last terms in the above expression. Then, by making the same assumption as in section 2.1.2, i.e. that the modes 1 and 2 are restricted to specific spatio-temporal mode functions defined in equations 4.2 and 4.3, we get:

$$
p(t, t+\tau, \Delta t) = \frac{\cos^2\kappa \cdot \sin^2\kappa}{4} \cdot |\zeta_1(t+\tau)\zeta_2(t) + \zeta_1(t)\zeta_2(t+\tau)|^2 \tag{4.6}
$$

Equation 4.6 above is very similar to what we had in eq. 2.7 of section 2.1.2, but has new pre-factors reflecting the fact that we are using an unbalanced beamsplitter and a 50:50 splitter on the output (mode 3) to observe the photon statistics. The interference factor differs in that the mode functions are reflecting dissimilar sources and also in that it has a positive sign owing to the detections being made in the same output arm of the interference beamsplitter (95:5).

Integrating over the detection times of D1 (t) and the arrival time of the laser photon (t_0), then letting the Gaussian wavepacket become infinitely long ($\sigma \to \infty$), we arrive at the detection probability we are interested in:

$$
P(\tau) = \frac{1}{4} \cos^2\kappa \sin^2\kappa \cdot (1 + \exp(-|\tau|/\tau_c) \cdot \cos \Delta E \tau/\hbar) \tag{4.7}
$$

where τ_c is the coherence time of the XX photons and ΔE is the XX to laser energy detuning. Compared to eq. 2.7 of section 2.1.2 equation 4.7 above has a sign change, reflecting the fact that we are observing the effect of interference in the same output arm of the beamsplitter (95:5) instead of opposite outputs, meaning that interference will manifest itself as bunching of photons. Also, an oscillating factor is present, indicating that we should be able to observe quantum beats if the sources have a non-zero detuning, provided that our detectors can resolve them.

In order to arrive at expression 4.7 we explicitly ignored the possibility of having multiple photons from either source, which is a simplified picture. By considering different cases that can lead to coincident detections at detectors D1 and D2 we can take these into account and estimate the second-order correlation function for co-polarised laser and ELED[82] as it will be measured in the experiment:

$$
g_{||}^{(2)}(\tau) = \frac{2\eta\alpha^2 \cdot \left(1 + e^{-|\tau|/\tau_c} \cdot \cos \Delta E \tau/\hbar\right) + \eta^2 g_{HBT}^{(2)}(\tau) + \alpha^4}{(\eta + \alpha^2)^2} \tag{4.8}
$$

where η is proportional to the XX photon intensity and α^2 is proportional to the laser intensity measured at detectors D1 and D2. The first term represents the wanted case with one photon from the quantum dot and one from the laser. The unbalanced coupling ratios $\cos^2\kappa$, $\sin^2\kappa$ have been "bundled" into the intensity factors η and α^2 (which are experimentally easily accessible from count rates on D1 and D2) and are therefore no longer explicitly written. The second term represents accidental coincidences from the quantum dot, where $g^{(2)}_{HBT}(\tau)$ is the XX transition second-order auto-correlation function, separately measured and analytically fitted as in chapter 2. The final term represents accidental coincidences from the laser. By convolving the above expression with the instrument response for detectors D1-D2 (measured to be 80 ps) we arrive at the simulated interference visibility presented together with the experimental results in the next section.

4.2.3 Experimental results

The measured second-order correlation functions $g_{||}^{(2)}(\tau)$ for co-polarised interfering photons are shown in figure 4.2 below for increasing detuning ΔE going from the bottom to the top of the figure. Points indicate experimental data and solid lines are simulated correlations according to equation 4.8 from the previous section. For zero detuning we show second-order correlations for both the interfering photons ($g_{||}^{(2)}(\tau)$, bottom correlation, black) and for non-interfering, orthogonally polarised photons ($g_{\perp}^{(2)}(\tau)$, bottom correlation, red). For non-interfering photons, which represent what is expected classically, we see a clear dip originating from the partially sub-Poissonian photon stream, while the co-polarised, interfering case contrasts with a clear peak. We note that this peak originates from our direct observation of the "bunching" behaviour due to bosonic coalescence in output port 3. Previous two-photon interference experiments usually observe two-photon interference as an *absence* of coincidences in opposite output ports[32,82,87].

As we increase the detuning ΔE quantum beats with increasing frequency appear in the correlations. The grey dashed line in figure 4.2 shows the calculated beat period for each detuning energy. Quantum beats of similar kind have previously been observed for photons originating from atomic transitions with very long radiative lifetimes (hundreds of nanoseconds)[147,148], but our observations here are to the best of our knowledge the first for quantum dot emitters.

It is interesting to note that the two-photon interference can be viewed as single-photon interference conditional on the detection of the first photon[74,147]: when the first photon is detected by either D1 or D2 the system is projected into the state $(|1_1 0_2\rangle \pm |0_1 1_2\rangle)/\sqrt{2}$, an entangled photon-number state for the input modes, since no which-way information exists revealing which input port the first (detected) photon originated from (the $\pm$ depends on which detector fired first). However, if the two photons are detuned the two components will evolve with different frequencies until the detection of the second photon, giving the detection time dependent state $|\psi_{12}(\tau)\rangle = (|1_1 0_2\rangle \pm \exp(\Delta E\tau/\hbar)|0_1 1_2\rangle)/\sqrt{2}$. The detection probability in output mode 3 can be calculated from this and acquires the characteristic beat $1/2 \cdot (1 + \cos \Delta E\tau/\hbar)$.

An effect of the quantum beats that will be of practical importance in our quantum teleportation experiments is the narrowing of the central peak of $g_{||}^{(2)}(\tau)$ with increasing ΔE. With the finite detector time resolution this means that the peak becomes harder and harder to resolve. This effect is visible in figure 4.2 as the detuning increases. To quantify the interference we calculate the interference visibility as $V(\tau) = \left(g_{||}^{(2)}(\tau) - g_{\perp}^{(2)}(\tau)\right)/g_{\perp}^{(2)}(\tau)$, and the resulting experimentally measured visibilities are shown in figure 4.3(a). We see that the visibility approaches zero for detection time differences larger than the XX photon coherence time $\tau_c \sim 161$ ps. The effect of detuning is also visible, both as oscillations of increasing frequency and as a reduced visibility at coincident detection ($\tau = 0$). The peak visibility $V(0)$ as a function of detuning ΔE is summarised in figure 4.3(b) together with simulation results. The magnitude of the observed bunching begins to drop as the beat period approaches the detector time resolution (80 ps for the pair D1-D2) but the interference is surprisingly robust, with appreciable visibility still after $\Delta E = 15$ μeV, and beats still visible in the correlations at $\Delta E = 40$ μeV, several times larger than the XX linewidth of $2\hbar/\tau_c \sim 8$ μeV. The somewhat surprising robustness of the post-selective two-photon interference shown here will be of practical help when performing the quantum teleportation experiments.

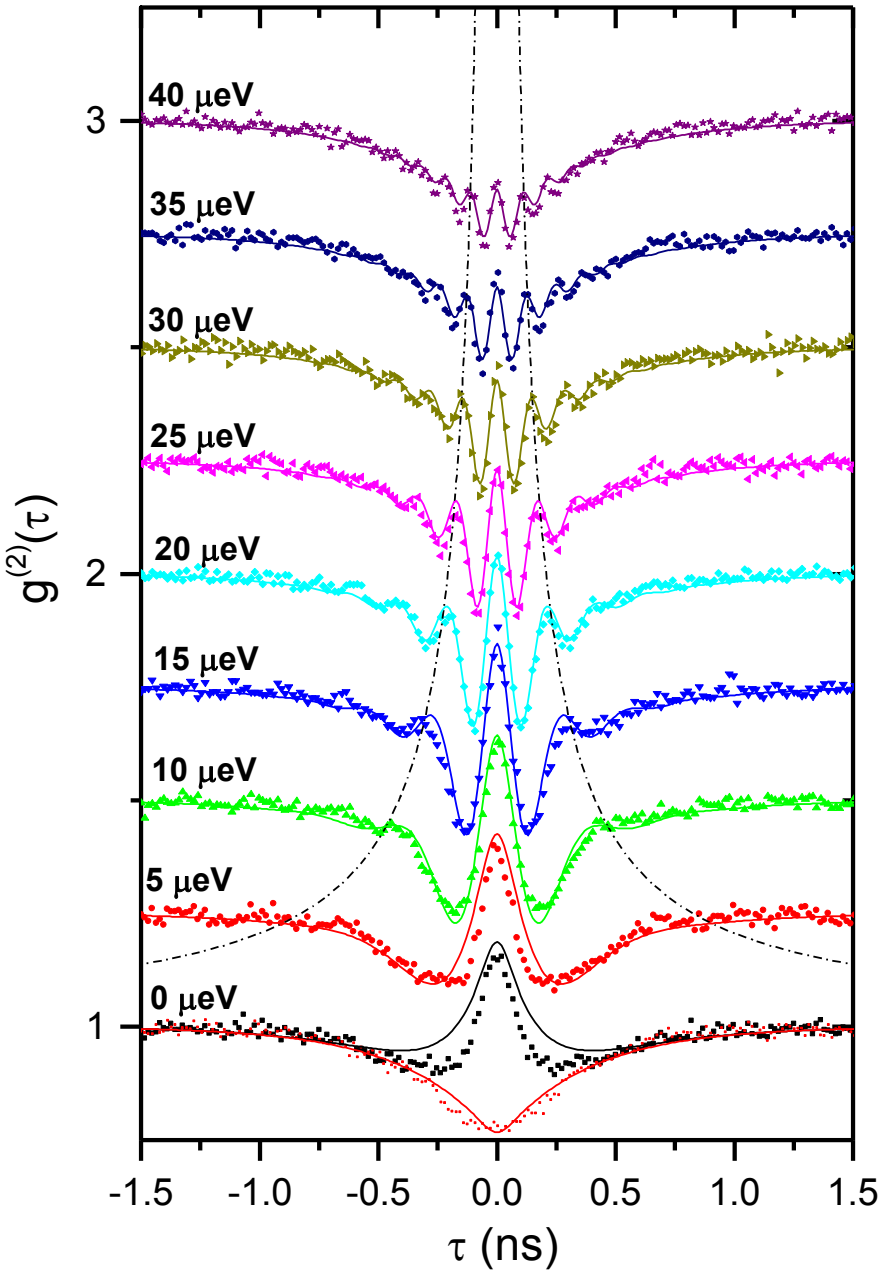

Figure 4.2: Measured (points) and simulated (full lines) second-order correlation functions for increasing energy detuning between co-polarised laser and ELED. For zero detuning (bottom correlations) the cross-polarised case is also shown (red curve). Clear evidence of bunching is manifested by the peak at $\tau \sim 0$ for co-polarised inputs (black curve, 0 μeV). For increasing detuning quantum beats appear, with period closely matching the expected value (grey, dashed curve).

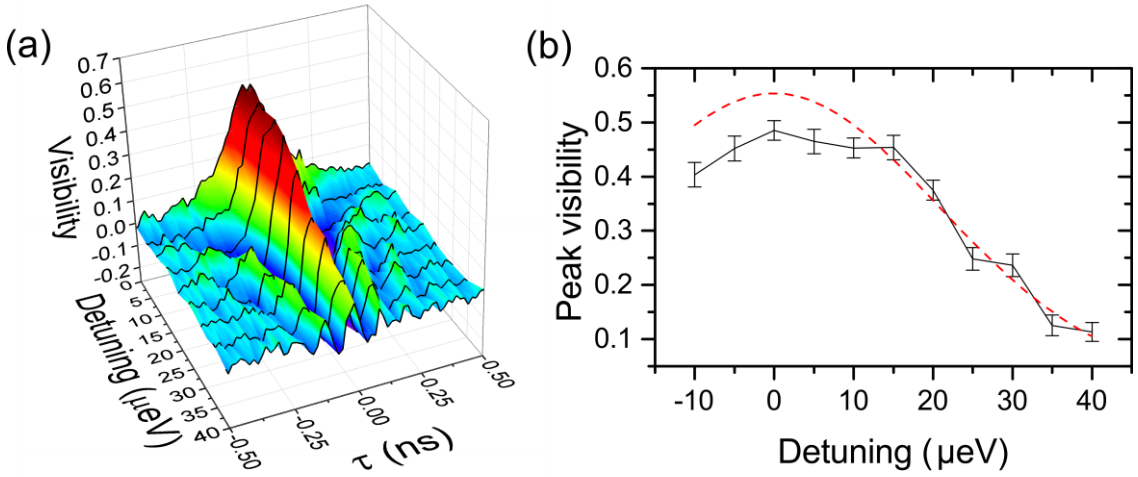

Figure 4.3: (a) Two-photon interference visibility as a function of laser-XX energy detuning. (b) Peak visibility $V(\tau = 0)$ as a function of detuning. Red dashed curve shows prediction from simulations.

4.3 Quantum teleportation of a laser photon

4.3.1 Experimental setup

Having verified that quantum interference on the unbalanced beamsplitter works as expected, we can turn our attention to the goal: to perform quantum teleportation with dissimilar light sources. For this purpose we extend our fibre-based setup to what is schematically showed in figure 4.4. A fibre-based polarising beamsplitter (PBS) is placed in the output port of the 95:5 splitter, forming a Bell-state measurement apparatus together with SSPDs D1 and D2 measuring in the H/V basis coinciding with the X eigenstates. In usual teleportation jargon we call this part of the setup 'Alice'. Note that compared to chapter 3 Alice is detecting both photons in the *same* output port of the beamsplitter. 'Bob' receives the X target photons propagating in mode 5 and is equipped with a PBS and avalanche photodiodes (D3, D4) to interrogate the polarisation state of the received X photons. All polarisation measurement bases are selected using electrical polarisation controllers (not shown) calibrated using an external laser beam.

Detection times are measured relative to detections by Alice's detector D1 (detecting H), with τ_1 signifying the detection time of D2 and τ_2 the detection time of Bob's detectors D3 or D4. In this way, we can build up time-resolved third-order correlation functions of two-fold detections by Alice and polarisation-dependent detection by Bob. The experimentally determined pair-wise detector resolutions were; D1-D2: 80 ps, D1-D3: 340 ps, D1-D4: 360 ps.

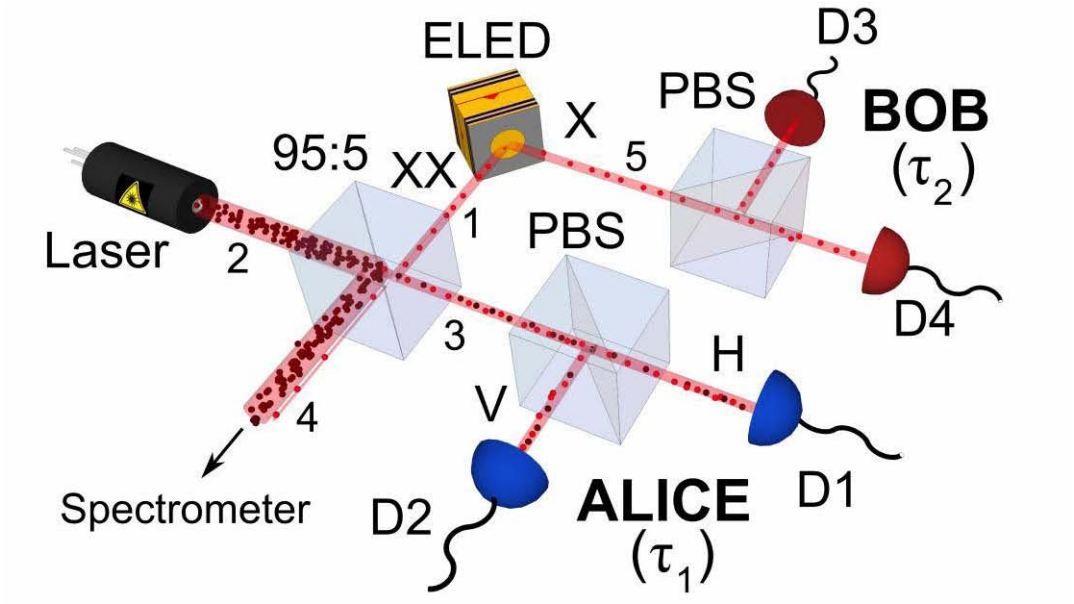

Figure 4.4: Schematic of setup implemented in single-mode fibre for quantum teleportation of polarisation states carried by laser photons. On Alice's side the teleporter comprises an unbalanced beamsplitter (95:5), polarising beamsplitter (PBS) set to measure in the H/V basis and superconducting single-photon counting detectors (D1, D2). Bob receives the X photons from the ELED and is equipped with a PBS and avalanche photo-diodes (D3, D4) to interrogate the teleported state.

4.3.2 Modelling quantum teleportation

4.3.2.1 Conditional probability

Detecting two photons on Alice's detectors D1 and D2, where D1 and D2 resolve orthogonal polarisations H and V in the *same* arm of the beamsplitter, effectively projects the detected photons onto the Bell state $|\psi_{12}^{+}\rangle$, orthogonal to $|\psi_{12}^{-}\rangle$ resolved in most quantum teleportation setups and chapter 3. With some algebra similar to equation 3.1 (page 40) we find that for an arbitrary laser input polarisation $\alpha|H_2\rangle + \beta|V_2\rangle$ we should find the teleported state received by Bob to be $\alpha|V_5\rangle + \beta|H_5\rangle$. This means the following set of unitary transformations imposed by the teleportation operation: H→V, V→H, D→D, A→A, R→L, L→R. Note the difference to teleportation in chapter 3; there it was the circular states that teleported onto the same state, here it is the diagonal states. The basic algebra considered here does not permit us to further understand and predict the performance of the teleportation of laser photons. For this purpose a more detailed model, based on spatio-temporal wavepacket models such as above in section 4.2.2, was developed and is presented in this section.

In the following, mode numbering according to figure 4.4 will be used. Let us define the laser photons to be in an arbitrary polarisation state $|C_2\rangle = \alpha|H_2\rangle + \beta\,|V_2\rangle$ while the entangled XX-X pair is assumed to be in state $|\psi_{15}\rangle = \left(|H_1H_5\rangle + e^{is\tau/\hbar}|V_1V_5\rangle\right)/\sqrt{2}$, where τ is the detection time difference between XX-X and s is the X fine-structure splitting. The joint polarisation input state of the system is thus $|\psi_{in}\rangle = |C_2\rangle|\psi_{15}\rangle$. Furthermore, let us define the electric field operators at Alice's detectors D1 and D2 to be $\hat{E}_H^+(t)$ and $\hat{E}_V^+(t)$ respectively. Bob measures an arbitrary polarisation state $|P_5\rangle = a|H_5\rangle + b\,|C_5\rangle$, and we associate the operator $\hat{E}_P^+(t)$ with the photo-detection of P-polarised photons by one of his detectors.

Our primary interest here is to first calculate the probability that Alice detects a H photon at time t and a V photon at $t+\tau_1$, while Bob detects polarisation P at $t+\tau_2$, *conditional* upon the presence of three photons in the input modes:

$$\begin{aligned} P(t, t+\tau_1, t+\tau_2) &= \left|\langle 0|\hat{E}_H^+(t)\hat{E}_V^+(t+\tau_1)\hat{E}_P^+(t+\tau_2)|\psi_{in}\rangle\right|^2 \\ &= |p(t, t+\tau_1, t+\tau_2)|^2 \end{aligned} \tag{4.9}$$

Here the probability is written with uppercase P while the probability amplitude is written with lowercase p. Using the beamsplitter mode transformations defined for the two-photon interference model in eq. 4.1 (page 62), we can relate the electric field operators at the point of detection to the operators at the input ports 1-2:

$$\begin{aligned} \hat{E}_H^+(t) &= \cos\kappa\,\hat{E}_{1H}^+(t) + \sin\kappa\,\hat{E}_{2H}^+(t) \\ \hat{E}_V^+(t) &= \cos\kappa\,\hat{E}_{1V}^+(t) + \sin\kappa\,\hat{E}_{2V}^+(t) \end{aligned} \tag{4.10}$$

Note that a polarisation dependence is kept on the operators in addition to the mode index. The electric field operator $\hat{E}_P^+(t) = \hat{E}_{5P}^+(t)$ at Bob's point of detection requires no transformation.

The probability amplitude in equation 4.9 can now be expanded:

$$
\begin{aligned}
&p(t, t+\tau_1, t+\tau_2) = \left\langle 0 \middle| \hat{E}_H^+(t)\hat{E}_V^+(t+\tau_1)\hat{E}_P^+(t+\tau_2) \middle| \psi_{in} \right\rangle = \\
&\Big\langle 0 \Big| \Big(\cos\kappa\, \hat{E}_{1H}^+(t) + \sin\kappa\, \hat{E}_{2H}^+(t)\Big)\Big(\cos\kappa\, \hat{E}_{1V}^+(t+\tau_1) \\
&\qquad + \sin\kappa\, \hat{E}_{2V}^+(t+\tau_1)\Big)\hat{E}_{5P}^+(t+\tau_2)\Big| \psi_{in} \Big\rangle = \\
&\Big\langle 0 \Big| \Big(\cos^2\kappa\, \hat{E}_{1H}^+(t)\hat{E}_{1V}^+(t+\tau_1)\hat{E}_{5P}^+(t+\tau_2) \\
&\qquad + \cos\kappa\sin\kappa\, \hat{E}_{1H}^+(t)\hat{E}_{2V}^+(t+\tau_1)\hat{E}_{5P}^+(t+\tau_2) \\
&\qquad + \cos\kappa\sin\kappa\, \hat{E}_{1V}^+(t+\tau_1)\hat{E}_{2H}^+(t)\hat{E}_{5P}^+(t+\tau_2) \\
&\qquad + \sin^2\kappa\, \hat{E}_{2H}^+(t)\hat{E}_{2V}^+(t+\tau_1)\hat{E}_{5P}^+(t+\tau_2)\Big)\Big| \psi_{in} \Big\rangle
\end{aligned}
\tag{4.11}
$$

The first and the last terms can be omitted since we are interested in a probability conditional upon *one* photon present in each input mode 1-2. The probability for multiples from either mode will be dealt with when considering intensity terms later, similar to the two-photon interference model. Having dropped these cases we have

$$
\begin{aligned}
&p(t, t+\tau_1, t+\tau_2) \\
&\qquad = \cos\kappa\sin\kappa \Big\langle 0 \Big| \Big(\hat{E}_{1H}^+(t)\hat{E}_{2V}^+(t+\tau_1)\hat{E}_{5P}^+(t+\tau_2) \\
&\qquad + \hat{E}_{1V}^+(t+\tau_1)\hat{E}_{2H}^+(t)\hat{E}_{5P}^+(t+\tau_2)\Big)\Big| \psi_{in} \Big\rangle
\end{aligned}
\tag{4.12}
$$

Following the usual approach (sections 2.1.2, 4.2.2) we can relate the electric field operator mode k to the annihilation operators:

$$
\begin{aligned}
\hat{E}_{kH}^+(t) &= \xi_k(t)\hat{a}_{kH} \\
\hat{E}_{kV}^+(t) &= \xi_k(t)\hat{a}_{kV}
\end{aligned}
\tag{4.13}
$$

Note that the annihilation (and creation) operator has been given polarisation dependence, i.e. they remove (or create) one photon of specific polarisation in mode k. As in section 4.2.2, the laser in mode 2 is CW but initially considered as a Gaussian wavepacket:

$$
\xi_2(t) = Ae^{-\frac{(t-t_0)^2}{2\sigma^2} - i\omega_2 t} \tag{4.14}
$$

$A = (\pi\sigma^2)^{-1/4}$ is a normalisation so that the integral of absolute wavepacket squared is unity and t_0 is the arrival time of the laser photon. For modes 1 and 5 carrying the XX-X pair we need to be more careful since they are populated by the entangled photon pair. We model this by defining a joint mode function,

$$
\xi_{15}(t, t') = \begin{cases} Be^{-\gamma_{xx}t - i\omega_1 t + i\Phi(t)} e^{-\gamma_x(t'-t) - i\omega_x t'}, \text{ when } t \geq 0 \text{ and } t' \geq t \\ 0, \text{ else} \end{cases} \tag{4.15}
$$

where t is the detection time of the XX photon and t' the X photon, ω_X and ω_2 are central frequency of the X and XX photon respectively. γ_{xx} is the decay rate of the XX photon and γ_X the X photon. As before, decoherence of the XX photon is modelled as a random phase fluctuation process $\Phi(t)$. Decoherence of the X photon plays no role in the teleportation experiment and is therefore ignored here. $B = 2\sqrt{\gamma_{xx}\gamma_x}$ is a normalisation factor such that $\int_{-\infty}^{\infty}\int_{-\infty}^{\infty}|\xi_{15}(t,t')|^2 dt dt' = 1$.

Putting the pieces together in equation 4.12 we get

$$\begin{aligned} & p(t, t+\tau_1, t+\tau_2) = \\ & \sin\kappa\cos\kappa\,\langle 0\big|\big(\xi_2(t)\xi_{15}(t+\tau_1, t+\tau_2)\hat{a}_{2H}(t)\hat{a}_{1V}(t+\tau_1)\hat{a}_{5P}(t+\tau_2) \\ & \qquad + \xi_2(t+\tau_1)\xi_{15}(t, t+\tau_2)\hat{a}_{2V}(t \\ & \qquad + \tau_1)\hat{a}_{1H}(t)\hat{a}_{5P}(t+\tau_2)\big)\big|\psi_{in}\rangle \end{aligned} \tag{4.16}$$

Letting the annihilation operators "work to the left" (for example: $\langle 0|\hat{a}_{1H} = \langle H_1|$) and considering the polarisation input state $|\psi_{in}\rangle = |C_2\rangle|\psi_{15}\rangle$

$$\begin{aligned} & p(t, t+\tau_1, t+\tau_2) = \\ & \sin\kappa\cos\kappa\cdot[\xi_2(t)\xi_{15}(t+\tau_1, t+\tau_2)\,\langle H_2|C_2\rangle\langle V_1 P_5(\tau_2-\tau_1)|\psi_{23}\rangle \\ & \qquad + \xi_2(t+\tau_1)\xi_{15}(t, t+\tau_2)\,\langle V_2|C_2\rangle\langle H_1 P_5(\tau_2)|\psi_{23}\rangle] \\ & \qquad = \sin\kappa\cos\kappa/\sqrt{2}\Big[\,\xi_2(t)\xi_{15}(t+\tau_1, t+\tau_2)\alpha b^* e^{\frac{is(\tau_2-\tau_1)}{\hbar}} \\ & \qquad + \xi_2(t+\tau_1)\xi_{15}(t, t+\tau_2)\beta a^*\Big] \end{aligned} \tag{4.17}$$

In the experiment we run the source in d.c. mode, i.e. the excitation time relative to the laser photon is random. In addition we do not register the absolute detection time of the H photon, t. Therefore we average over many different "H detection times" t, and many different laser photon arrival times t_0:

$$P_{HVP}(\tau_1, \tau_2) = \int_{-\infty}^{\infty}\int_{-\infty}^{\infty} p(t, t+\tau_1, t+\tau_2)\cdot p^*(t, t+\tau_1, t+\tau_2)\,dt\,dt_0 \tag{4.18}$$

Inserting the assumed mode functions (equations 4.14 and 4.15) into the above integral gives long but straight-forward integral expression that can be analytically evaluated. In the end, the probability that Alice detects a H photon at some time t and a V photon at time $t+\tau_1$ while Bob detects a photon with polarisation state $|P_5\rangle = a|H_5\rangle + b|V_5\rangle$ at time $t+\tau_2$ is:

$$\begin{aligned} P_{HVP}(\tau_1, \tau_2) = \gamma_x \sin^2\kappa\cos^2\kappa\Big[& |\alpha|^2|b|^2\cdot e^{-2\gamma_x(\tau_2-\tau_1)}\cdot\theta(\tau_2-\tau_1) \\ & + |a|^2|\beta|^2\cdot e^{-2\gamma_x\tau_2}\cdot\theta(\tau_2) + e^{-\frac{|\tau_1|}{\tau_c}-\gamma_x(\tau_2-\tau_1)-\gamma_x\tau_2}\cdot \\ & \cdot\left(\alpha\beta^* ab^*\cdot e^{\frac{is(\tau_2-\tau_1)}{\hbar}+i\Delta\omega\tau_1} + \alpha^*\beta a^* b\cdot e^{-\frac{is(\tau_2-\tau_1)}{\hbar}-i\Delta\omega\tau_1}\right) \\ & \cdot\theta(\tau_2-\tau_1)\cdot\theta(\tau_2)\Big] \end{aligned} \tag{4.19}$$

where $\theta(\tau)$, the Heaviside step function, is used to describe discontinuities:

$$\theta(\tau) = \begin{cases} 1, \tau \geq 0 \\ 0, else \end{cases}$$

Equation 4.19 is quite complicated, depending on the input state $|C_2\rangle = \alpha|H_2\rangle + \beta\,|V_2\rangle$, Bob's detected polarisation $|P_5\rangle = a|H_5\rangle + b|V_5\rangle$, the decay rate γ_x and fine-structure s of the X state, the coherence time of the XX photons τ_c and the source detuning $\Delta E = \hbar\Delta\omega$. In particular the fine-structure and the source's detuning are interesting, showing up as oscillating factors on the last term. For superposition states on the equator of the Poincaré sphere, for example D ($\alpha = \beta = 1/\sqrt{2}$) the first two terms will be of equal magnitude whether Bob detects D or A

($a = 1/\sqrt{2}, b = \pm 1/\sqrt{2}$). The difference will be made by the last term which embodies the interference in Alice's Bell state measurement. Since it decays exponentially with the XX coherence time, teleportation will only succeed for $|\tau_1| \sim 0$. Figure 4.5 illustrates the effect of above discussed parameters on $P_{HVP}(\tau_1, \tau_2)$ for input state D. With no detuning and zero FSS, the probability for Bob to detect D is high near $\tau_1 = 0$, but low for output A (panels a-b). For large τ_1 comparable to τ_c the probabilities to detect D and A are identical. If we assume a large FSS (panel c) or detuning (panel d) of 40 μeV oscillations appear, making detection of the expected state D less likely at certain times. The effect when using realistic photon detectors will be to wash out the signature of teleportation.

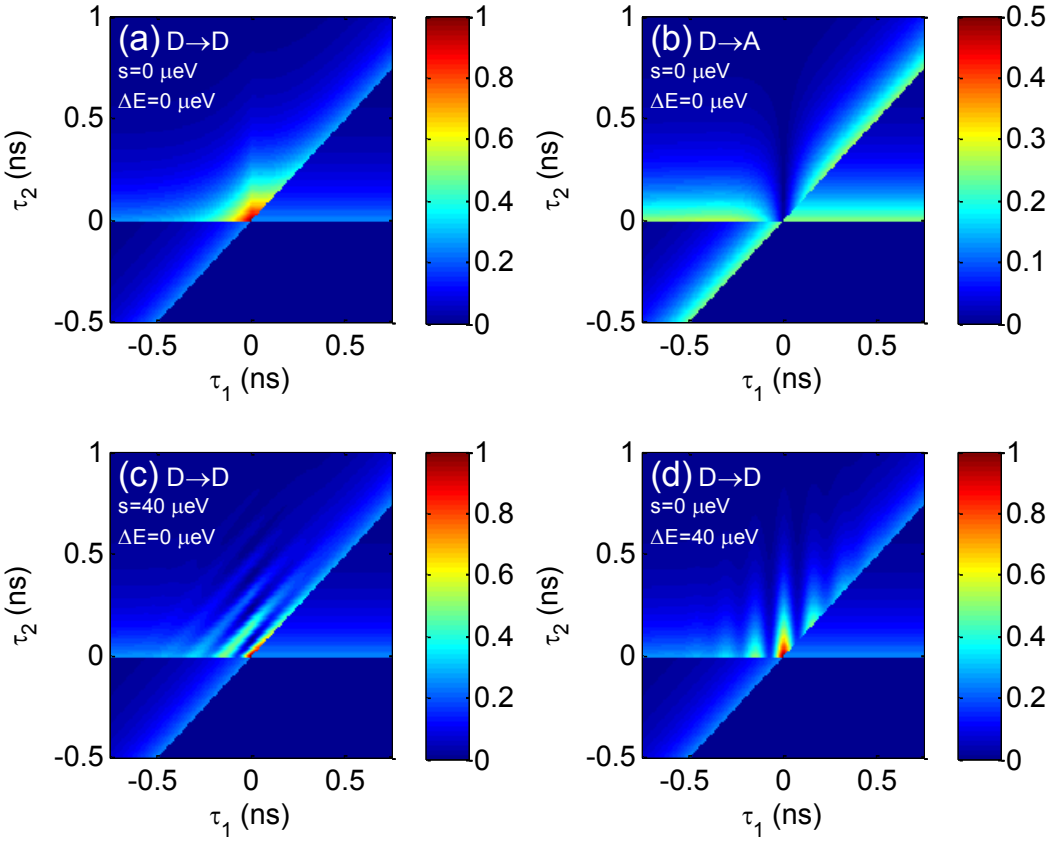

Figure 4.5: Detection probability $P_{HVP}(\tau_1, \tau_2)$ for input state D and (a) no exciton FSS ($s = 0$) and perfectly tuned light sources ($\Delta E = 0$) when Bob detects the expected output state D and (b) Bob detects A. Note that the colour scale is different to better visualise the vanishing probability to detect A at $\tau_1 = 0$ where interference occurs. (c) Bob detects the expected output state D but large FSS ($s = 40$ μeV) causes oscillations in detection probability. (d) Bob detects D but large source detuning ($\Delta E = 40$ μeV) cause oscillations in detection probability.

The probability $P_{HVP}(\tau_1, \tau_2)$ derived in this section is conditional upon the presence of three photons in the input modes 1-3, and would be appropriate for a deterministic entangled source which always produces an entangled pair in ports 2-5. This is however not yet the case for the ELED used in the experiments presented in this chapter, and how we account for this is described in the next section.

4.3.2.2 Empirical parameters characterising the entangled photon source

Accounting for uncorrelated biexciton-exciton emission

$P_{HVP}(\tau_1, \tau_2)$ derived in the section above is a probability per unit time that Alice registers a H photon at some time t followed by a V photon at $t + \tau_1$, and that Bob detects a P-polarised photon at time $t + \tau_2$. $P_{HVP}(\tau_1, \tau_2)$ tails off with rate γ_x towards zero, reflecting the lifetime of the X state correlated with the XX photon. $P_{HVP}(\tau_1, \tau_2)$ is however a simplified model, which would be directly applicable for a deterministic photon pair source that always prepares the system in the XX state after which it can relax unperturbed. Here, the source is operated in d.c. mode, which means that we do not always get an X photon after the emission of an XX photon. Sometimes a re-excitation of XX will occur, or an electron (hole) will tunnel in, changing the X complex into an X^- (X^+) complex, thus destroying the polarisation correlation between XX and X photons. In typical d.c. polarisation correlation measurements we detect many photons with time difference between XX-X detection events much larger than $\sim 1/\gamma_x$, i.e. they are not from the same cascade, and so we do in the measurements of third-order correlation functions $g^{(3)}$'s presented in section 4.3.3. Since the exact quantum dot state level system is difficult to model accurately, we deal with these deviations from an ideal source in a semi-empirical way by separating the intensity correlations from the polarisation correlations between XX and X photons[60], and begin by asking ourselves the question "provided that Alice has made a coincident detection and Bob has a photon present in mode 3, what is the probability that he finds polarisation P"?

Suppose that we have two uncorrelated photons from the ELED in input modes 1 and 5, and a control laser photon with polarisation C in mode 2. The photons in Alice's system will with probability $\sin^2\kappa\cos^2\kappa$ go into the arm of the unbalanced beamsplitter where the Bell state measurement is carried out. The uncorrelated photons "masquerading" as an XX-X pair is assumed to be completely mixed and will thus with probability 1/4 have polarisations H-P, and with equal probability 1/4 it has polarisations V-P. Hence, the probability for us to detect polarisations H-V-P for these uncorrelated photons is

$$\sin^2\kappa\cos^2\kappa\left(|\langle C|H\rangle|^2\cdot\frac{1}{4}+|\langle C|V\rangle|^2\cdot\frac{1}{4}\right)=\sin^2\kappa\cos^2\kappa\cdot\frac{1}{4} \tag{4.20}$$

We calculate a probability $F_P(\tau_1, \tau_2)$ weighted between the correlated photon events, represented with the first term $P_{HVP}(\tau_1, \tau_2)$ and uncorrelated photon events occurring with relative intensity Γ_b represented by a second term. We normalise to the total intensity which includes the complement of Bob's detection (i.e. probability to detect polarisation *Q*, orthogonal to *P*) and arrive at a probability to find polarisation *P* in Bob's output provided a three-photon detection occurs:

$$F_P(\tau_1,\tau_2)=\frac{P_{HVP}(\tau_1,\tau_2)+\Gamma_b\sin^2\kappa\cos^2\kappa\frac{1}{4}}{\left(P_{HVP}(\tau_1,\tau_2)+P_{HVQ}(\tau_1,\tau_2)\right)+\Gamma_b\sin^2\kappa\cos^2\kappa\frac{1}{2}} \tag{4.21}$$

We can see that the above expression approaches 1/2 for large times, i.e. the photons will be uncorrelated either because the two-photon interference on Alice's side failed (large τ_1) or the XX-X pair was not emitted in the same emission cycle (large τ_2).

Estimating empirical parameters

There are two free parameters in the above description, Γ_b and γ_x. The values of these can be estimated from the XX-X polarisation correlation measurements presented in section 3.2.2. With an assumed XX-X joint wavepacket of the form given in eq. 4.15 the probability to detect polarisation P for the XX photon at some time t, and Q for the X photon at time $t+\tau$ can be calculated:

$$\begin{aligned} P_{PQ}(\tau) &= \int_0^\infty dt|A|^2 e^{-2\gamma_{xx}t-2\gamma_x(t+\tau-t)}|\langle PQ(\tau)|\psi\rangle|^2 \\ &= |A|^2 e^{-2\gamma_x\tau}\,|\langle PQ(\tau)|\psi\rangle|^2 \int_0^\infty dt\, e^{-2\gamma_{xx}t} \\ &= 2\gamma_x e^{-2\gamma_x\tau}\,|\langle PQ(\tau)|\psi\rangle|^2 \end{aligned} \tag{4.22}$$

where $|\psi\rangle = (|HH\rangle + \exp(is\tau/\hbar)|VV\rangle)/\sqrt{2}$ is the usual XX-X biphoton polarisation state. Using equation 4.22 and again making the same assumption of the source being a mixture of a "perfect" biphoton emitter and a completely mixed source, on can readily calculate the degree of correlation in different polarisation bases P/Q:

$$\begin{aligned} C_{PQ} &= \frac{\left[\left(P_{PP}(\tau)+\Gamma_b\cdot\frac{1}{4}\right)-\left(P_{PQ}(\tau)+\Gamma_b\cdot\frac{1}{4}\right)\right]}{\left[\left(P_{PP}(\tau)+\Gamma_b\cdot\frac{1}{4}\right)+\left(P_{PQ}(\tau)+\Gamma_b\cdot\frac{1}{4}\right)\right]} \\ &= \frac{\left[P_{PP}(\tau)-P_{PQ}(\tau)\right]}{\left[P_{PP}(\tau)+P_{PQ}(\tau)+\Gamma_b\cdot\frac{1}{2}\right]} \\ &= \frac{2\gamma_x e^{-2\gamma_x\tau}\cdot\left(\,|\langle PP|\psi\rangle|^2-\,|\langle PQ|\psi\rangle|^2\right)}{\gamma_x e^{-2\gamma_x\tau}+\frac{1}{2}\Gamma_b} \\ &= \pm\frac{\gamma_x e^{-2\gamma_x\tau}\cos s\tau/\hbar}{\gamma_x e^{-2\gamma_x\tau}+\frac{1}{2}\Gamma_b} \end{aligned} \tag{4.23}$$

In the above expression the degree of correlation takes on the negative sign in the circular basis and positive in the linear bases. Experimentally, we have already measured and presented (section 3.2.2) the polarisation correlations in three bases; rectilinear (H/V), diagonal superposition basis (D/A) and circular superposition basis (R/L).

Figure 4.6(a) shows the experimentally determined degrees of correlation, calculated according to eq. 2.10 of section 2.2.1.2, along with fits to eq. 4.23 above. The fitting was done manually, and for $\Gamma_b = 0.45$ ns^{-1} and $\gamma_x = 2.5$ ns^{-1} reasonable agreement is found. Also shown in figure 4.6(b) is the fidelity to the ideal Bell state $|\Phi^+\rangle$ calculated from the degree of correlation (eq. 2.10), which agrees well with experiment.

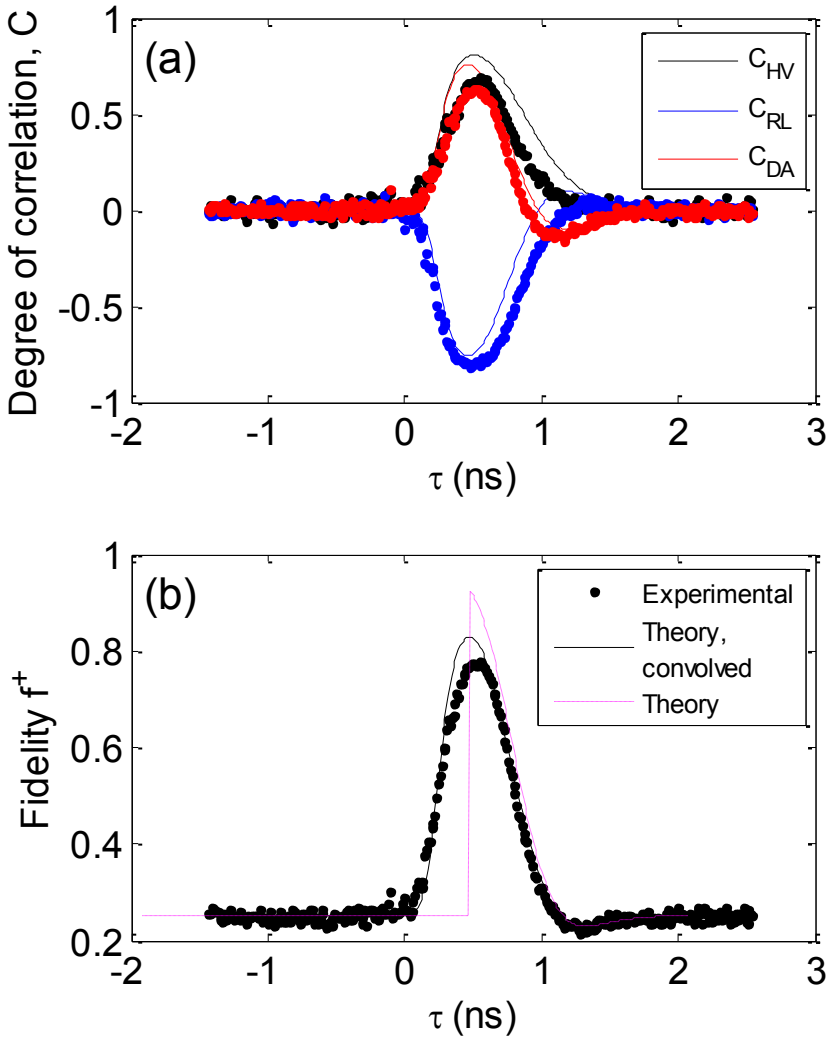

Figure 4.6: (a) Degree of polarisation from polarisation correlation measurements of XX-X photon pairs, plotted as a function X detection time τ after XX. Correlations shown in rectilinear H/V (black), circular R/L (blue) and diagonal superposition (red) polarisation bases. Solid lines show fits. (b) Entanglement fidelity f^+ to the ideal Bell state $|\Phi^+\rangle$. Experimental results are shown with black points, lines show results from empirical fit with the black one including finite detector response and dashed one being the underlying theoretical curve, assuming infinitely fast detectors.

Simulating third-order correlation functions

Having formulated $F_P(\tau_1, \tau_2)$ in equation 4.21 above and determined the free parameters from independent experimental observations we are in a position where we can start to make predictions about the performance of the ELED-based teleporter based on the finite XX coherence time and the entanglement fidelity of the XX-X pair. However, experimentally we measure third-order correlation functions using the setup presented in figure 4.4, and these measurements will also include errors due to multiple photons generated by the light sources. Therefore, we calculate the third-order correlations by taking these factors into account in a similar way as for two-photon interference (equation 2.15 in section 2.1.2 and equation 4.8 in section 4.2.2).

We let α'^2 be proportional to the intensity of the laser in input port 2, then $\alpha^2 = \sin^2\kappa \cdot \alpha'^2$ is proportional to the laser intensity in mode 3, Alice's detection arm. Similarly, the quantum dot intensity at the input of the beamsplitter is proportional to η', and the intensity in Alice's detection arm is $\eta = \cos^2\kappa\,\eta'$. Now we can consider different ways to register three photons:

(1) **Desired case:** one photon from laser and one from QD detected by Alice. This occurs with relative intensity *after beamsplitter* proportional to $\eta \cdot \alpha^2$ and can be realised in two ways:

a) Control photon went to H-detector, ancilla to V-detector (probability $|\langle C|H\rangle|^2 \cdot \frac{1}{2}$). This means that Bob's X photon has an intensity correlation with V-detector's (D2) photon: $g^{(2)}_{V,X}(\tau_2 - \tau_1)$

b) Control photon went to V-detector, ancilla to H-detector and is detected (with probability $|\langle C|V\rangle|^2 \cdot \frac{1}{2}$). This means Bob's photon has an intensity correlation with H-detector's (D1) photon: $g^{(2)}_{H,X}(\tau_2)$

Finally, conditional on one photon from the laser and two from the quantum dot being detected by Alice and Bob, the probability that the exciton is found to have polarisation P is $F_P(\tau_1, \tau_2)$. Collecting the terms we get:

$$\alpha^2\eta\left(\frac{1}{2}|\langle C|H\rangle|^2 g^{(2)}_{V,X}(\tau_2 - \tau_1) + \frac{1}{2}|\langle C|V\rangle|^2 g^{(2)}_{H,X}(\tau_2)\right) \cdot F_P(\tau_1, \tau_2)$$

(2) **Multiple XX photons from ELED:**
Two XX photons are emitted and detected as H and V by Alice with relative intensity proportional to $\eta^2/4$, and the X photon relative intensity to polarisation P is 1/2. But now all three photons originate form the quantum dot, so for a complete description we would need something like a third-order-correlation function for the quantum dot only, capturing the sub-Poissonian nature of the XX transition as well as the XX-X correlations. We have found that approximating this with $g^{(2)}_{HBT}(\tau_1) \cdot g^{(2)}_{XX-X}(\tau_2) \cdot g^{(2)}_{XX-X}(\tau_2 - \tau_1)$ agrees reasonably well with experimental observations. For this second contribution to measured third-order-correlations we finally get:

$$\frac{\eta^2}{8} g^{(2)}_2(\tau_1) g^{(2)}_{HP}(\tau_2) g^{(2)}_{VP}(\tau_2 - \tau_1)$$

(3) **Multiple photons from the laser:** The relative intensity of having two photons originating from the laser in Alice's measurement arm is $\alpha^4/2$ as given by Poissonian statistics. The final term includes the probability to detect one as H, and one as V, as well as a relative probability of find the (uncorrelated) X photon to have polarisation P (1/2):

$$\frac{\alpha^4}{4} \cdot |\langle C|H\rangle|^2 \cdot |\langle C|V\rangle|^2$$

In all of the above expressions we have dropped the unbalanced coupling ratios $\cos^2\kappa$ and $\sin^2\kappa$ since they are bundled into the intensities η and α^2 after the beamsplitter. A low intensity approximation is adopted, taking only up to two photons from each source into account. The relative intensities of the light sources after the unbalanced beamsplitter are easily measured using detectors D1 and D2.

Collecting all the terms (1)-(3) above we get

$$\begin{aligned} g^{(3)}_{HVP}(\tau_1,\tau_2) \propto \alpha^2\eta\Big(&\frac{1}{2}|\langle C|H\rangle|^2 g^{(2)}_{VX}(\tau_2-\tau_1) \\ &+\frac{1}{2}|\langle C|V\rangle|^2 g^{(2)}_{HX}(\tau_2)\Big)F_P(\tau_1,\tau_2) \\ &+\frac{\eta^2}{8}g^{(2)}_{HBT}(\tau_1)g^{(2)}_{HP}(\tau_2)g^{(2)}_{VP}(\tau_2-\tau_1) \\ &+\frac{\alpha^4}{4}|\langle C|H\rangle|^2\cdot|\langle C|V\rangle|^2 \end{aligned} \tag{4.24}$$

which can trivially be normalised so that $g^{(3)}_{HVP}(\tau_1\to\infty,\tau_2\to\infty)=1$. Convolving the above expression with the measured detector time responses we arrive at simulated functions $g^{(3)}_{HVP}(\tau_1,\tau_2)$ that, as we shall see in the next section, compare well with the experimental results.

Using the developed model we simulate the performance of our teleporter for different laser to quantum dot intensity ratios (η/α^2) and detunings ΔE for a superposition control input state such as $|\mathrm{D}_2\rangle=(|H_2\rangle+|V_2\rangle)/\sqrt{2}$. The results, shown in 4.7 below, suggest that a fidelity of up to 75% is achievable, and in order to suffer a no more than 1% reduction from this, the energy detuning needs to be less than ~10 μeV which is experimentally feasible. We chose to perform the experiments at a quantum dot to laser intensity ratio (measured at D1 and D2) of $\eta/\alpha^2=2$ where the predicted fidelity is close to maximum.

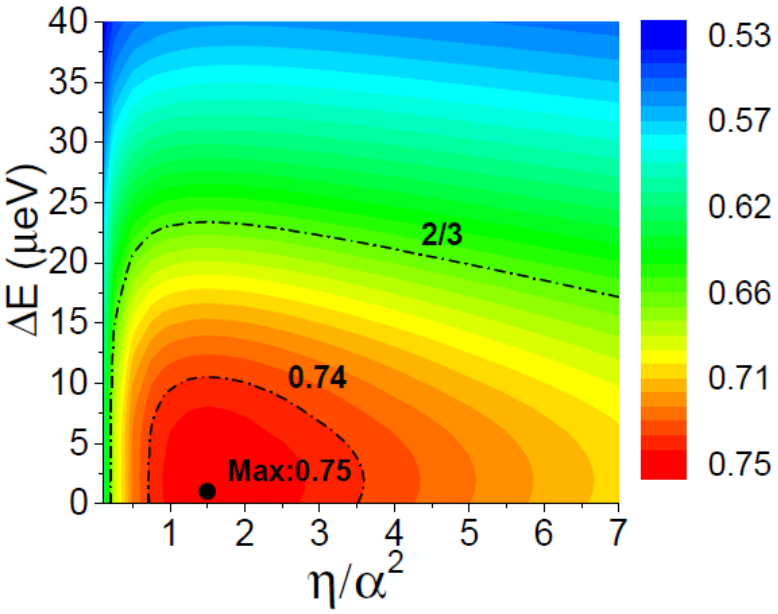

Figure 4.7: Simulated teleportation fidelity for a superposition state such as D, as a function of XX to laser intensity ratio (η/α^2) and laser-ELED energy detuning.

4.3.3 Experimental results

We test the quantum teleportation protocol for six input laser polarisation states symmetrically distributed over the Poincare sphere in three polarisation bases; the rectilinear basis H/V coinciding with Alice's measurement basis and the quantum dot exciton eigenbasis, the diagonal basis spanned by $|D/A\rangle = 1/\sqrt{2}\,(|H\rangle \pm |V\rangle)$ and the circular basis $|R/L\rangle = 1/\sqrt{2}\,(|H\rangle \pm i|V\rangle)$. The set was chosen to represent teleportation of a general qubit state. For each input state (as presented in sections 4.3.3.1-4.3.3.3) we measure the fidelity onto the expected output state by aligning Bob to the corresponding basis, i.e. he detects the expected state and the orthogonal counterpart.

4.3.3.1 Teleporting polar states

Quantum teleportation of the polar states H and V, coinciding with the X eigenstates and Alice's measurement basis, is not really 'quantum' as discussed in section 3.2.3, since they do not require interference and entanglement to work. That is true also here, despite the laser input. Figure 4.8(a) and (b) show measured third-order correlation functions for teleportation of input state H, when Bob detects V and H respectively. The vertical dark stripe at $\tau_1 = 0$ can be attributed to the sub-Poissonian nature of the XX transition, but there is only one dark vertical streak since the input photon is supplied by an independent source (in contrast to section 3.2.3 where 2-3 vertical stripes are seen). Similarly, only one horizontal feature is visible, originating from correlations between H-polarised XX photons (detected by D1) and X target photons, giving a suppression of V detections by Bob (panel a) and enhanced detection of H (panel b). The diagonal streak can be explained in the same way, but there Bob's detection is correlated with XX photons detected as V (by Alice's detector D2).

In figure 4.8(c) and (d) the simulated third-order correlation functions based on equation 4.24 are shown, reproducing all the major features in the experimental data. The fact that teleportation of H does not require interference leads to the diagonal bright feature extending through the origin in panels (a) and (c).

The bottom two panels (figure 4.8(e) and (f)) show cross-sections for coincidence by Alice ($\tau_1 = 0$) through the simulated and experimentally measured third-order correlation functions. Again, qualitatively good agreement between model and reality is found, and they both show that when Bob detects a photon shortly after Alice registers a coincidence ($\tau_2 = 0$), it is predominantly a V-polarised photon as expected from the configuration of Alice's Bell-state analyser.

We calculate the fidelity of Bob's detected photons to the expected state V by taking $f_{H\to V}(\tau_1,\tau_2) = g^{(3)}_{HVV}(\tau_1,\tau_2)/(\,g^{(3)}_{HVV}(\tau_1,\tau_2) + g^{(3)}_{HVH}(\tau_1,\tau_2))$. The result is shown in figure 4.9, with panel (a) showing the full time dependence as a function of Alice's (τ_1) and Bob's (τ_2) detection time delays. The diagonal bright streak in $g^{(3)}_{HVV}$ in figure 4.8(a) results in a fidelity exceeding 1/2 along the diagonal. The cross-section at $\tau_1 = 0$ when *general* teleportation can succeed is shown in panel (b), with a peak fidelity of $f_{H\to V} = 0.835 \pm 0.026$. The red solid lines show fidelities calculated using the modelled third-order-correlation functions, exhibiting good agreement with measurements also here.

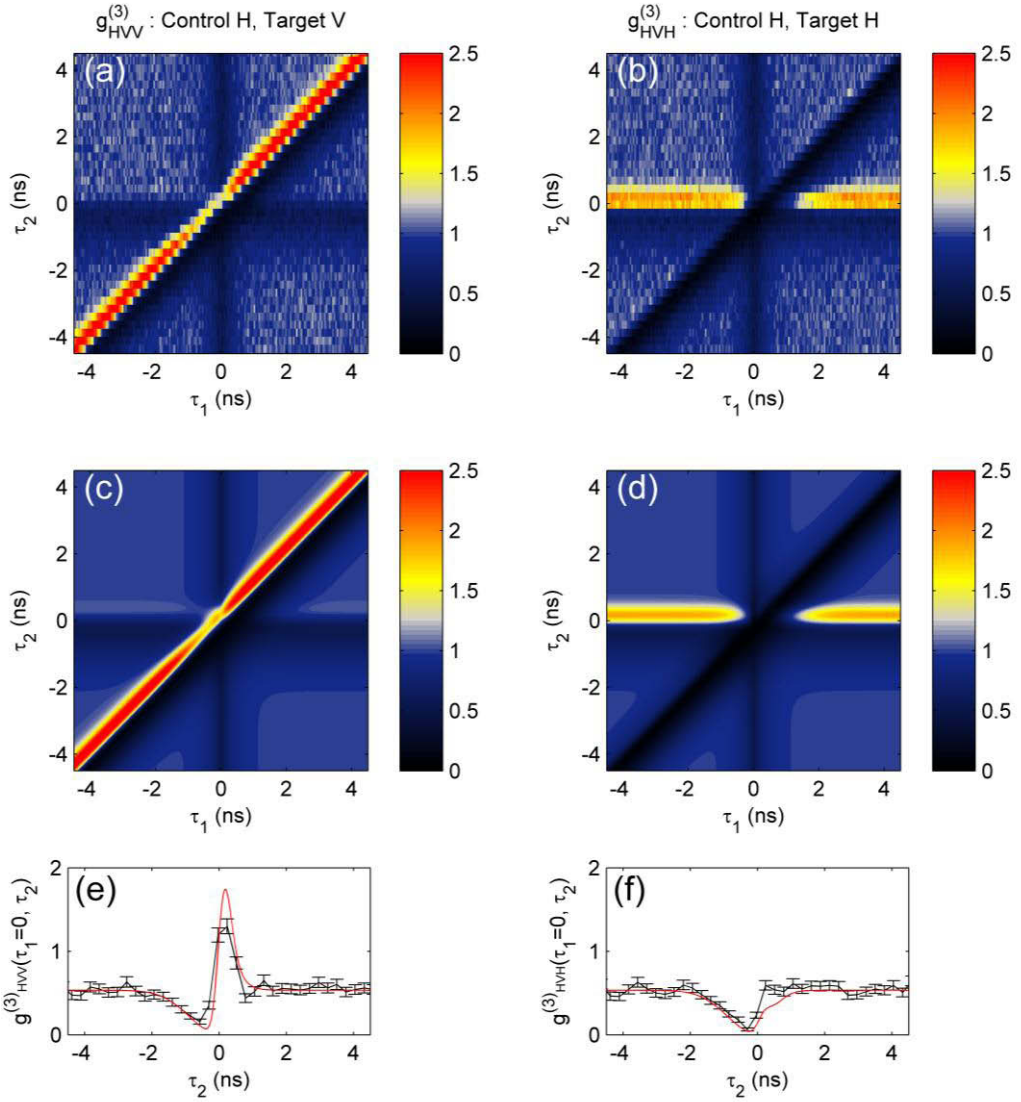

Figure 4.8: Measured third-order correlation functions for control state H for (a) Bob detecting target V, $g^{(3)}_{HVV}(\tau_1, \tau_2)$ and (b) Bob detects target H, $g^{(3)}_{HVH}(\tau_1, \tau_2)$. (c) and (d) show corresponding simulated third-order correlation functions. (e) and (f) show cross-setions through the correlations, showing that Bob detects predominantly V when $\tau_2 \sim 0$. The black curve shows experimental results with Poissonian counting statistics indicated by error bars, red curve is simulated correlation function.

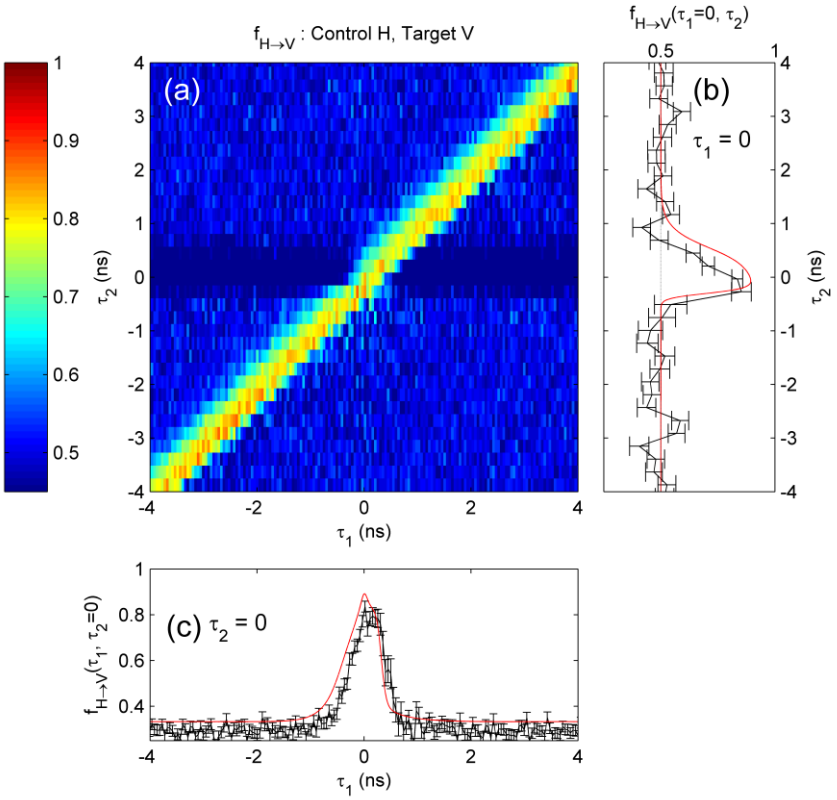

Figure 4.9: (a) Experimentally measured fidelity of control input H onto target V as a function of τ_1 and τ_2. At the origin $\tau_1 = \tau_2 = 0$ where teleportation of a general state can succeed a peak fidelity of 0.835±0.026 is found. (b) Cross-section for $\tau_1 = 0$ when Alice registers coincidence. (c) Cross-section for τ_2 along Alice's time axis τ_1. Red curves in (b) and (c) show modelled fidelity.

4.3.3.2 Teleporting superposition states

Superposition states are far more interesting and reveal more about the character of the teleporter, since they rely on two distinct quantum physical aspects to work: entanglement and quantum interference. Four superposition states evenly distributed on the equator of the Poincaré sphere were tested, D/A and R/L. In this section results for A and R laser polarisations are presented.

Figures 4.10(a) and (b) show the measured third-order correlation functions for the input laser polarised along A when Bob measures A (panel a) and D (panel b) respectively. Here the diagonal and horizontal features are of approximately the same magnitude, and also similar between the two panels (a) and (b), since an A- or D-polarised X photon detected by Bob is as likely to be "paired up" with an H-polarised as a V-polarised XX photon. Crucially, panel (b) shows a clear absence of D-polarised target photons at the origin, i.e. where interference in Alice's unbalanced beamsplitter can take place and the Bell-state measurement succeeds, projecting the target photon onto the expected output A. Indeed the diagonal and horizontal features in panel (a) go through the origin. The clear difference between panels (a) and (b) at the origin indicates successful teleportation of polarisation state A to A. Figure 4.10(c) and (d) show simulated third-order correlation functions that reproduce all these main features observed experimentally. In panels (e) and (f) cross-sections for $\tau_1 = 0$ are shown, also showing that Bob receives predominantly A-polarised X photons when they are detected shortly after Alice's coincidence, i.e. when the XX-X pair is from the same radiative decay cycle.

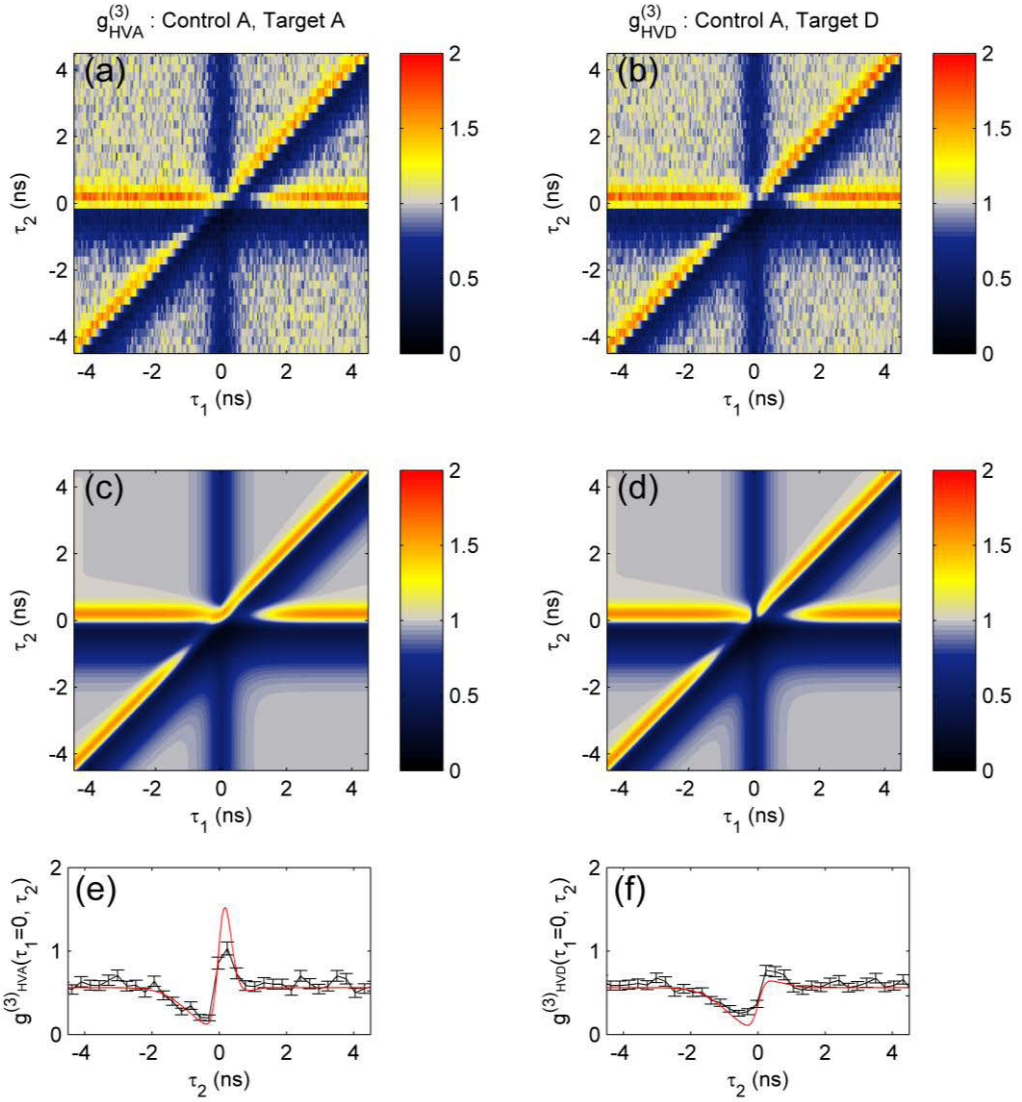

Figure 4.10: Measured third-order correlation functions for control state A for (a) Bob detecting target A, $g^{(3)}_{HVA}(\tau_1, \tau_2)$ (b) Bob detects target D, $g^{(3)}_{HVD}(\tau_1, \tau_2)$. (c) and (d) corresponding simulated third-order correlation functions. (e) and (f) cross-sections through the correlations, illustrating that Bob detects predominantly A when $\tau_2 \sim 0$. Black curve is experimental results with Poissonian counting statistics indicated by error bars, red curve is simulated correlation function.

Figure 4.11(a) shows the fidelity of input A onto A as a function of detection time delays. For this superposition state, in contrast to the polar state H (figure 4.9), only a small high-fidelity spot exists, limited in τ_1-direction by the coherence time of the XX photons and in τ_2-direction by the effective lifetime of the correlated X photons emitted after the XX photons. We find a fidelity $f_{A\to A} = 0.698 \pm 0.033$ when $\tau_1 = \tau_2 = 0$. Measurements and model agree qualitatively well as evidenced in the cross-sections through $f_{A\to A}(\tau_1, \tau_2)$ in panels (b) and (c).

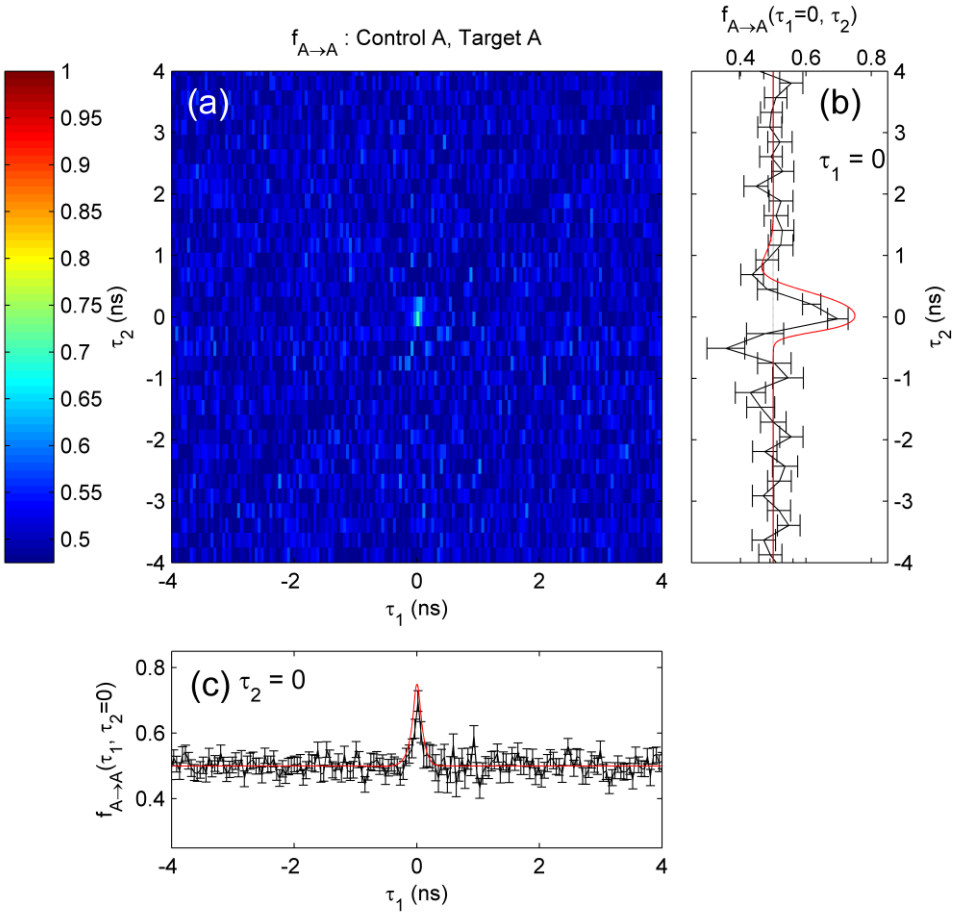

Figure 4.11: (a) Experimentally measured fidelity of control input A onto target A as a function of τ_1 and τ_2. The high-fidelity spot at $\tau_1 \sim \tau_2 \sim 0$ indicates teleportation for three-fold coincidence with fidelity value 0.698±0.033 to A. (b) Cross-section for $\tau_1 = 0$ when Alice registers coincidence. (c) Cross-section for $\tau_2 = 0$ along Alice's time axis τ_1. Red curves in (b) and (c) show modelled fidelity.

Teleporting a superposition state in the circular basis is very similar to the diagonal basis. Figure 4.12 presents the measured (panels a, b) and simulated (panels c, d) third-order correlation functions when the laser photons are carrying polarisation state R. The difference to the diagonal basis is that in the circular basis we expect the states to teleport to the orthogonal state. This is also what we see when comparing figure panels 4.12(a) and (c) with (b) and (d); Bob receives mainly L polarised X photons near the origin.

In figure 4.13(a) the detection time-dependent fidelity $f_{R\to L}(\tau_1, \tau_2)$ is shown, together with cross-sections through the origin in panels (b) and (c) showing good agreement between model and experimental data. At the origin we find a teleportation fidelity of $f_{R\to L} = 0.744 \pm 0.028$.

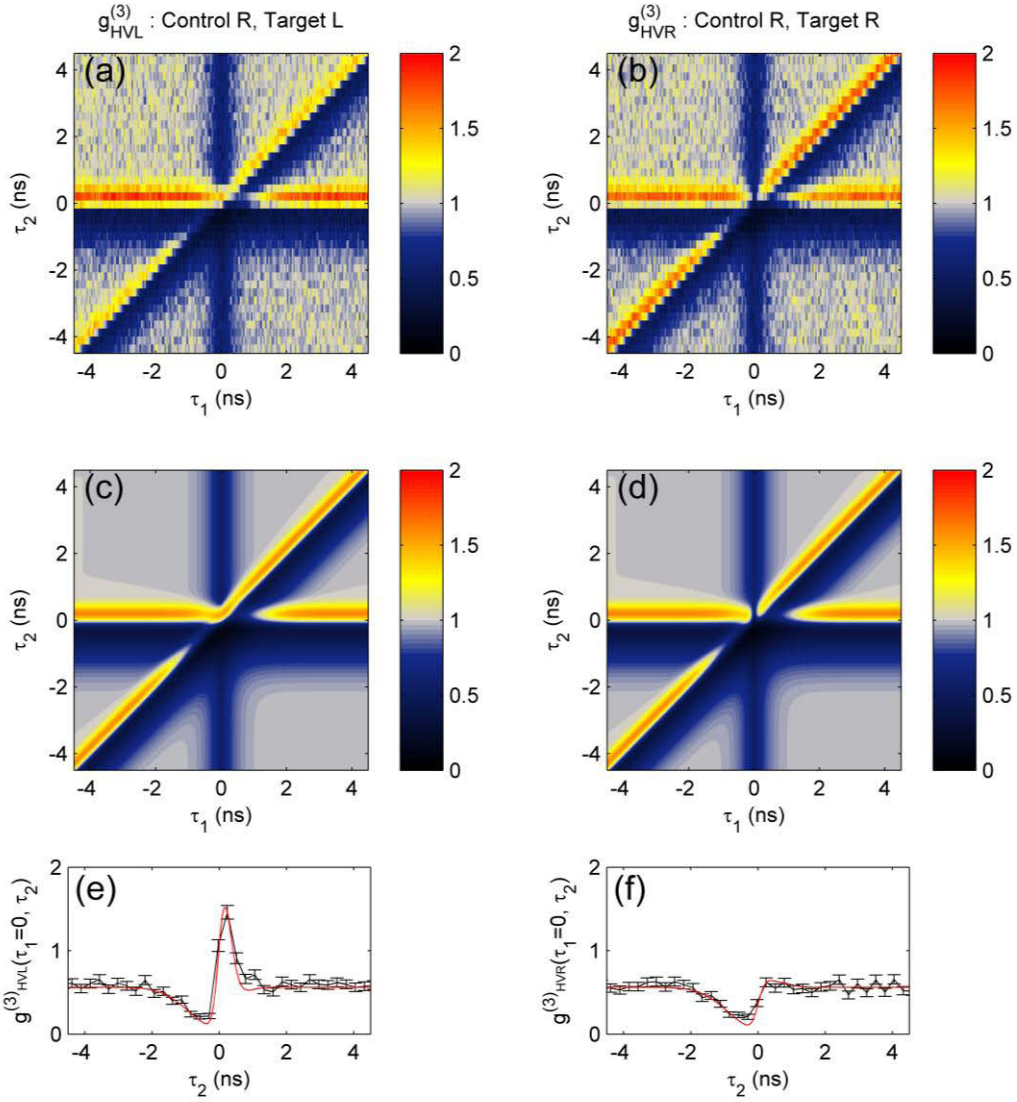

Figure 4.12: Measured third-order correlation functions for control state R for (a) Bob detecting target L, $g^{(3)}_{HVL}(\tau_1, \tau_2)$ (b) Bob detects target R, $g^{(3)}_{HVR}(\tau_1, \tau_2)$. (c) and (d) show corresponding simulated third-order correlation functions. (e) and (f) show cross-sections through the correlations, showing that Bob detects predominantly L when $\tau_2 \sim 0$. Black curve is experimental results with Poissonian counting statistics indicated by error bars, red curve is simulated correlation function.

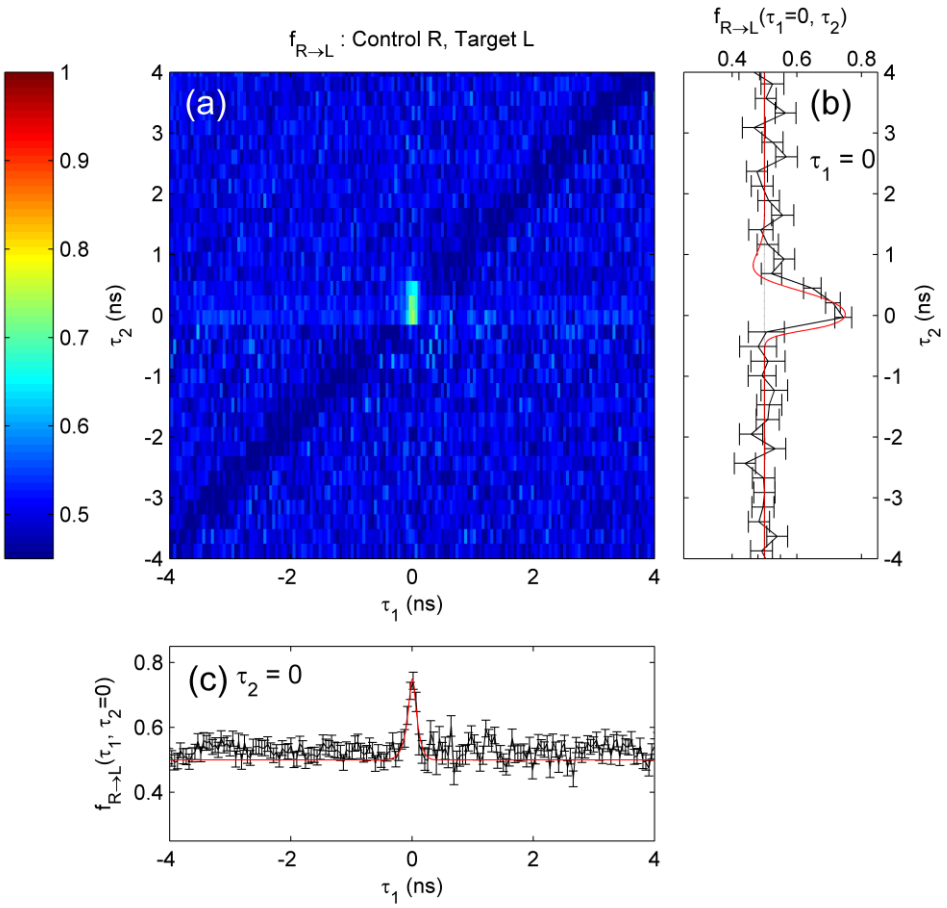

Figure 4.13: (a) Experimentally measured fidelity of control input R onto target L as a function of τ_1 and τ_2. The high-fidelity spot at $\tau_1 \sim \tau_2 \sim 0$ indicates teleportation for three-fold coincidence with fidelity 0.744±0.028 to L. (b) Cross-section for $\tau_1 = 0$ when Alice registers coincidence. (c) Cross-section for $\tau_2 = 0$ along Alice's time axis τ_1. Red curves in (b) and (c) show modelled fidelity.

4.3.3.3 Teleportation of a general input state

Fig 4.14 shows the simulated and experimentally measured fidelities for the six individual laser polarisation states measured. The polar states on the Poincaré sphere coinciding with Alice's measurement basis show the highest fidelity as expected ($f_{H\to V} = 0.835 \pm 0.026$, $f_{V\to H} = 0.861 \pm 0.024$), as these do not require successful interference in the Bell-state measurement apparatus, and could be done with just classically correlated photon pairs. The four superposition states, which rely on both successful interference *and* entanglement, all have relatively similar output fidelities ($f_{D\to D} = 0.725 \pm 0.032$, $f_{A\to A} = 0.698 \pm 0.033$, $f_{R\to L} = 0.744 \pm 0.028$, $f_{L\to R} = 0.741 \pm 0.031$). The slightly higher fidelity in the circular basis compared to the diagonal is consistent with polarisation correlations observed for this type of QD, which can be attributed to nuclear polarisation fluctuations in the quantum dot[59,100]. The simulation does not include these effects and predict the same peak fidelities for all superposition states (0.75) and also the same for the two polar states H and V (0.92).

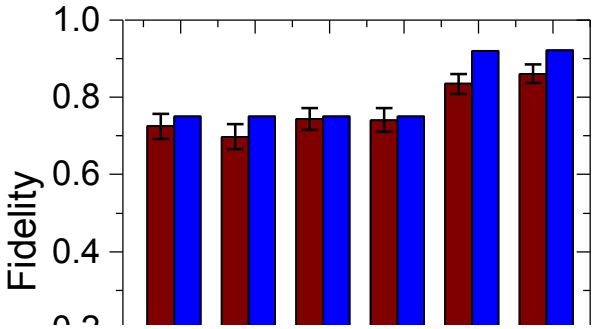

Figure 4.14: Distribution of individual output state fidelities. Experimentally measured fidelities in red, simulated in blue.

As discussed in chapter 3, for our choice of input states, the highest possible average output fidelity is 2/3 using the best possible classical teleporter[132]. Figure 4.15 below presents the average fidelity for our set of input states, shown as a function of the detection times. For coincident detection by Alice and Bob ($\tau_1 = \tau_2 = 0$) we achieve an average fidelity of 0.767 ± 0.012, clearly beating the classical limit and proving that quantum teleportation from laser photons to an X photon is taking place. Also shown in figure 4.15, projected onto the sidewalls, are cuts through the origin of the fidelity map at $\tau_1 = 0$ and $\tau_2 = 0$ together with results from the model showing good overall agreement. At $\tau_1 = 0$ (along Bob's time axis τ_2) the peak width is limited by the XX-X polarisation correlations, and for $\tau_2 = 0$ (along Alice's time axis τ_1) the peak is limited by the XX coherence time τ_c. The higher fidelity compared to the average for teleporting states encoded on another XX photon (0.704, section 3.2.5) can be explained primarily by the interference being less sensitive to the finite coherence time τ_c of the XX photons since the laser photon has (practically) infinite coherence length; we can see this in equation 4.19 where the interfering term drops as $\exp(-|\tau_1|/\tau_c)$ whereas if we interfered two XX photons it would drop twice as fast (see for example eq. 2.7 in section 2.1.2).

The main source of uncertainties in all experiments is due to the photon counting statistics. Quoted errors on teleportation fidelities include in addition to this an uncertainty in time calibration of the photon correlation equipment (less than 1% on individual fidelities).

During the teleportation experiment we also collect detection events to probe the statistics of the X photons going down the optical fibres to Bob, essentially performing a Hanbury-Brown-Twiss measurement using his detectors (D3-D4) simultaneously as the laser photons are being teleported. The resulting second-order correlation function is shown in figure 4.16 and we find a characteristic dip with minimum $g^{(2)}_{X-X}(0) = 0.247 \pm 0.001$, which confirms that the setup erases the Poissonian statistical nature of the input laser field, also shown with $g^{(2)}_{laser}(0) \sim 1$. This could be useful for transferring the state carried by the laser photons into a quantum circuit and thereby reduce errors in its operation.

To conclude this section, we have proven that quantum teleportation from photons of a Poissonian light field onto photons generated by a sub-Poissonian quantum emitter is taking place.

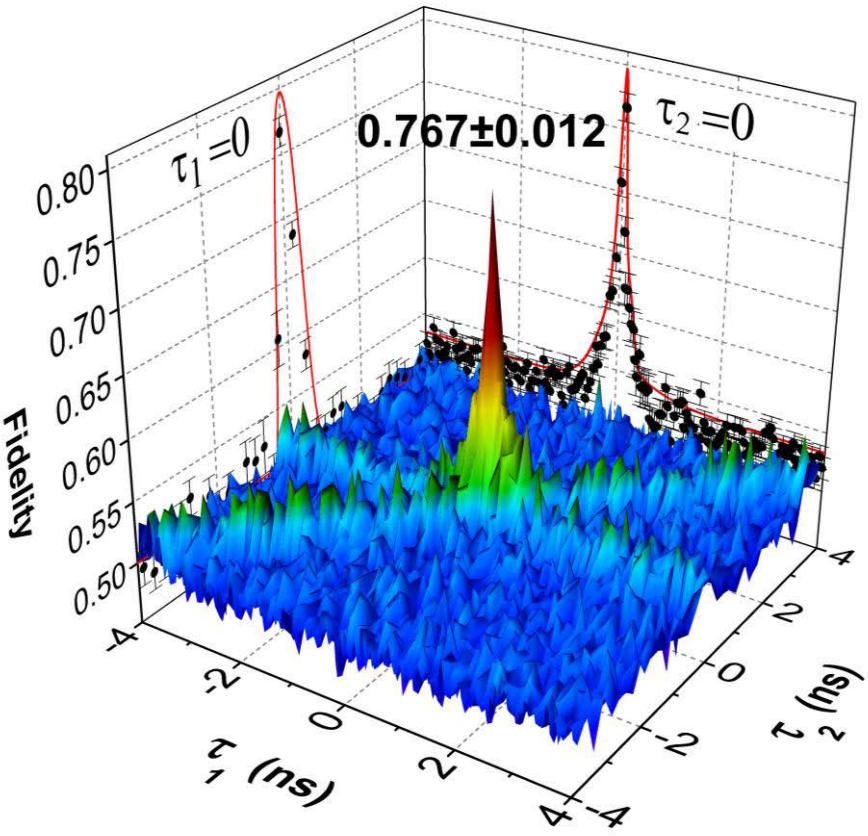

Figure 4.15: Average teleportation fidelity for six input states, as a function of Alice's detection time τ_1 and Bob's detection time τ_2. Points and red lines on projected on side-walls show cross-section through the experimental and simulated average fidelity map respectively. A peak fidelity of 0.767±0.012, beating the classical limit 2/3 and proving the quantum nature of the teleportation.

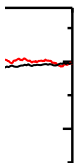

Figure 4.16: Second-order correlation function in the teleportation output received by Bob (black), based on detection events acquired during the teleportation measurements using APDs D3-D4, averaged over the six teleported states. The dip extends to 0.247±0.002 and shows that the Poissonian nature of the teleporter input laser field (red) has been erased in the output received by Bob.

4.3.3.4 Measuring the density matrix of a teleported photon

In the experiments described above Bob interrogates the output photon by measuring in the expected output polarisation basis only, which cannot reveal the full character of the output light. For example, when teleporting R Bob was aligned to record R-and L-polarised photons only. To explore the teleported states deeper we performed single qubit tomography[149] of the output photon density matrix corresponding to laser input state R by measuring the output fidelity in the three bases H/V, D/A and R/L. For a perfect quantum teleportation implementation one would expect input R to yield output L with unit fidelity and fidelity 0.5 in the H/V and D/A bases. At $\tau_1 = \tau_2 = 0$ we measure fidelities $f_{R\to L} = 0.713 \pm 0.031$, $f_{R\to D} = 0.646 \pm 0.034$ and $f_{R\to H} = 0.550 \pm 0.033$. These numbers can easily be related to the density matrix, here expressed in the rectilinear (H/V) basis:

$$\rho = \begin{pmatrix} \rho_{11} & \rho_{12} \\ \rho_{12}^* & \rho_{22} \end{pmatrix} = \begin{pmatrix} f_H & \left(f_D - \frac{1}{2}\right) + i\left(f_R - \frac{1}{2}\right) \\ \left(f_D - \frac{1}{2}\right) - i\left(f_R - \frac{1}{2}\right) & 1 - f_H \end{pmatrix} \tag{4.25}$$

We see that the diagonal elements are related to the measurements in the H/V basis, while the real (imaginary) elements are directly related to the measurements in the D/A (R/L) basis. Figure 4.17 shows the reconstructed density matrix presented in the circular basis. Clearly the output state is closest to the expected (L) and the fidelity $f_{R\to L}$ is the same as measured previously (section 4.3.3.2) within the accuracy of the experiments, but the measurements also revealed a relatively strong D component which results in the non-zero off-diagonal imaginary components in figure 4.17(b).

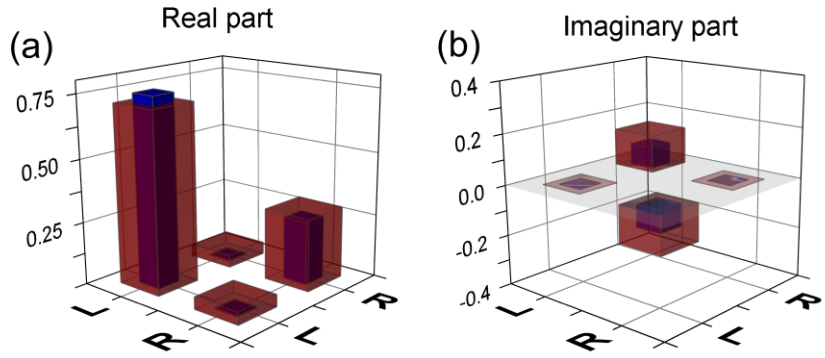

Figure 4.17: (a) Real part of density matrix of target X_t photon, for input state R at time of maximum fidelity, shown in the circular polarisation basis. The strongest element occurs for L, the expected output state. (b) Corresponding imaginary part. Red bars are experimental values, blue simulated.

The largest eigenvalue λ_1 of the density matrix tells us the maximum fidelity that can be measured, and the corresponding eigenvector $|\nu_1\rangle$ tells us the polarisation along which Bob should be aligned in order to measure this fidelity. Figure 4.18(a) shows λ_1 as a function of Bob's detection time τ_2, with an experimental peak value of 0.763±0.030 which is larger than $f_{R\to L}$. This confirms that indeed Bob's measurement of L was not optimally aligned to the actual output state. The results based on simulated third-order-correlation functions, also presented in figure 4.18(a), show good agreement.

The density matrix is diagonalised in the eigenbasis, i.e. $\rho = \lambda_1|\nu_1\rangle\langle\nu_1| + (1-\lambda_1)|\nu_2\rangle\langle\nu_2|$, but we can also model the density matrix as being composed of a fraction b of completely mixed light $(|\nu_1\rangle\langle\nu_1| + |\nu_2\rangle\langle\nu_2|)/2$ and a pure fraction $(1-b)$ of $|\nu_1\rangle\langle\nu_1|$:

$$\rho = (1-b)\cdot|\nu_1\rangle\langle\nu_1| + b\cdot\left(\frac{1}{2}|\nu_1\rangle\langle\nu_1| + \frac{1}{2}|\nu_2\rangle\langle\nu_2|\right) \tag{4.26}$$

It is then easy to relate the mixed fraction to the largest eigenvalue: $b = 2(1-\lambda_1)$. We see from figure 4.18(a) that as τ_2 increases $\lambda_1 \to 1/2$, i.e. the mixed fraction $b \to 1$ as the X photon detected by Bob is no longer from the same radiative cascade as the XX photon detected by Alice. As it carries no correlation to mediate the teleportation the target photon polarisation becomes completely randomised, i.e. the mixed fraction becomes unity.

In addition to the time dependence of λ_1 we analyse the corresponding eigenstate $|\nu_1\rangle$. Figure 4.18(b) shows the overlap with the desired output L and the orthogonal state R. Experimentally, we can follow the evolution of $|\nu_1\rangle$ up to $\tau_2 \sim 1$ ns after which the uncertainty becomes too large. In any case, a clear evolution can be seen of the output from L towards R with Bob's detection time τ_2, i.e. the delay between from Alice's coincidence to the detection of X photon. The numerical model, in contrast to the experiment, is noise-free and a pure fraction (albeit still asymptotically vanishing for large τ_2) can always be accurately separated, and as shown in Figure 4.18(b) the predicted output state evolution is well-described by the fine-structure splitting (s~2 μeV) of the X state, and the evolution rate agrees well with the experimental data.

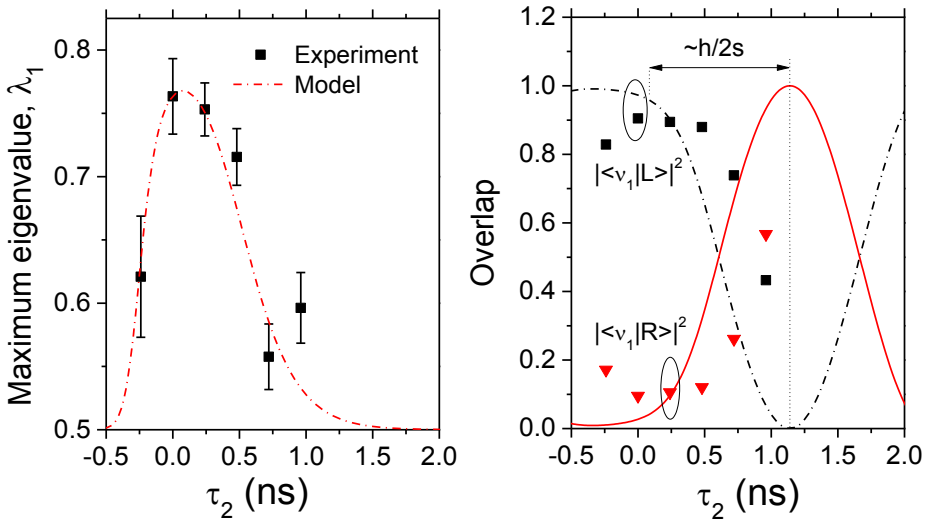

Figure 4.18: (a) Maximum eigenvalue of the density matrix as a function of Bob's detection time τ_2, taken at $\tau_1 = 0$ (when Alice registers coincidence). Simulated result shown with red dashed curve. (b) Evolution of the pure output state component of the density matrix, shown as overlap of the eigenstates $|\nu_1\rangle$ with L (black squares) and R (red triangles) respectively. Simulated curves are plotted for L (black, dashed) and R (red, solid line).

4.4 Conclusions

To conclude, we have performed photonic quantum teleportation of input states encoded on photons from a coherent light source, teleporting them onto a stream of photons from a sub-Poissonian semiconductor emitter. With further improvements of the device design, such as placing the emitter in an optical cavity[34,68,79], the teleportation method presented here could find application in e.g. the realisation of quantum relays for dissimilar light sources. The protocol used here, with a strongly unbalanced beamsplitter, could also provide a useful interface to remotely initialise quantum information circuits using ubiquitous laser-generated photons over long distances, and more "exotic" sub-Poissonian light fields in the local quantum circuit. Other interesting applications could be to secure QKD networks from Trojan horse attacks[150]. The laser-quantum emitter interface it provides is also well suited for existing QKD systems which are usually based on weak coherent pulses[151].

5 Voltage control of dynamic nuclear polarisation in single quantum dots

5.1 Introduction

Quantum dots find many potential applications in the field of quantum information processing, e.g. as quantum memories[152], coherent qubit control[22,36] and as discussed extensively in previous chapters, for generation of single photons and pairs of entangled photons. The hyperfine interactions between the localised charge carriers in the quantum dot and the mesoscopic nuclear spin system influence all above mentioned applications; it is a limiting source of dephasing in coherent manipulation schemes[153] and nuclear spin fluctuations affect the exciton eigenstates with direct impact on entangled-photon-pair generation[100]. Understanding the nuclear interactions in quantum dots is thus motivated from an application point of view, but apart from that it is also a very active field of material science in its own right. Dynamic nuclear polarisation (DNP), in which spin-polarised electrons transfer spin to the nuclei and thereby create a nuclear polarisation that acts back on the electrons (the Overhauser effect[154]), was first explored in bulk semiconductors from ~1970s for electrons localised near donors[155]. DNP effects in quantum dots, studied from the 1990s and on[156,157] differ from the bulk because of the charge confinement; the carriers interact with a comparatively small number of nuclei (10^4-10^5) making spin transfer more efficient[43], and the nuclei are largely decoupled from the surrounding bulk material which means that the spin lattice is essentially a small, isolated system with inhibited nuclear spin diffusion[158]. DNP combined with nuclear magnetic resonance techniques have been used to in detail probe the isotope composition and strain in individual quantum dots[159], and to quantify the hyperfine interaction of electrons and holes in different quantum dot material systems[160], to mention two recent examples of quantum dot material science.

This chapter starts with a description of physical processes involved in dynamic nuclear polarisation experiments in quantum dots (section 5.2) which gives a background to interpret experimental results presented in subsequent sections. DNP experiments in zero field (section 5.3.3) and in longitudinally applied fields (Faraday geometry, section 5.3.4) strongly indicate that the main parameters governing the dynamics are the electron hyperfine correlation time τ_c^e and the nuclear depolarisation time $T_{d\infty}$, and that they are interconnected and can be controlled by an applied voltage. DNP in Faraday geometry is shown to exhibit strongly non-linear bistable behaviour, and internal effective fields corresponding to several Tesla are created through optical pumping. Depolarisation measurements of optically aligned electron spin in transverse magnetic fields (Voigt geometry, section 5.3.5) also exhibit strongly non-linear behaviour and a radical departure from the standard Hanle effect[155]. The results furthermore show that quasi-resonant excitation, previously used in observation of anomalous Hanle effect in single quantum dots[161], is not a pre-requisite for such anomalous behaviour, and that the system can be voltage tuned from the anomalous to the normal Hanle regime.

5.2 Electron-nuclear spin system

All occurring isotopes in InAs/GaAs QD systems have non-zero nuclear spin (Ga and As 3/2, In 9/2) which means that hyperfine interactions can be expected to take place, and the interaction in quantum dots is particularly strong in QDs compared to bulk systems due to the charge carrier confinement[43]. The electron-nuclear interaction is usually described with a "Fermi contact" Hamiltonian proportional to $|\psi(\boldsymbol{R}_i)|^2$, the probability of finding the electron at the nuclear site $\boldsymbol{R}_i$[162]:

$$\begin{aligned} \widehat{H}_{hf} &= \nu_0 \sum_i A_i |\psi(\boldsymbol{R}_i)|^2 \, \widehat{\boldsymbol{S}} \cdot \widehat{\boldsymbol{I}}^{\boldsymbol{i}} = \\ &= \frac{\nu_0}{2} \sum_i A_i |\psi(\boldsymbol{R}_i)|^2 \cdot \left[2\hat{I}_z^i \hat{S}_z + \left(\hat{I}_+^i \hat{S}_- + \hat{I}_-^i \hat{S}_+ \right) \right] \end{aligned} \tag{5.1}$$

where the summation is over all nuclear lattice sites i, ν_0 is the crystal lattice unit cell volume, A_i is the hyperfine interaction constant for the different nuclear species ($A_{In} = 56$ μeV, $A_{As} = 46$ μeV, $A_{Ga} = 42$ μeV) and $\widehat{\boldsymbol{S}}$ and $\widehat{\boldsymbol{I}}^{\boldsymbol{i}}$ are the electron and nuclear spin operators. Here the identity $\widehat{\boldsymbol{S}} \cdot \widehat{\boldsymbol{I}}^{\boldsymbol{i}} = \hat{I}_z^i \hat{S}_z + \left(\hat{I}_+^i \hat{S}_- + \hat{I}_-^i \hat{S}_+ \right)/2$ has been used, with the second term using the ladder operators $\hat{I}_\pm^i$ and $\hat{S}_\pm$ representing the possibility for the system to perform "flip-flops", i.e. electron spin flips with transfer of angular momentum to the spin of one nucleus. Hole wavefunctions, in contrast to conduction electrons, do not overlap significantly with the nuclei, and their main interaction is of dipole-dipole type which is at least one order of magnitude weaker[163] and is therefore neglected in the rest of this chapter.

The positively charged exciton state X^+ is a particularly convenient object for studying the electron-nuclear spin interactions, as it contains two paired holes in a spin singlet state $(|\Uparrow\Downarrow\rangle - |\Uparrow\Downarrow\rangle)/\sqrt{2}$ and an un-paired electron[44]. Using optical excitation the spin orientation of the electron can thus be controlled simply by means of polarised optical pumping, which will also be the method used in the following sections.

Figure 5.1 illustrates a scheme of different processes involved in dynamic nuclear polarisation experiments. The effect of a spin polarisation of the nuclear spin ensemble on an electron is usually described in terms of an effective magnetic field, the Overhauser field $B_{n,z}$, inducing a shift in electron spin energy called the Overhauser shift $\Delta E_{OHS} = g_e \mu_B B_{n,z}$. This shift can be observed on the optically recombining X^+ complex by means of spectroscopy (see section 5.3.2). The electron spin also influences the nuclei and this is often also described in terms of an effective magnetic field, the Knight field. The Knight field is limited to a few tens of mT maximum[162] while the Overhauser field, as we shall see in section 5.3.4, can reach several Tesla. Despite the differing orders of magnitudes the Knight field can play an important role both for stabilizing the nuclear spins in low magnetic fields, and conversely contribute to nuclear de-polarisation in some situations[43].

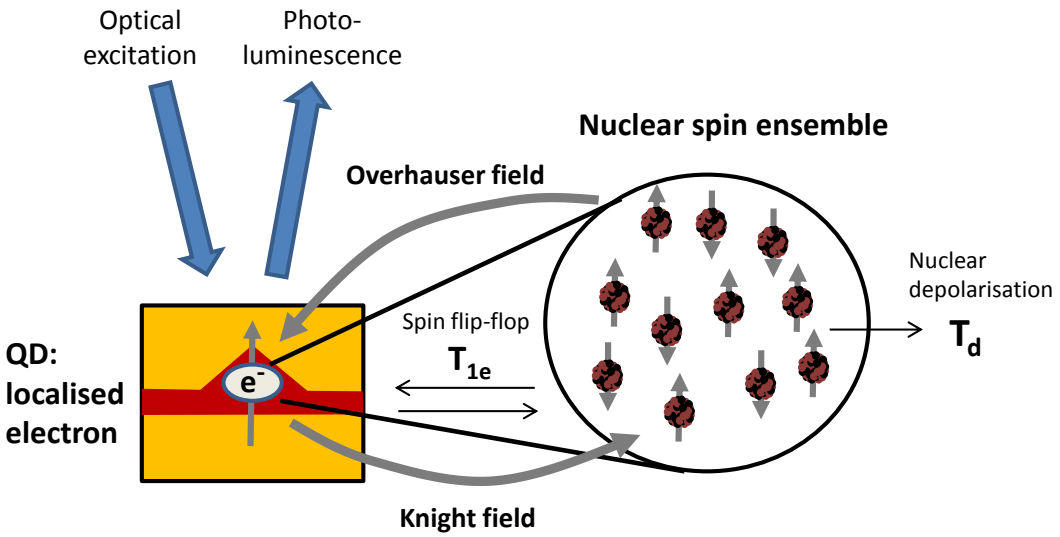

Figure 5.1: Hyperfine interactions between localised electrons and the quantum dot host nuclei in optical spin orientation experiments. Optical excitation creates a spin-polarised electron in the quantum dot that has hyperfine interactions with the nuclear ensemble. Net spin is transferred from the electron to the nuclei via "flip-flops" and can build up a nuclear spin polarisation, acting back on the electron via the Overhauser effect. Flip-flop processes occur on characteristic time scale T_{1e}. Nuclear-to-nuclear dipole interactions (spin diffusion to surrounding bulk lattice nuclei) and Knight field fluctuations contribute to nuclear depolarisation (T_d).

The hyperfine interactions permit transfer of spin from the electron to the nuclei in spin-conserving "flip-flop" processes characterised by the time scale T_{1e} as indicated in figure 5.1. T_{1e} can be estimated as[43,164]

$$T_{1e}^{-1} = \left(\frac{\tilde{A}}{N\hbar}\right)^2 \cdot \frac{2f_e\tau_c^e}{1 + (\Delta E_e \tau_c^e/\hbar)^2} \tag{5.2}$$

where f_e is the fraction of time the quantum dot is occupied by an electron, τ_c^e is the electron hyperfine correlation time and $\Delta E_e = g_e\mu_B(B_z + B_{n,z})$ is the electron spin splitting due to an external field B_z and an Overhauser field $B_{n,z}$. $\tilde{A} \approx 47$ μeV is the average Fermi-contact hyperfine constant for realistic InAs quantum dots with Ga intermixing, μ_B is the Bohr magneton and g_e the electron g-factor. The presence of ΔE_e implies a slow-down of the nuclear depolarisation rate due to electrons (T_{1e}^{-1}) in fields larger than the Knight field. Since the electron Zeeman spin splitting in a given magnetic field is ~1000 larger than the nuclear Zeeman splitting[43] electron-nuclear flip-flop processes would at first seem problematic from an energy conservation point of view. The electron correlation time τ_c^e, characterising the interaction time between the electron and nuclei, here provides an essential line broadening that makes flip-flops possible without violating energy conservation. τ_c^e is usually considerably shorter than the X^+ radiative lifetime and is most likely limited by the relaxation of the electron during the initial charge capture and formation of the X^+ state[165].

Figure 5.1 also contains an additional pathway for nuclear spin depolarisation, as indicated symbolically by an arrow away from the electron-nuclear system under consideration and characterised by the time T_d. This path represents nuclear spin depolarisation, for example by spin diffusion from the quantum dot into nuclei in the surrounding host lattice, mediated by nuclear dipole-dipole interactions. Modelling nuclear spin depolarisation is a very complex task due to the presence of strong nuclear quadrupole effects in strained InAs QDs[159]. One plausible approach is to include the gradual inhibition of nuclear spin relaxation due to quadrupolar coupling as the longitudinal field increases[166]:

$$T_d^{-1} = T_{d\infty}^{-1} + \frac{T_{d0}^{-1}}{1 + \left(B_z/B_Q\right)^2} \tag{5.3}$$

B_Q is usually in the range of hundreds of mT, which stresses the importance of quadrupolar effects at low fields. At high fields $B_z \gg B_Q$ the external field dominates the effective quadrupolar fields and the order and separation of the nuclear Zeeman levels is restored.

The dynamics of the electron-nuclear spin transfer can be modelled using a rate equation[167]:

$$\frac{d\langle \tilde{I}_z \rangle}{dt} = -\frac{1}{T_{1e}}\left(\langle \tilde{I}_z \rangle - \tilde{Q}\left(\langle \hat{S}_z \rangle - \langle \hat{S}_z \rangle_0\right)\right) - \frac{\langle \tilde{I}_z \rangle}{T_d} \tag{5.4}$$

where an average field picture is used with $\langle \tilde{I}_z \rangle = \sum \langle \hat{I}_z^i \rangle / N$ the average nuclear spin in the quantum dot (averaged over all nuclear species and all N lattice sites i).
$\tilde{Q} = \sum_i I_i(I_i+1)/(N\left(S(S+1)\right) \approx 13$ for InAs QDs. Assuming steady state it is straight-forward to derive

$$\langle \tilde{I}_z \rangle = \frac{\tilde{Q}}{1 + T_{1e}/T_d} \cdot \left(\langle \hat{S}_z \rangle - \langle \hat{S}_z \rangle_0\right) \tag{5.5}$$

Furthermore, assuming a spatial electron wavefunction of identical magnitude over all nuclear sites, one can relate the average nuclear spin $\langle \tilde{I}_z \rangle$ to the effective magnetic field $B_{n,z}$ of the nuclei acting on the electron: $B_{n,z} = 2\tilde{A}\sum \langle \hat{I}_z^i \rangle / g_e \mu_B$. Using this, equation 5.5 can be re-written as an implicit equation in $B_{n,z}$:

$$g_e \mu_B B_{n,z} = \frac{2\tilde{A}\tilde{Q}}{1 + T_{1e}(B_{n,z})/T_d} \cdot \left(\langle \hat{S}_z \rangle - \langle \hat{S}_z \rangle_0\right) \tag{5.6}$$

The average electron spin $\langle \widehat{S}_z \rangle$ refers to the average electron spin at the start of the interaction, right after the dot becomes populated. As a rough approximation we take a constant value of $\langle S_z \rangle \approx 0.8 \cdot 1/2 = 0.4$ (consistent with high degrees of electron polarisation observed in section 5.3.3). The equilibrium electron spin polarisation $\langle S_z \rangle_0 = 1/2 \cdot \tanh(g_e \mu_B B_z / k_B T)$ at 4K is negligible over the magnetic field range explored in section 5.3.4.

Equation 5.6 will have different solutions depending on the values of the system parameters and the applied magnetic field B_z. Figure 5.2(a) shows an example of the left hand side (LHS) and right hand side (RHS) for three different external field magnitudes (1T, 3T and

5T). The LHS is trivially just a line with slope unity. The RHS has a Lorentzian shape, centred around the electron Zeeman splitting $g_e \mu_B B_z$ and has a width given by $\hbar/\tau_c^e$. In general there will be three solutions to the equation, two which are stable. At 1T the solutions are degenerate, 39 μeV in the example. At 3T three solutions (4, 56, 80 μeV) are found, where the largest and smallest are the stable solutions that the system will exhibit experimentally. These correspond to different branches in a hysteretic DNP behaviour. At 5T the system has again only one solution, 1 μeV, which corresponds to a point after a sudden collapse of the OHS (for more about this see section 5.3.4).

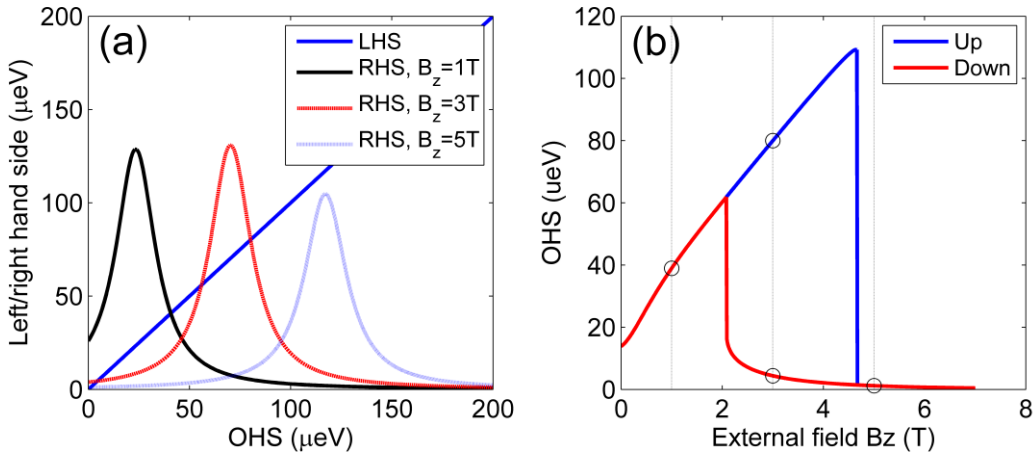

Figure 5.2: (a) Graphical representation of the left hand side (LHS) and right hand side (RHS) of equation 5.6 at three different external fields. At $B_z = 1$T and 5T only one solution exists, but for 3T three solutions exist, of which only two are stable. (b) Example solution to the implicit equation 5.6, showing the two stable solutions corresponding to sweeping external field up (blue) or down (red). Black circles mark the points corresponding to the curves in panel (a).

Bistabilities of the DNP of quantum dots under different experimental conditions varying for example excitation polarization[168,169], excitation power[165,170] and magnetic field[171] have been extensively studied and successfully modelled before using the implicit equation 5.6 above. In section 5.3.4 the above described model will be used to aid the first systematic study of the bistable nuclear spin system as a function of an applied electric field. The application of a bias voltage can have profound effects on the main characteristics of the coupled electron spin-nuclear spin system, such as electron correlation time, nuclear spin relaxation time, the Hanle effect and the electric field gradients in the structure i.e. nuclear quadrupole effects.

5.3 Experimental

5.3.1 Magneto-spectroscopy setup

Single quantum dot spectroscopy of X^+ for optical detection of dynamic nuclear polarisation presented in the following sections was carried out using a micro-photoluminescence setup (micro-PL) schematically depicted in figure 5.3 below. The configuration is of confocal type with excitation and detection coupled from and to single mode fibres in different arms. Glan-Taylor linear polarisers and voltage-controlled liquid crystal retarders allow for excitation and detection of circular, linear or arbitrary elliptical polarisation. The sample is mounted on an XYZ piezo stage in a liquid helium exchange cryostat. The stage allows for nanometre precision movements in three dimensions. This, in combination with the very high spatial resolution of the system (~1 μm) owing to the small effective apertures of the excitation and detection single mode fibres (SMF), allows single quantum dots to be optically addressed. High-resolution spectroscopy is performed using a monochromator coupled to a low noise silicon CCD.

A superconducting magnet allows for fields up to 9T to be applied in z-direction, coinciding with the sample growth direction in Faraday geometry (section 5.3.4). For Voigt geometry experiments (section 5.3.5) the sample is mounted vertically using a custom made holder, allowing the applied field to be applied transversely, or in-plane, relative to the sample growth direction. An additional mirror makes optical access to the single quantum dots possible also in this geometry.

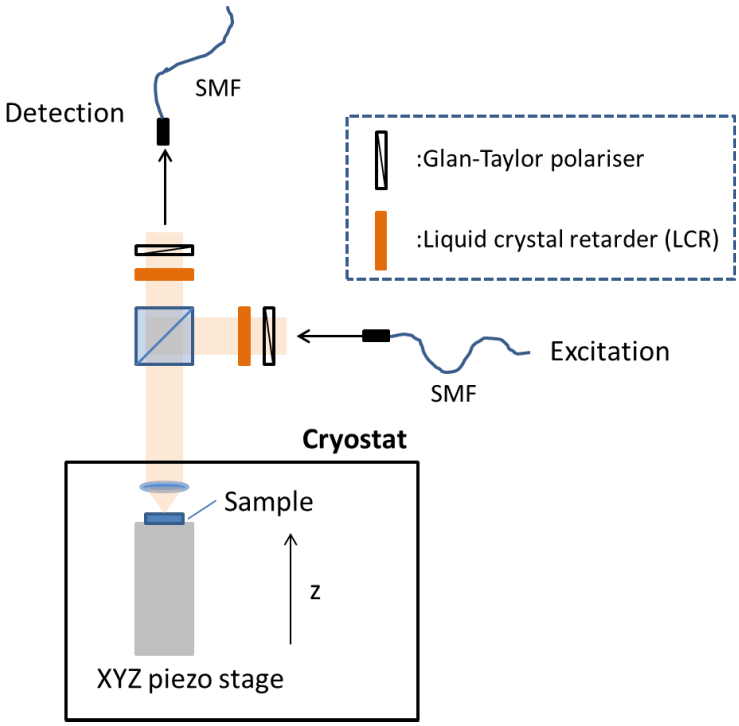

Figure 5.3: Micro-PL setup for single quantum dot magneto-spectroscopy in Faraday geometry. A combination of Glan-Taylor linear polarisers and voltage controlled liquid crystal retarders (LCR) allows for excitation and detection of arbitrary polarisations.

5.3.2 Optical detection of nuclear polarisation

Figure 5.4 shows the optical transitions of the positively charged trion X^+ and associated spin configurations in the presence of an external longitudinal field B_z and an effective nuclear magnetic (Overhauser) field $B_{n,z}$. In the X^+ state two heavy holes are present and in the lowest orbital states they occupy anti-parallel spin states (+3/2 ⇑ and -3/2 ⇓). After recombination a single hole is left in the dot, with Zeeman energy only determined by the external field as the hyperfine interaction of holes is one order of magnitude weaker[160] than for the electron and therefore neglected, as explained before. Conservation of angular momentum determines which transitions are optically active: the un-paired electron +1/2 (↑) can recombine with a -3/2 hole (⇓), i.e. the electron makes a transition to a valence state with angular momentum 3/2. The increased angular momentum $\hbar$ of the electron is balanced by the emission of a σ^- polarised photon carrying angular momentum $-\hbar$. Similar rules apply to the trion with a spin-down (↓) electron.

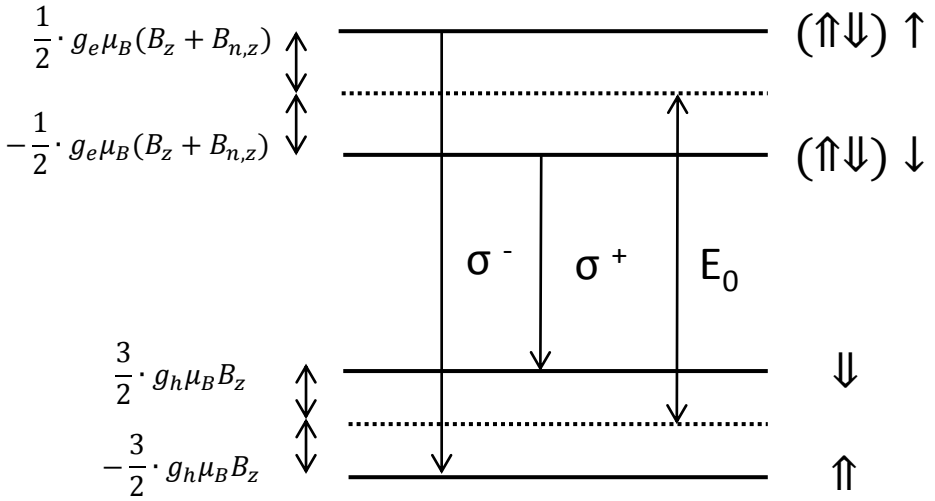

Figure 5.4: Zeeman splitting of X⁺ transition lines. Optically active transitions with circular polarisation are shown.

From the diagram in figure 5.4 we see that the energies of the transitions are given by the initial state of the electron and the final state of the hole:

$$\mathrm{E}(\sigma^{\pm}) = E_0 \mp \frac{1}{2} g_e \mu_B \left(B_z + B_{n,z}\right) \mp \frac{3}{2} g_h \mu_B B_z \tag{5.7}$$

which gives a total energy splitting of the lines

$$\Delta\mathrm{E} = g_e \mu_B \left(B_z + B_{n,z}\right) + 3 g_h \mu_B B_z = \Delta Z + \Delta E_{OHS} \tag{5.8}$$

where $\Delta Z = g_e \mu_B B_z + 3 g_h \mu_B B_z$ is the Zeeman splitting in absence of an effective nuclear magnetic field, and $\Delta E_{OHS} = g_e \mu_B B_{n,z}$ is the Overhauser shift.

Figure 5.5 shows an example PL-spectrum measured at $B_z = 6$ T showing a clear and large Zeeman splitting ΔZ of the X^+ transition of a quantum dot. Linearly polarised excitation was used to ensure no initial spin polarisation of the charge carriers to avoid nuclear polarisation effects. By carefully measuring the σ^+- σ^- splitting ΔE with *circularly* polarised excitation and knowing ΔZ the OHS (ΔE_{OHS}) resulting from electron-nuclear spin transfer can be separated from equation 5.8 above. Due to the inherently narrow-band emission of single quantum dots, OHS down to a few μeV, well below the linewidth of the spectroscopy system, can be detected by fitting the measured transition line with Gaussian lineshapes. Figure 5.6 illustrates an example of such lineshape analysis, detecting an OHS ~8 μeV induced by optical spin-pumping of the nuclei in the absence of external magnetic field.

In the following sections, we perform micro-photoluminescence (PL) experiments in zero external magnetic field, with an external magnetic field parallel (Faraday geometry) and transverse (Voigt geometry) to the sample growth direction. Through careful analysis of recorded spectra as outlined here the electron interaction with the mesoscopic nuclear spin ensemble in single quantum dots is studied.

Figure 5.5: Zeeman splitting of X^+ transition in an external field $B_z = 6$T. Linearly polarised excitation was used.

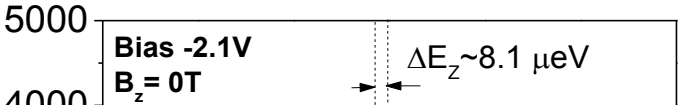

Figure 5.6: Detection of small energy shifts by line fitting. σ^+ circularly polarised excitation induces ~8 μeV Overhauser shift detected by recording σ^+/ σ^-- polarised spectra.

5.3.3 Optical pumping of nuclear spin polarisation in a charge tuneable device

Our sample contains self-assembled InAs quantum dots (QD) embedded in a GaAs diode structure. The design, schematically depicted in figure 5.7, includes thick AlGaAs barriers to allow for wide range electric field tuning while avoiding the tunnelling out of photo-generated carriers. Such designs have previously been used to tune the energy of different exciton complexes[172], to observe the coherent coupling between neutral exciton states[50] and to control the electron- and hole g-factors[173]. Distributed Bragg reflectors placed outside the tunnelling barriers create a weak optical cavity, enhancing the light collection efficiency around the emission wavelengths of the quantum dots (~940 nm). The sample is operated with an applied d.c. bias at ~4K in the photoluminescence spectroscopy setup depicted in figure 5.3 above.

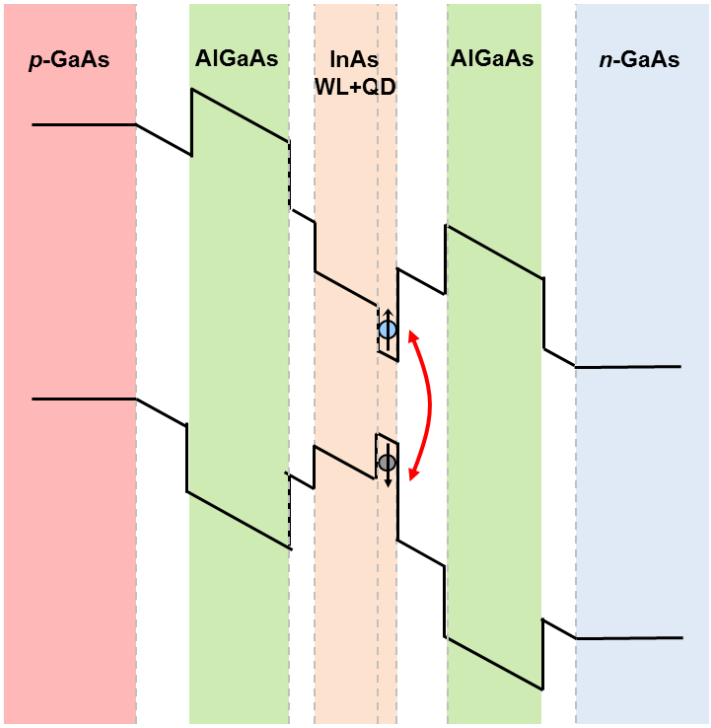

Figure 5.7: Schematic band diagram of the charge-tuneable QD diode structure. Thick AlGaAs barriers (green) inhibit the tunnelling of photo-generated charge carriers out of the quantum dot. White regions indicate nominally intrinsic (un-doped) GaAs. Charge carriers are excited in the low-energy tail of the wetting layer and subsequently relax into the quantum dot ground states.

We take advantage of the wide tuning range of the devices to study the effect of varying electric field on dynamic nuclear polarisation (DNP) effects in single quantum dots. We use circularly polarised light from a tuneable CW Ti-Sa laser to create a spin-polarised electron population in the wetting layer. The holes on the other hand quickly lose their polarisation in the wetting layer[43], which means that the formation of the hole singlet state of the X^+ is uninhibited, while the unpaired electron spin is largely determined by the pump laser. To achieve the highest possible nuclear spin polarisation we operate the laser at ~850 and ~860 nm, which corresponds to the low energy tail of the quantum dot wetting layer and minimises excitation of light holes[174].

The large electric field tuning range of the device used here is illustrated in figure 5.8(a), which shows photoluminescence from a quantum dot as a function of applied voltage. The X^+ transition can be seen over a range of more than 4V beginning at about approximately -4.5V. Around -1.3V the electron tunnelling rate out of the dot has been sufficiently suppressed to permit the existence of neutral exciton ($X0$) and biexciton ($XX0$) complexes and at ~0V the negative trion (X^-) appears. From this point and through the rest of this chapter we devote our attention to the X^+state only, since it has been shown that its presences allows for achieving high degrees of DNP [43].

We start to probe the nuclear spin system in zero external magnetic field by exciting the charge carriers with circularly polarised light. As discussed in section 5.2 the mean electron spin is partially transferred to the nuclear spin system and results in the build-up of an effective nuclear magnetic field $B_{n,z}$ that will in turn act on the electron. The Overhauser shift (OHS), $\Delta E_{OHS} = g_e \mu_B B_{n,z}$ is here, in absence of external magnetic field ($\Delta Z = 0$), directly detected as the difference between σ^- and σ^+-polarised PL spectra as described by equation 5.8. While comparing the σ^+ and σ^- transition energies allows us to calculate the OHS and gain insight into the nuclear spin environment, comparing the PL *intensities* gives insight into the environment experienced by electrons localised in the quantum dot through the degree of circular polarisation $\rho_c = (I_{\sigma+} - I_{\sigma-})/(I_{\sigma+} + I_{\sigma-})$, where $I_{\sigma\pm}$ is taken as the area of the fitted lineshapes. The degree of circular polarisation is directly related to the electron spin polarisation averaged over the spin lifetime; $\rho_c = -2\langle S_z \rangle = -2/\tau_r \int_0^\infty \langle S_z(t) \rangle \exp(-t/\tau_r) dt$. The resulting OHS together with the degree of circular polarisation is shown in figure 5.8(b) for the X^+ transition. Around -2V, roughly in the middle of the range where X^+ exists, an OHS of ~8 μeV and a high degree of PL circular polarisation (~60%) is achieved. Here, the DNP helps to stabilise the electron spin against the fluctuating effective magnetic field from the nuclei in the QD[174]. Towards the ends of the range the OHS and the circular polarisation both drop, as the conditions for spin transfer to the nuclei become less favourable, and charge carriers begin to tunnel in and out of the dot and consequently lose their spin polarisation.

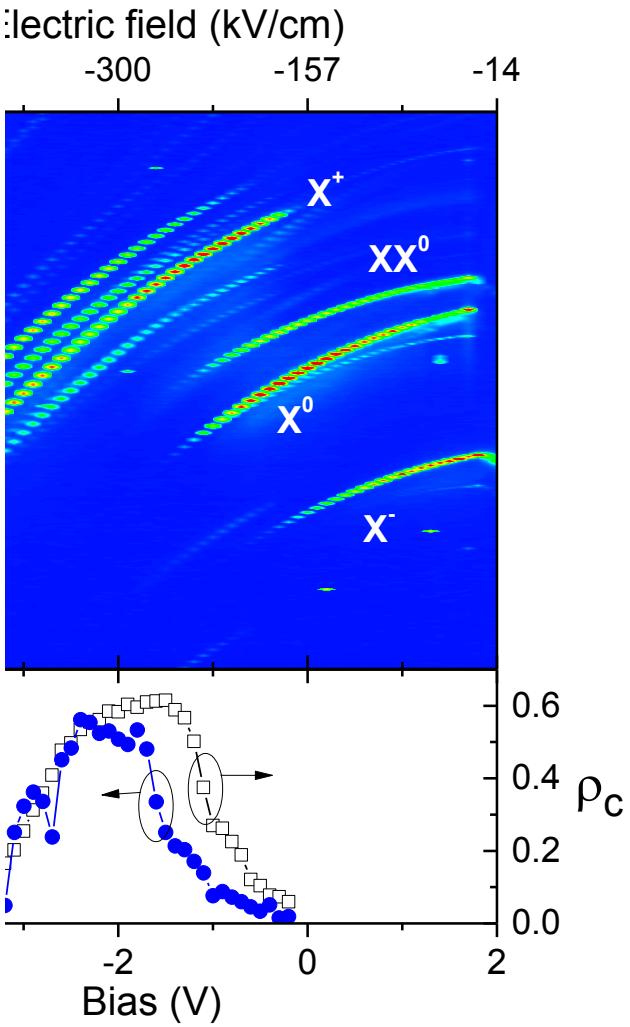

Figure 5.8: (a) Bias-dependent PL spectra in zero external magnetic field, showing identified exciton complexes. (b) Overhauser shift (OHS, blue circles) and degree of circular polarisation (ρ_c) as a function of applied bias voltage.

5.3.4 Dynamic nuclear polarisation in longitudinal magnetic field

The results presented in figure 5.8 on their own strongly indicate that we can control the electron-nuclear interaction by changing the bias voltage, but they do not allow us to deduce any of the parameters characterising the interaction. To study the voltage dependence further, we perform DNP measurements in applied longitudinal magnetic fields B_z at different applied voltages. For each voltage B_z is swept first from zero to a maximum of 6T, and back down to zero, all the time exciting spin-polarised electrons with a σ^+-polarised laser and recording the PL-spectra.

As a first example let us consider measurements at a constant bias of -2.0V: Figure 5.9 shows the detected energy splitting of the circularly polarised X^+ lines for linear excitation (red) and σ^+-excitation (black). For both linear and circular excitation the energy splitting first increases linearly with B_z, crucially however with different slopes. At a critical field $B_{z,c1}$ a discontinuous jump can be seen for the circularly excited case, after which the two curves overlap. The deviation for $B_z < B_{z,c1}$ can be explained by the existence of an Overhauser shift ΔE_{OHS} experienced by the electron.

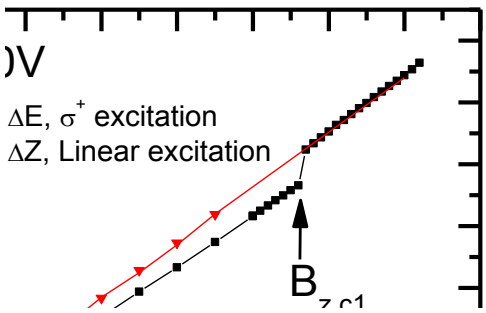

Figure 5.9: X^+ Zeeman splitting as a function of applied magnetic field for constant bias -2.0V. A discontinuous jump occurs at $B_{z,c1} = 4.6$ T.

The difference between the two curves in figure 5.9 gives the OHS (in accordance with equation 5.8):

$$\Delta E_{OHS} = g_e \mu_B B_{n,z} = \Delta E - \Delta Z \qquad (5.9)$$

The energy shift with circular excitation in figure 5.9 is smaller than with linearly polarised excitation, i.e. $\Delta E_{OHS} < 0$, which indicates that the nuclear spins align to build up an effective magnetic field $B_{n,z}$ *opposite* to the external field B_z. The helicity of the exciation relative to the external field direction is important[166]; with σ^- no discontinuity is observed, i.e. $\Delta E_{OHS} \sim 0$ telling us that the nuclear spin system does not polarise to an appreciable degree when the pumping would correspond to an effective nuclear field $B_{n,z}$ aligned parallel to B_z.

Figure 5.10(a) shows the measured OHS at constant bias -2.0V, deduced from data in figure 5.9 according to eq. 5.9. As the external field is ramped up the OHS increases and compensates the electron Zeeman energy, keeping the total electron spin splitting $\Delta E_e = g_e\mu_B(B_z + B_{n,z})$ small, which ensures that electron-nuclear flip-flops and further build-up of nuclear spin polarisation remains possible. At the critical field $B_{z,c1} = 4.6$ T the nuclear polarisation reaches saturation; any increase in external field B_z from this point increases the electron spin splitting, rapidly making the flip-flop processes energetically difficult. Here, the system is unable to maintain nuclear polarisation and through negative feedback via the electron Zeeman energy a drastic collapse of OHS occurs, coinciding with the discontinuity in figure 5.9. As the external field is swept back down and the electron Zeeman splitting ΔE_e gradually decreases an OHS around zero is observed, until a critical field $B_{z,c2} = 2$ T where the Zeeman energy is small enough for flip-flops to take place and the OHS recovers rapidly, this time through positive feedback via ΔE_e. Clearly the system possesses a memory effect; the reaction to a change in magnetic field depends strongly on the history of the system.

Figure 5.10 (b) shows the degree of circular polarisation ρ_c of X^+ measured simultaneously with the OHS. The dip just before $B_{z,c1}$ can be qualitatively explained by considering that as we approach the critical field the electron spin splitting ΔE_e is decreasing which (i) leads to an increased flip-flop rate as the system tries to maintain $B_{n,z} = -B_z$ and (ii) removes the stabilising effect of large ΔE_e against nuclear fluctuations δB_n[175]. Both effects lead to reduced observed electron spin polarisation.

At two different bias voltages, -1.1V and -2.8V, we observe qualitatively similar OHS bistabilities as illustrated in figure 5.10(c-f). The critical fields, however, are lower than at -2.0V as summarised in figure 5.11(a), reflecting that the DNP conditions change with bias. To shed more light on the parameters governing the system we use the implicit equation 5.6 for $B_{n,z}$ presented in section 5.2, repeated here for convenience:

$$g_e\mu_B B_{n,z} = \frac{2\tilde{A}\tilde{Q}}{1 + T_{1e}(B_{n,z})/T_d} \cdot \left(\langle\hat{S}_z\rangle - \langle\hat{S}_z\rangle_0\right) \tag{5.6}$$

The longitudinal electron g-factor g_e can be accurately determined from experimental data at the critical field $B_{z,c1}$ by considering that there $\Delta E_e = g_e\mu_B\left(B_{z,c1} + B_{n,z}\right) = 0$, i.e. $\left|g_e\mu_B B_{z,c1}\right| = |\Delta E_{OHS}|$[166,176]. For the quantum dot studied here we find a slight variation of ~10% in g_e with voltage, see figure 5.10 panels (a), (c) and (e).

By solving equation 5.6 we can model the observed OHS and extract parameters characterising the electron-nuclei spin interaction. We find that the most sensitive parameters are the electron correlation time τ_c^e and the nuclear depolarisation time $T_{d\infty}$, determined primarily by the critical fields $B_{z,c1}$ and $B_{z,c2}$, and we fit these manually. Table 5.1 below summarises all parameters going into equation 5.6. Figures 5.10(a,c,e) include the resulting fits to the OHS (courtesy of L. Bouet and B. Urbaszek), which show good qualitative agreement. Figure 5.11(b) summarises the fitted parameters as a function of applied bias voltage. At -2.0V, where the largest OHS can be built up, we find a minimum for τ_c^e and a maximum for $T_{d\infty}$. Away from -2.0V τ_c^e increases while $T_{d\infty}$ decreases. Such reciprocal behaviour of τ_c^e and $T_{d\infty}$ has been observed before[168] and that $T_{d\infty}$ depends on τ_c^e can be expected; long spin memory times are observed for unpopulated quantum dots[177], i.e. de-polarisation is linked to the presence of an electron, characterised by τ_c^e. The depolarisation mechanism could be direct through Knight field fluctuations, or indirect through local modification of the electric field gradients, i.e. the nuclear quadrupole effects, when an electron is present.

Parameter	Description	Value
g_e	Electron g-factor (experimentally determined)	-0.404 to -0.43
$\tilde{A}$	Average hyperfine constant	47 μeV
$\tilde{Q}$	$\tilde{Q} = \sum_i I_i(I_i+1)/(N(S(S+1))$	13
N	Number of nuclei in confined electron wavefunction.	$6 \cdot 10^4$
$\langle \hat{S}_z \rangle$	Average electron spin z-component directly after initialisation of electron spin	$0.8 \cdot \frac{1}{2} = 0.4$
B_Q	Phenomenological parameter, representing strength of quadrupolar effects	0.4 T
T_{d0}	Nuclear depolarisation time in zero field	500 μs
$T_{d\infty}$	Nuclear depolarisation time in high field	Fitting parameter
τ_c^e	Electron hyperfine interaction correlation time	Fitting parameter

Table 5.1: Summary of parameters used in OHS fitting.

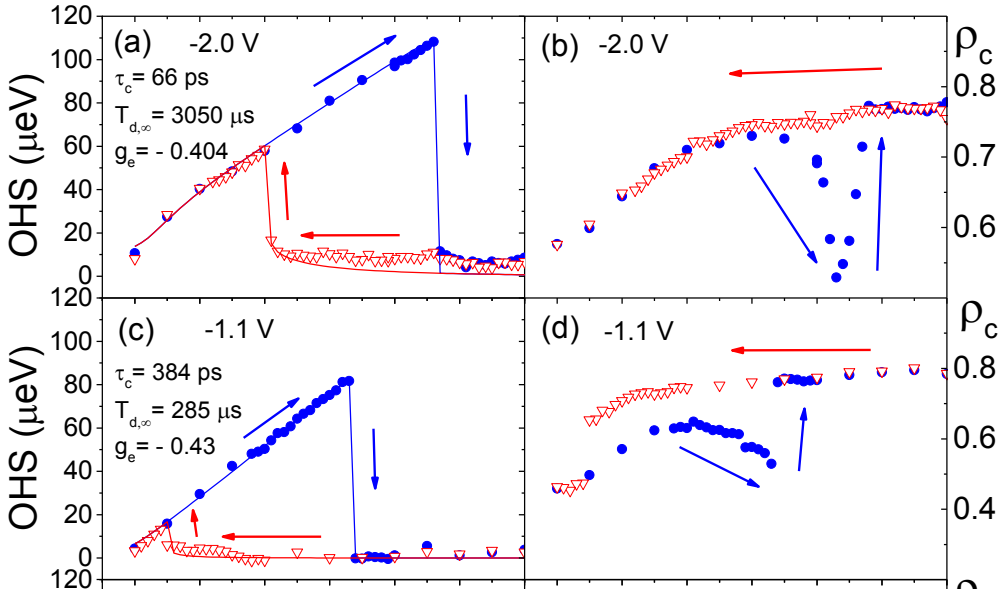

Figure 5.10: Overhauser shift (OHS) bistabilities and associated degree of circular polarisation (ρ_c) in magnetic field sweeps at three different bias voltages.
(a)-(b): at -1.1V (c)-(d) at -2.0V and (e)-(f) at -2.8 V. Blue filled circles are experimental results sweeping field B_z up, red triangles when sweeping B_z down. Solid lines are fitted curves (courtesy of L. Bouet and B. Urbaszek), using parameters τ_c and $T_{d,\infty}$ as free parameters. Electron g-factors g_e were experimentally determined.

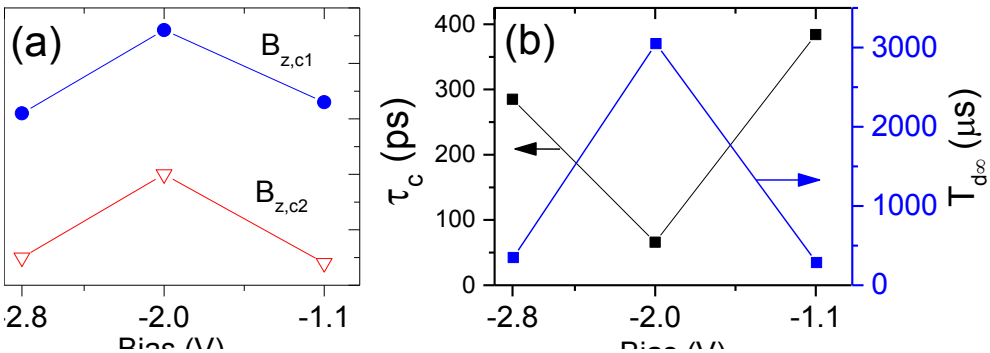

Figure 5.11: (a) Experimentally determined critical field sweeping magnetic field up ($B_{z,c1}$) and down ($B_{z,c2}$) for different applied bias. (b) System parameters fitted using bistability curves in figure 5.10, electron hyperfine correlation time τ_c and nuclear depolarisation time $T_{d\infty}$.

A very direct way to probe the voltage control over DNP effects, enabled by the wide tuning range of our device, is to scan the bias while pumping the quantum dot with polarised electrons, and observe how the OHS changes during the bias scan[178]. The measurements start in zero magnetic field and we slowly increase the field strength until the desired magnitude B_z is reached, all the time exciting the carriers with σ^+-polarised light and keeping the bias at -2.0V, the most favourable point for DNP. Then we sweep the applied voltage from -2.0V to -0.5V near the end of the range of existence of X^+ and back again, while recording PL spectra for determination of OHS and circular polarisation. Based on the zero-field experiments (figure 5.8) and the magnetic field sweep bistabilities (figure 5.10) we can expect that as we change the bias voltage away from -2.0V we change τ_c^e and $T_{d\infty}$, i.e. the conditions for DNP. Figures 5.12 show the results for $B_z = 1.5$ T (panels a, b) and $B_z = 3$ T (panels c, d) respectively. Comparing with figure 5.10(a) (bias constant at -2.0V) we can note that $B_z < B_{z,c1}$ for both of our chosen magnetic field strengths. For $B_z = 1.5$ T (figure 5.12 (a)) we see a collapse of the OHS near -1.0V, accompanied again by a drop in circular polarisation (figure 5.12(b)) as $\Delta E_e \to 0$. When sweeping the voltage back towards -2.0V a revival of the OHS is observed at -1.7V when the electron hyperfine correlation time τ_c^e becomes shorter again (see figure 5.11(b)).

For $B_z = 3$ T we see a similarly sudden collapse of the OHS, but no recovery. This is not surprising, as comparing again with figure 5.10 (c) we can see that even at the optimal conditions (-2.0V) the recovery happens first at ~2 T. The Zeeman splitting at 3T is simply too large for flip-flops to take place to any considerable degree, and the positive feedback mechanism associated with a revival never kicks in.

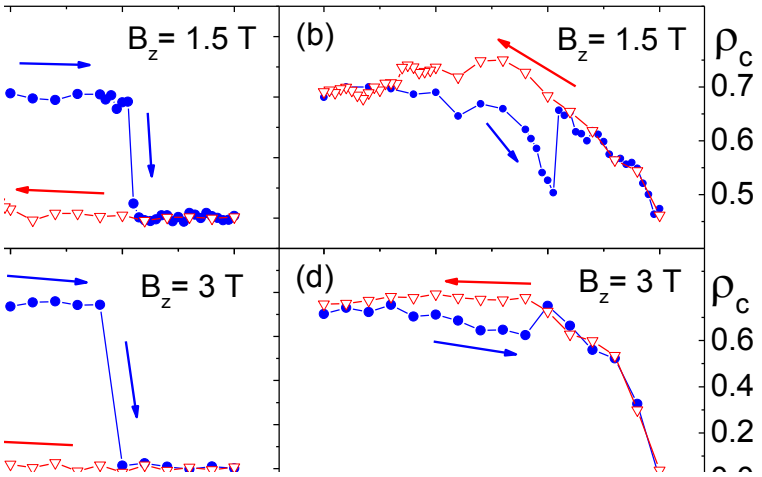

Figure 5.12: Dynamic nuclear polarisation in bias scans. (a) OHS exhibiting bistability in bias scan at constant magnetic field $B_z = 1.5$ T (b) associated degree of circular polarisation. (c) OHS during bias scan at $B_z = 3$ T *not* exhibiting bistable behaviour. (d) associated degree of circular polarisation.

To conclude the measurements in Faraday geometry, we have been able to control the width of the DNP bistability in magnetic field sweeps, achieving internal effective nuclear magnetic fields of several Tesla. Furthermore, we could observe bistable behaviour directly as a function of applied voltage. Our modelling of the OHS shows good qualitative and quantitative agreement, suggesting that the dynamics of the electron-nuclei interactions are primarily governed by the hyperfine correlation time τ_c^e and the nuclear depolarisation time $T_{d\infty}$, that they are mutually dependent and that they can be controlled by an applied voltage.

5.3.5 Electron depolarisation experiments in transverse magnetic field

An electron spin aligned along the longitudinal/growth axis (z), subject to a transverse magnetic field B_x is expected to precess around the magnetic field axis with the Larmor frequency $\Omega = |g_{e,x}\mu_B B_x|$. Averaged over the spin lifetime τ_s^* the observed degree of circular polarisation, directly related to the average electron spin, is expected to have a standard Hanle depolarisation curve with Lorentzian magnetic field dependence $\rho_c = \rho_c(0)/(1 + B_x^2/B_{1/2}^2)$ with HWHM $B_{1/2} = \hbar/|g_{e,x}|\mu_B\tau_s^*$ [155]. For single InP/InGaP[179] and InAs/GaAs[161] quantum dots radical departures from this scenario have been observed, with significantly broadened depolarisation curves and strikingly non-linear, hysteretic behaviour.

Here, we perform Hanle depolarisation measurements in transverse magnetic field on the same quantum dot as was used in previous sections, complementing the observations in longitudinal field. The X^+ PL polarization once again provides the means to observe the electron depolarisation. Experiments are started in absence of external magnetic field, and the quantum dot is non-resonantly excited in the wetting layer by a circularly polarised (σ^-) cw laser. The magnetic field B_x is gradually increased and the effect on electron polarisation is observed via the σ^+/σ^--polarised X^+ PL.

Figure 5.13(a) shows the measured de-polarisation curve at bias -1.7V where the electron polarisation is maximised (figure 5.8(b)). The initial polarisation at $B_x = 0$ is 60% and remains almost constant up to 0.2T, after which it gradually drops to ~35% at ~0.5T. For $0.5\text{T} < B_x < 0.9\text{T}$ the polarisation drops slower again, but collapses suddenly at 0.95T. After this point the electron polarisation is completely lost. Without interrupting the experiment, the magnetic field is ramped down, and a sudden revival of circular polarisation is observed at 0.8T, after which the system more or less follows the previously observed curve. Figure 5.13(a) also shows a Lorentzian depolarisation curve assuming a 1 ns electron spin lifetime, which illustrates the drastic departure of our experimental observations from the standard Hanle effect. The highly nonlinear, hysteretic behaviour observed here is in line with previous work on InAs/GaAs single QDs[161].

The anomalous Hanle effect in transverse fields has been explained in terms of dynamic nuclear polarisation, but with the remarkable difference that electron spins with initial alignment along the longitudinal axis (z) are now transferring spin to the nuclei to build up a *transverse* effective nuclear field[161] $B_{n,x}$, in contrast to Faraday geometry where a longitudinal Overhauser field resulted. Supporting this interpretation is the fact that we do not observe any significant OHS between the detected σ^+/σ^--PL. The effect of $B_{n,x}$ is to cancel the external field B_x, so that the electron spin splitting remains small and spin transfer to nuclei can continue to take place, similar to the Faraday geometry measurements. A microscopic theory exactly *how* the spin transfer occurs is still lacking though.

Figure 5.13: Electron depolarisation experiments in transverse magnetic field B_x. (a) Circular polarisation at constant bias -1.7V exhibiting clearly anomalous Hanle effect and a bistable region when sweeping field up (blue circles) and down (red triangles). A Lorentzian for an assumed electron spin lifetime of 1 ns highlights the difference to standard Hanle curves. (b) Circular polarisation measured at -1.4V (open green squares) and -1.1V (open magenta diamonds) with circular excitation, and at -1.7V with elliptical polarisation (solid green squares, solid magenta diamonds). The black solid line shows a Lorentzian fit to the -1.1V depolarisation curve.

Inspired by the observations in Faraday geometry, where the electron spin correlation time and nuclear depolarisation time could be voltage controlled in our charge-tuneable device, more depolarisation measurements were performed at -1.4V and -1.1V, see figure 5.13(b). For both -1.4V and -1.1V the initial electron polarisation is lower (46% and 25% respectively), as expected based on previous zero-field measurements in figure 5.8(b). The depolarisation curve at -1.4V is still broadened, but no abrupt collapse is observed. At -1.1V the curve fits rather well to a Lorentzian curve, allowing us to extract a spin lifetime $\tau_s^* \approx 490$ ps (the electron g-factor was determined to be 0.181 in separate measurements), a reasonable value only slightly shorter than typical radiative lifetimes.

To rule out that the different behaviour at different bias voltages is solely down to the different initial polarisations $\rho_c(0)$, we operate the device at -1.7V and adjust the excitation to be elliptical using the liquid crystal retarders, achieving exactly the same initial polarisations as for -1.4V and -1.1V with fully circularly polarised excitation. The results are shown in figure 5.13(b). The curves are clearly broader than the ones done at -1.4V and -1.1V, and we can conclude that the changing behaviour with bias is not mainly determined by initial polarisation. We can also conclude that by controlling the bias, we can tune the electron-nuclear system from the anomalous to the standard Hanle regime. Based on the measurements in Faraday geometry a reasonable hypothesis is that the electron correlation time τ_c^e plays a key role also in the anomalous Hanle effect.

5.4 Conclusions

The intricate coupling between a single carrier spin and the mesoscopic nuclear spin system gives rise to strong internal effective fields, up to several Tesla, and highly non-linear effects, as demonstrated by bistable OHS in Faraday geometry (figures 5.10, 5.12) and in electron depolarisation experiments in Voigt geometry (figure 5.13). In Faraday geometry the measurements showed that the electron correlation time τ_c^e could be controlled, and that the nuclear spin relaxation time $T_{d\infty}$ was co-dependent. This hints at Knight field fluctuations (obviously directly dependent on the presence of an electron) playing an important role in nuclear relaxation. Furthermore the voltage control of τ_c^e and $T_{d\infty}$ allowed us to observe DNP hysteresis directly as a function of applied bias over a much wider range than has been previously possible[178].

In Voigt geometry the anomalous Hanle effect was observed, with drastically broadened depolarisation curves and strongly non-linear and hysteretic behaviour. In contrast to previous reports on anomalous Hanle effect in InAs QDs[161] non-resonant excitation in the wetting layer was used, showing that the effect only relies on the initial creation of spin-polarised electrons. It was also demonstrated that by changing bias voltage the system could be tuned from the anomalous to the standard Hanle regime. In light of the bias dependence of τ_c^e seen in Faraday DNP experiments, it is likely that the electron correlation time τ_c^e playing a key role also for the anomalous Hanle effect.

6 Conclusions and outlook

The need for improved single photon and entangled-pair sources to replace the SPDC sources conventionally used in optical quantum information science has been emphasized at several points in this thesis. Semiconductor quantum dots offer an interesting alternative base upon which a quantum light source technology could be built, with many degrees of freedom for the "quantum engineer" to explore, optimise and adapt according to application. Electrically driven entangled light sources based on quantum dots are from an application point of view particularly attractive: semiconductor technology offers the possibility of miniaturisation and integration, and purely electrical operation would reduce the overall complexity by getting rid of the driving laser systems.

In chapter 2 an entangled-light-emitting diode (ELED) based on self-assembled InAs quantum dots was employed in two-photon-interference experiments. In contrast to previous work on quantum dots which has focussed mainly on emission from charged excitons, the interfering photons here were part of entangled photon pairs, with entanglement fidelities up to 0.87 ± 0.04. Post-selective two-photon interference visibility of up to 0.60 ± 0.05 was measured, showing that a majority of the photons detected simultaneously did indeed interfere.

Encouraged by the two-photon interference result the first teleportation setup utilising electrically generated entangled light was implemented (chapter 3). Six states symmetrically distributed over the Poincaré sphere (H, V, D, A, R, L) were teleported with an average fidelity of 0.704 ± 0.016. Since the classical limit for the chosen set of states is 2/3, we could conclude that quantum teleportation did indeed take place.

Recognizing that applications are likely to require teleportation of photons from a source different to the ELED, the teleportation setup was modified to accommodate a CW laser, as presented in chapter 4. As a stepping stone towards teleportation, it was verified that the two-photon interference between the dissimilar sources worked, and in addition this allowed us to observe quantum beats on a timescale of ~100 ps when detuning the laser from the quantum dot generated photons. This is to the best of our knowledge the first observation of such beats for quantum dots, previously only reported for very long photon wavepackets originating from atomic transitions. Proceeding to teleportation experiments, it was found that the highly coherent laser photons reduces the overall sensitivity of the quantum teleportation process to dephasing events in the quantum dot, and the average teleportation fidelity for six states increased to 0.76 ± 0.012. Single-qubit tomography revealed that the fine-structure splitting (FSS) of the quantum dot exciton state is carried through to an evolution of the teleported state, which highlights the importance of containing the FSS problem.

Controlling nano-scale systems such as quantum dots requires a deep understanding of the material physics, exemplified by the fact that even effects on the hyperfine level influence entangled light generation. Thus research efforts into QD material science are strongly motivated by applications. The hyperfine interaction of a confined electron spin with the mesoscopic nuclear host lattice was explored in collaboration with INSA-Toulouse, France. The main result, presented in chapter 5, is demonstration of voltage control of nuclear spin polarisation dynamics in a charge-tuneable structure, which was attributed to bias control of the electron spin correlation time and the nuclear depolarisation time. Furthermore, the anomalous Hanle effect, previously only observed with quasi-resonant excitation for InAs QDs, was observed under non-resonant conditions, and could be voltage tuned into the normal Hanle regime.

Better quantum light sources will result from development on two fronts: (i) improved quantum dot quality, e.g. reducing sources of photon decoherence such as charge fluctuations in nearby traps and wetting layer, and (ii) improved device designs, e.g. using optical cavity effects for Purcell enhanced emission, potentially reducing the problem with exciton fine-structure while improving source efficiency. Electrically driven devices, such as the ELED, need to have faster electrical response for high quality pulsed operation. This was only briefly explored in section 2.2.2, but the limited study illustrates the challenge. Faster devices could be achieved by reducing the device area (capacitance) and identifying resistive elements. It is also possible that more advanced resonant tunnelling approaches such as Benson et al.'s original proposal[56] could prove fruitful.

Quantum dot based light sources have been shown to be in possession of many of the qualities sought after in optical quantum information processing; low multiple photon emission probability, high purity (coherence)[32,108], high efficiency[70] and, as demonstrated in this thesis, compatibility with electrical operation without external lasers and the ability to generate entangled light. These properties make quantum dots one of the prime candidates to realise the quantum light sources for the future. It is a grand challenge for the future to improve and unify several of these properties in one light source, but great progress has been made in recent years. Parallel to being application-driven, optical quantum information offers the researcher a window into the fascinating and often counter-intuitive quantum physical world. The great potential promised by quantum technology combined with the bringing together of different disciplines such as semiconductor physics, information science and quantum mechanics (and for those so inclined, even philosophy[180]) is very stimulating for the researcher. Without doubt this will continue to inspire and motivate great research efforts into semiconductor based quantum light emitters in the coming years.

7 Bibliography

1. Einstein, A., Podolsky, B. & Rosen, N. Can quantum-mechanical description of physical reality be considered complete? *Physical Review* **47,** 777–780 (1935).

2. Bohr, N. Can quantum-mechanical description of physical reality be considered complete. *Physical Review* **48,** 696–702 (1935).

3. Schrödinger, E. Die gegenwärtige situation in der quantenmechanik. *Naturwissenschaften* **23,** 807–812, 823–828, 844–849 (1935).

4. Wiseman, H. M. From Einstein's theorem to Bell's theorem: a history of quantum non-locality. *Contemporary Physics* **47,** 79–88 (2006).

5. Zeilinger, A. Quantum entanglement: A fundamental concept finding its applications. *Physica Scripta* **T76,** 203–209 (1998).

6. Schrödinger, E. The present situation in quantum mechanics. *Proceedings of the American Philosophical Society* **124,** 323–338 (1980).

7. Bell, J. S. On the Einstein Podolsky Rosen Paradox. *Physics* **1,** 195–200 (1964).

8. Clauser, J., Horne, M., Shimony, A. & Holt, R. Proposed Experiment to Test Local Hidden-Variable Theories. *Physical Review Letters* **23,** 880–884 (1969).

9. Aspect, A., Grangier, P. & Roger, G. Experimental Tests of Realistic Local Theories via Bell's Theorem. *Physical Review Letters* **47,** 460–463 (1981).

10. Aspect, A., Grangier, P. & Roger, G. Experimental Realization of Einstein-Podolsky-Rosen-Bohm Gedankenexperiment: A New Violation of Bell's Inequalities. *Physical Review Letters* **49,** 91–94 (1982).

11. Scheidl, T. *et al.* Violation of local realism with freedom of choice. *Proceedings of the National Academy of Sciences of the United States of America* **107,** 19708 (2010).

12. Giustina, M. *et al.* Bell violation using entangled photons without the fair-sampling assumption. *Nature* **497,** 227–230 (2013).

13. Bennett, C. H. *et al.* Teleporting an unknown quantum state via dual classical and Einstein-Podolsky-Rosen channels. *Physical Review Letters* **70,** 1895–1899 (1993).

14. Bouwmeester, D. *et al.* Experimental quantum teleportation. *Nature* **390,** 575–579 (1997).

15. Yao, X.-C. *et al.* Observation of eight-photon entanglement. *Nature Photonics* **6,** 225–228 (2012).

16. Ritter, S. *et al.* An elementary quantum network of single atoms in optical cavities. *Nature* **484,** 195–200 (2012).

17. Monz, T. *et al.* 14-Qubit Entanglement: Creation and Coherence. *Physical Review Letters* **106,** 130506 (2011).

18. Bernien, H. *et al.* Heralded entanglement between solid-state qubits separated by three metres. *Nature* **497,** 86–90 (2013).

19. Rossetti, R., Nakahara, S. & Brus, L. E. Quantum size effects in the redox potentials, resonance Raman spectra, and electronic spectra of CdS crystallites in aqueous solution. *Journal of Chemical Physics* **79,** 1086 (1983).

20. Bawendi, M. G., Steigerwald, M. . & Brus, L. E. The Quantum Mechanics of larger semiconductor clusters ("Quantum dots"). *Annual Review of Physical Chemistry* **41,** 477–496 (1990).

21. Reed, M. A. *et al.* Observation of discrete electronic states in a zero-dimensional semiconductor nanostructure. *Physical Review Letters* **60,** 535–539 (1988).

22. Petta, J. R. *et al.* Coherent Manipulation of Coupled Electron Spins in Semiconductor Quantum Dots. *Science* **309,** 2180–2184 (2005).

23. Goldstein, L., Glas, F., Marzin, J. Y., Charasse, M. N. & Le Roux, G. Growth by molecular beam epitaxy and characterization of InAs / GaAs strainedlayer superlattices. *Applied Physics Letters* **47,** 1099–1101 (1985).

24. *Quantum Dots: Optics, Electron Transport and Future Applications*. 358 (Cambridge University Press, 2012).

25. *Properties of lattice-matched and strained Indium Gallium Arsenide*. 317 (Inspec, the Institution of Electrical Engineers, 1993).

26. Marzin, J.-Y., Gérard, J.-M., Izraël, A. & Barrier, D. Photoluminescence of Single InAs Quantum Dots Obtained by Self-Organized Growth on GaAs. *Physical Review Letters* **73,** 716–719 (1994).

27. Young, R. J. *et al.* Inversion of exciton level splitting in quantum dots. *Physical Review B* **72,** 113305 (2005).

28. Jarlov, C. *et al.* Bound and anti-bound biexciton in site-controlled pyramidal GaInAs/GaAs quantum dots. *Applied Physics Letters* **101,** 191101 (2012).

29. Skiba-Szymanska, J. *et al.* Narrow emission linewidths of positioned InAs quantum dots grown on pre-patterned GaAs (100) substrates. *Nanotechnology* **22,** 065302 (2011).

30. Juska, G., Dimastrodonato, V., Mereni, L. O., Gocalinska, A. & Pelucchi, E. Towards quantum-dot arrays of entangled photon emitters. *Nature Photonics* **AOP,** (2013).

31. Shields, A. J. Semiconductor quantum light sources. *Nature Photonics* **1,** 215–223 (2007).

32. Santori, C., Fattal, D., Vucković, J., Solomon, G. S. & Yamamoto, Y. Indistinguishable photons from a single-photon device. *Nature* **419,** 594–7 (2002).

33. Yuan, Z. *et al.* Electrically driven single-photon source. *Science* **295,** 102–105 (2002).

34. Dousse, A. *et al.* Ultrabright source of entangled photon pairs. *Nature* **466,** 217–220 (2010).

35. Stevenson, R. M. *et al.* A semiconductor source of triggered entangled photon pairs. *Nature* **439,** 5 (2006).

36. Boyer de la Giroday, A. *et al.* Exciton-Spin Memory with a Semiconductor Quantum Dot Molecule. *Physical Review Letters* **106,** 216802 (2011).

37. Lindner, N. & Rudolph, T. Proposal for Pulsed On-Demand Sources of Photonic Cluster State Strings. *Physical Review Letters* **103,** 113602 (2009).

38. Cohen-Tannoudji, C., Diu, B. & Laloë, F. *Quantum Mechanics, Vol I*. 1524 (Wiley, 1977).

39. *Single Quantum Dots: Fundamentals, Applications and New Concepts*. 352 (Springer, 2003).

40. Gies, C., Wiersig, J. & Jahnke, F. in *Single semiconductor quantum dots* (Michler, P.) 1–30 (Springer, 2009).

41. Toda, Y., Moriwaki, O., Nishioka, M. & Arakawa, Y. Efficient Carrier Relaxation Mechanism in InGaAs/GaAs Self-Assembled Quantum Dots Based on the Existence of Continuum States. *Physical Review Letters* **82,** 4114–4117 (1999).

42. Nielsen, T., Gartner, P. & Jahnke, F. Many-body theory of carrier capture and relaxation in semiconductor quantum-dot lasers. *Physical Review B* **69,** 235314 (2004).

43. Urbaszek, B. *et al.* Nuclear spin physics in quantum dots: an optical investigation. *Reviews of Modern Physics* **85,** 79 (2012).

44. Bayer, M. *et al.* Fine structure of neutral and charged excitons in self-assembled In(Ga)As/(Al)GaAs quantum dots. *Physical Review B* **65,** 1–23 (2002).

45. Stevenson, R. M. *et al.* Evolution of Entanglement Between Distinguishable Light States. *Physical Review Letters* **101,** 170501 (2008).

46. Hudson, A. J. *et al.* Coherence of an entangled exciton-photon state. *Physical Review Letters* **99,** 266802 (2007).

47. Bennett, A. J. *et al.* Free induction decay of a superposition stored in a quantum dot. *Physical Review B* **84,** 195401 (2011).

48. Ellis, D. J. P. *et al.* Control of fine-structure splitting of individual InAs quantum dots by rapid thermal annealing. *Applied Physics Letters* **90,** 011907 (2007).

49. Trotta, R. *et al.* Universal recovery of the bright-exciton level-degeneracy in quantum dots without structural symmetry. *Physical Review L* **109,** 147401 (2012).

50. Bennett, A. J. *et al.* Electric-field-induced coherent coupling of the exciton states in a single quantum dot. *Nature Physics* **6,** 947–950 (2010).

51. Kuroda, T. *et al.* Symmetric quantum dots as efficient sources of highly entangled photons. *ArXiv eprints* 1302.6389v1 (2013).

52. Brassard, G., Lütkenhaus, N., Mor, T. & Sanders, B. C. Limitations on Practical Quantum Cryptography. *Physical Review Letters* **85,** 1330–1333 (2000).

53. Gao, W.-B. *et al.* Teleportation-based realization of an optical quantum two-qubit entangling gate. *Proceedings of the National Academy of Sciences of the United States of America* **107,** 20869–74 (2010).

54. Smirr, J.-L., Frey, R., Diamanti, E., Alléaume, R. & Zaquine, I. Intrinsic limitations to the quality of pulsed spontaneous parametric downconversion sources for quantum information applications. *Journal of the Optical Society of America B* **28,** 832 (2011).

55. Scarani, V., De Riedmatten, H., Marcikic, I., Zbinden, H. & Gisin, N. Four-photon correction in two-photon Bell experiments. *European Physical Journal D* **32,** 129–138 (2005).

56. Benson, O., Santori, C., Pelton, M. & Yamamoto, Y. Regulated and entangled photons from a single quantum Dot. *Physical Review Letters* **84,** 2513–6 (2000).

57. Reischle, M. *et al.* Triggered single-photon emission from electrically excited quantum dots in the red spectral range. *Applied Physics Letters* **97,** 143513 (2010).

58. Kessler, C. A. *et al.* Strong antibunching from electrically driven devices with long pulses: A regime for quantum-dot single-photon generation. *Physical Review B* **86,** 115326 (2012).

59. Salter, C. L. *et al.* An entangled-light-emitting diode. *Nature* **465,** 594–7 (2010).

60. Salter, C. L. Development and application of an entangled-light-emitting diode, Ph.D. thesis, University of Cambridge. (2011).

61. Schubert, E. F. *Light-Emitting Diodes*. 236 (Cambridge University Press, 2002).

62. Bennett, A. J. *et al.* Single-photon-emitting diodes: a review. *Physica Status Solidi (B)* **243,** 3730–3740 (2006).

63. Bienstman, P. Cavity Modelling Framework, http://camfr.sourceforge.net/ (accessed 2013-06-04).

64. Bienstman, P. Rigorous and efficient modelling of wavelength scale photonic components, Ph.D. thesis, University Gent. (2001).

65. Delbeke, D., Bockstaele, R., Bienstman, P., Baets, R. & Benisty, H. High-Efficiency Semiconductor Resonant-Cavity Light-Emitting Diodes: A Review. *IEEE Journal on Selected Topics in Quantum Electronics* **8,** 189–206 (2002).

66. Björk, G., Machida, S., Yamamoto, Y. & Igeta, K. Modification of spontaneous emission rate in planar dielectric microcavity structures. *Physical Review A* **44,** 669–681 (1991).

67. Schwagmann, A. *et al.* On-chip single photon emission from an integrated semiconductor quantum dot into a photonic crystal waveguide. *Applied Physics Letters* **99,** 261108 (2011).

68. Pooley, M. A. *et al.* Controlled-NOT gate operating with single photons Controlled-NOT gate operating with single photons. *Applied Physics Letters* **100,** 211103 (2012).

69. Friedler, I. *et al.* Solid-state single photon sources: the nanowire antenna. *Optics Express* **17,** 2095–2110 (2009).

70. Claudon, J. *et al.* A highly efficient single-photon source based on a quantum dot in a photonic nanowire. *Nature Photonics* **4,** 174–177 (2010).

71. Gregersen, N., Nielsen, T. R., Mørk, J., Claudon, J. & Gérard, J. M. Designs for high-efficiency electrically pumped photonic nanowire single-photon sources. *Optics Express* **18,** 21204–21218 (2010).

72. Kammerer, C. *et al.* Interferometric correlation spectroscopy in single quantum dots. *Applied Physics Letters* **81,** 2737 (2002).

73. Cassabois, G. & Ferreira, R. Dephasing processes in a single semiconductor quantum dot. *Comptes Rendus Physique* **9,** 830–839 (2008).

74. Legero, T., Wilk, T., Kuhn, A. & Rempe, G. Time-resolved two-photon quantum interference. *Applied Physics B: Lasers and Optics* **77,** 797–802 (2003).

75. Santori, C., Fattal, D., Vuckovic, J., Solomon, G. S. & Yamamoto, Y. Single-photon generation with InAs quantum dots. *New Journal of Physics* **6,** 89–89 (2004).

76. Fox, R. F. Contributions to the Theory of Multiplicative Stochastic Processes. *Journal of Mathematical Physics* **13,** 1196 (1972).

77. Berthelot, A. *et al.* Unconventional motional narrowing in the optical spectrum of a semiconductor quantum dot. *Nature Physics* **2,** 759–764 (2006).

78. Saleh, B. E. A. & Teich, M. C. *Fundamentals of photonics*. 966 (Wiley, 1991).

79. Patel, R. B. *et al.* Postselective two-photon interference from a continuous nonclassical stream of photons emitted by a quantum dot. *Physical Review Letters* **100,** 4 (2008).

80. Patel, R. B. *et al.* Quantum interference of electrically generated single photons from a quantum dot. *Nanotechnology* **21,** 274011 (2010).

81. Patel, R. B. *et al.* Two-photon interference of the emission from electrically tunable remote quantum dots. *Nature Photonics* **4,** 632–635 (2010).

82. Bennett, A. J., Patel, R. B., Nicoll, C. A., Ritchie, D. A. & Shields, A. J. Interference of dissimilar photon sources. *Nature Physics* **5,** 715–717 (2009).

83. Knill, E., Laflamme, R. & Milburn, G. J. A scheme for efficient quantum computation with linear optics. *Nature* **409,** 46–52 (2001).

84. Gottesman, D. & Chuang, I. L. Demonstrating the viability of universal quantum computation using teleportation and single-qubit operations. *Nature* **402,** 390–393 (1999).

85. Broome, M. A. *et al.* Photonic Boson Sampling in a Tunable Circuit. *Science* **339,** 794–798 (2012).

86. Spring, J. B. *et al.* Boson Sampling on a Photonic Chip. *Science* **339,** 798–801 (2012).

87. Hong, C. K., Ou, Z. Y. & Mandel, L. Measurement of Subpicosecond Time Intervals between Two Photons by Interference. *Physical Review Letters* **59,** 2044–2046 (1987).

88. Kaltenbaek, R., Blauensteiner, B., Żukowski, M., Aspelmeyer, M. & Zeilinger, A. Experimental Interference of Independent Photons. *Physical Review Letters* **96,** 240502 (2006).

89. Pittman, T. B. *et al.* Can Two-Photon Interference be Considered the Interference of Two Photons? *Physical Review Letters* **77,** 1917–1920 (1996).

90. Lettow, R. *et al.* Quantum Interference of Tunably Indistinguishable Photons from Remote Organic Molecules. *Physical Review Letters* **104,** 123605 (2010).

91. Beugnon, J. *et al.* Quantum interference between two single photons emitted by independently trapped atoms. *Nature* **440,** 779–82 (2006).

92. Maunz, P. *et al.* Quantum interference of photon pairs from two remote trapped atomic ions. *Nature Physics* **3,** 538–541 (2007).

93. Bernien, H. *et al.* Two-Photon Quantum Interference from Separate Nitrogen Vacancy Centers in Diamond. *Physical Review Letters* **108,** 043604 (2012).

94. Zeilinger, A. General properties of lossless beamsplitters. *American Journal of Physics* **49,** 882–883 (1981).

95. Feynman, R. P., Leyton, R. & Sands, M. *Feynman Lectures on Physics Volume 3*. (Pearson/Addison-Wesley, 1963).

96. Mattle, K., Weinfurter, H., Kwiat, P. G. & Zeilinger, A. Dense Coding in Experimental Quantum Communication. *Physical Review Letters* **76,** 4656–4659 (1996).

97. Patel, R. B. *et al.* Two-photon interference of the emission from electrically tunable remote quantum dots. *Nature Photonics* **4,** 632–635 (2010).

98. Kok, P. & Lovett, B. W. *Introduction to Optical Quantum Information Processing*. 504 (Cambridge University Press, 2010).

99. Stevenson, R. M., Bennett, A. J. & Shields, A. J. in *Quantum Dots - Optics, Electron Transport and Future Applications* (Tartakovskii, A.) 319–337 (Cambridge University Press, 2012).

100. Stevenson, R. M. *et al.* Coherent entangled light generated by quantum dots in the presence of nuclear magnetic fields. *ArXiv eprints* (2011). at <http://arxiv.org/abs/1103.2969>

101. Bennett, A. J. *et al.* Indistinguishable photons from a diode. *Applied Physics Letters* **92,** 193503 (2008).

102. Briegel, H., Dür, W., Cirac, J. I. & Zoller, P. Quantum Repeaters: The Role of Imperfect Local Operations in Quantum Communication. *Physical Review Letters* **81,** 5932–5935 (1998).

103. Blokhin, S. A. *et al.* Oxide-confined 850 nm VCSELs operating at bit rates up to 40 Gbit/s. *Electronics Letters* **45,** 501–502 (2009).

104. Liu, Y., Ng, W.-C., Oyafuso, F., Klein, B. & Hess, K. Simulating the modulation response of VCSELs, the effects of diffusion capacitance and spatial hole-burning. *IEE Proceedings Optoelectronics* **149,** 182–188 (2002).

105. Gazzano, O. *et al.* Bright solid-state sources of indistinguishable single photons. *Nature Communications* **4,** 1425 (2013).

106. Ates, S. *et al.* Post-Selected Indistinguishable Photons from the Resonance Fluorescence of a Single Quantum Dot in a Microcavity. *Physical Review Letters* **103,** 167402 (2009).

107. Matthiesen, C., Vamivakas, A. N. & Atatüre, M. Subnatural Linewidth Single Photons from a Quantum Dot. *Physical Review Letters* **108,** 093602 (2012).

108. He, Y.-M. *et al.* On-demand semiconductor single-photon source with near-unity indistinguishability. *Nature Nanotechnology* **8,** 213–217 (2013).

109. Dieks, D. Communication by EPR devices. *Physics Letters A* **92A,** 271–272 (1982).

110. Wootters, W. K. & Zurek, W. H. A single quantum cannot be cloned. *Nature* **299,** 802–803 (1982).

111. Bennett, C. H. & Brassard, G. Quantum Cryptography: Public Key Distribution and Coin Tossing. in *Proceedings of the IEEE International Conference on Computers, Systems and Signal Processing* 175–179 (IEEE Press, 1984).

112. Ursin, R. *et al.* Quantum teleportation across the Danube. *Nature* **430,** 849 (2004).

113. De Riedmatten, H. *et al.* Long Distance Quantum Teleportation in a Quantum Relay Configuration. *Physical Review Letters* **92,** 047904 (2004).

114. Marcikic, I., De Riedmatten, H., Tittel, W., Zbinden, H. & Gisin, N. Long-distance teleportation of qubits at telecommunication wavelengths. *Nature* **421,** 509–513 (2003).

115. Ma, X.-S. *et al.* Quantum teleportation over 143 kilometres using active feed-forward. *Nature* **489,** 269–73 (2012).

116. Jin, X.-M. *et al.* Experimental free-space quantum teleportation. *Nature Photonics* **4,** 376–381 (2010).

117. Merali, Z. The quantum space race. *Nature* **492,** 22–25 (2012).

118. Kim, Y. H., Kulik, S. P. & Shih, Y. Quantum teleportation of a polarization state with a complete bell state measurement. *Physical Review Letters* **86,** 1370–1373 (2001).

119. Lütkenhaus, N., Calsamiglia, J. & Suominen, K. Bell measurements for teleportation. *Physical Review A* **59,** 3295 (1999).

120. Jacobs, B. C., Pittman, T. B. & Franson, J. D. Quantum relays and noise suppression using linear optics. *Physical Review A* **66,** 052307 (2002).

121. Halder, M. *et al.* Entangling Independent Photons by Time Measurement. *Nature Physics* **3,** 692 (2007).

122. Takesue, H. & Miquel, B. Entanglement swapping using telecom-band photons generated in fibers. *Optics Express* **17,** 773–777 (2009).

123. Sangouard, N., Simon, C., De Riedmatten, H. & Gisin, N. Quantum repeaters based on atomic ensembles and linear optics. *Reviews of Modern Physics* **83,** 33–80 (2011).

124. Specht, H. P. *et al.* A single-atom quantum memory. *Nature* **473,** 190–193 (2011).

125. Bao, X. *et al.* Efficient and long-lived quantum memory with cold atoms inside a ring cavity. *Nature Physics* **8,** 517–521 (2012).

126. Yuan, Z.-S. *et al.* Experimental demonstration of a BDCZ quantum repeater node. *Nature* **454,** 1098–1101 (2008).

127. Zhao, Z., Yang, T., Chen, Y., Zhang, A. & Pan, J. Experimental Realization of Entanglement Concentration and a Quantum Repeater. *Physical Review Letters* **90,** 207901 (2003).

128. Kok, P. *et al.* Linear optical quantum computing. *Reviews of Modern Physics* **79,** 135 (2007).

129. Knill, E., Laflamme, R. & Milburn, G. J. A scheme for efficient quantum computation with linear optics. **409,** (2001).

130. Nielsen, M. A. & Chuang, I. L. *Quantum Computation and Quantum Information*. 700 (Cambridge University Press, 2000).

131. O'Brien, J. L., Pryde, G. J., White, A. G., Ralph, T. C. & Branning, D. Demonstration of an all-optical quantum controlled-NOT gate. *Nature* **426,** 264–266 (2003).

132. Nilsson, J. *et al.* Quantum teleportation using a light-emitting diode. *Nature Photonics* **7,** 311–315 (2013).

133. Stevenson, R. M. *et al.* Indistinguishable Entangled Photons Generated by a Light-Emitting Diode. *Physical Review Letters* **108,** 040503 (2012).

134. Boschi, D., Branca, S., De Martini, F., Hardy, L. & Popescu, S. Experimental realization of teleporting an unknown pure quantum state via dual classical and Einstein-Podolsky-Eosen channels. *Physical Review Letters* **80,** 1121–1125 (1998).

135. Bennett, C. & DiVincenzo, D. Quantum information and computation. *Nature* **404,** 247–55 (2000).

136. Brien, J. L. O., Furusawa, A. & Vučković, J. Photonic quantum technologies. *Nature Photonics* **3,** 687–695 (2009).

137. Ladd, T. D. *et al.* Quantum computers. *Nature* **464,** 45–53 (2010).

138. Cirac, J. I. & Zoller, P. Quantum computations with cold trapped ions. *Physical Review Letters* **74,** 4091–4094 (1995).

139. Weber, J. R. *et al.* Quantum computing with defects. *Proceedings of the National Academy of Sciences of the United States of America* **107,** 8513–8518 (2010).

140. Shulman, M. D. *et al.* Demonstration of Entanglement of Electroscatically Coupled Singlet-Triplet Qubits. *Science* **336,** 202–205 (2012).

141. Kane, B. E. A silicon-based nuclear spin quantum computer. *Nature* **393,** 133–137 (1998).

142. Pla, J. J. *et al.* High-fidelity readout and control of a nuclear spin qubit in silicon. *Nature* **496,** 334–338 (2013).

143. Riebe, M. *et al.* Deterministic quantum teleportation with atoms. *Nature* **429,** 734–737 (2004).

144. Barrett, M. D. *et al.* Deterministic quantum teleportation of atomic qubits. *Nature* **429,** 737–739 (2004).

145. O'Brien, J. L. Optical quantum computing. *Science* **318,** 1567–70 (2007).

146. Ma, X.-S. *et al.* Quantum teleportation over 143 kilometres using active feed-forward. *Nature* **489,** 269–73 (2012).

147. Legero, T., Wilk, T., Hennrich, M., Rempe, G. & Kuhn, A. Quantum Beat of Two Single Photons. *Physical Review Letters* **93,** 070503 (2004).

148. Specht, H. P. *et al.* Phase shaping of single-photon wave packets. *Nature Photonics* **3,** 469–472 (2009).

149. Altepeter, J. B., Jeffrey, E. R. & Kwiat, P. G. in *Advances in Atomic, Molecular and Optical Physics* (Berman, P. R. & Lin, C. C.) 105–159 (Academic Press, 2005).

150. Lo, H.-K. & Chau, H. F. Unconditional Security of Quantum Key Distribution over Arbitrarily Long Distances. *Science* **283,** 2050–2056 (1999).

151. Sasaki, M. *et al.* Field test of quantum key distribution in the Tokyo QKD Network. *Optics Express* **19,** (2011).

152. Giroday, A. B. De *et al.* All-electrical coherent control of the exciton states in a single quantum dot. *Physical Review B* **82,** 241301 (2010).

153. Hanson, R. & Awschalom, D. D. Coherent manipulation of single spins in semiconductors. *Nature* **453,** 1043–1049 (2008).

154. Overhauser, A. Polarization of Nuclei in Metals. *Physical Review* **92,** 411–415 (1953).

155. Meier, F. & Zakharchenia, B. P. *Optical orientation*. 523 (North-Holland, 1984).

156. Gammon, D. *et al.* Electron and Nuclear Spin Interactions in the Optical Spectra of Single GaAs Quantum Dots. *Physical Review Letters* **86,** 5176–5179 (2001).

157. Gammon, D. *et al.* Nuclear Spectroscopy in Single Quantum Dots: Nanoscopic Raman Scattering and Nuclear Magnetic Resonance. *Science* **277,** 85–88 (1997).

158. Maletinsky, P., Badolato, A. & Imamoglu, A. Dynamics of quantum dot nuclear spin polarization controlled by a single electron. *Physical Review Letters* **99,** 056804 (2007).

159. Chekhovich, E. A. *et al.* Structural analysis of strained quantum dots using nuclear magnetic resonance. *Nature Nanotechnology* **7,** 646–650 (2011).

160. Chekhovich, E. A. *et al.* Element-sensitive measurement of the hole–nuclear spin interaction in quantum dots. *Nature Physics* **9,** 74–78 (2012).

161. Krebs, O. *et al.* Anomalous Hanle effect due to optically created transverse Overhauser field in single InAs/GaAs quantum dots. *Physical Review Letters* **104,** 056603 (2010).

162. Maletinsky, P. & Imamoğlu, A. in *Single semiconductor quantum dots* (Michler, P.) 145–184 (Springer, 2009).

163. Chekhovich, E. A., Krysa, A. B., Skolnick, M. S. & Tartakovskii, A. I. Direct Measurement of the Hole-Nuclear Spin Interaction in Single InP/GaInP Quantum Dots Using Photoluminescence Spectroscopy. *Physical Review Letters* **106,** 027402 (2011).

164. Maletinsky, P. Polarization and Manipulation of a Mesoscopic Nuclear Spin Ensemble Using a Single Confined Electron Spin, Ph.D. thesis, ETH Zürich. (2010).

165. Belhadj, T. *et al.* Optically monitored nuclear spin dynamics in individual GaAs quantum dots grown by droplet epitaxy. *Physical Review B* **78,** 205325 (2008).

166. Krebs, O. *et al.* Hyperfine interaction in InAs/GaAs self-assembled quantum dots: dynamical nuclear polarization versus spin relaxation. *Comptes Rendus Physique* **9,** 874 (2009).

167. Eble, B. *et al.* Dynamic nuclear polarization of a single charge-tunable InAs⁄GaAs quantum dot. *Physical Review B* **74,** 081306 (2006).

168. Urbaszek, B. *et al.* Efficient dynamical nuclear polarization in quantum dots: Temperature dependence. *Physical Review B* **76,** 201301 (2007).

169. Braun, P.-F. *et al.* Bistability of the nuclear polarization created through optical pumping in In1−xGaxAs quantum dots. *Physical Review B* **74,** 245306 (2006).

170. Tartakovskii, A. I. *et al.* Nuclear Spin Switch in Semiconductor Quantum Dots. *Physical Review Letters* **98,** 026806 (2007).

171. Maletinsky, P., Lai, C., Badolato, A. & Imamoglu, A. Nonlinear dynamics of quantum dot nuclear spins. *Physical Review B* **75,** 035409 (2007).

172. Bennett, A. J. *et al.* Giant Stark effect in the emission of single semiconductor quantum dots. *Applied Physics Letters* **97,** 031104 (2010).

173. Bennett, A. J. *et al.* Voltage tunability of single-spin states in a quantum dot. *Nature Communications* **4,** 1522 (2013).

174. Belhadj, T. *et al.* Controlling the Polarization Eigenstate of a Quantum Dot Exciton with Light. *Physical Review Letters* **103,** 086601 (2009).

175. Merkulov, I. A., Efros, A. L. & Rosen, M. Electron spin relaxation by nuclei in semiconductor quantum dots. *Physical Review B* **65,** 205309 (2002).

176. Kaji, R., Adachi, S., Sasakura, H. & Muto, S. Precise measurements of electron and hole g-factors of single quantum dots by using nuclear field. *Applied Physics Letters* **91,** 261904 (2007).

177. Maletinsky, P., Kroner, M. & Imamoglu, A. Breakdown of the nuclear-spin-temperature approach in quantum-dot demagnetization experiments. *Nature Physics* **5,** 407–411 (2009).

178. Makhonin, M. N. *et al.* Voltage controlled nuclear polarization switching in a single InGaAs quantum dot. *Physical Review B* **79,** 125318 (2009).

179. Dzhioev, R. & Korenev, V. Stabilization of the Electron-Nuclear Spin Orientation in Quantum Dots by the Nuclear Quadrupole Interaction. *Physical Review Letters* **99,** 037401 (2007).

180. Pusey, M. F., Barrett, J. & Rudolph, T. On the reality of the quantum state. *Nature Physics* **8,** 475–478 (2012).